

# Investigating Antarctic subglacial hydrologic processes from marine sediment cores

Allison P. Lepp  
Charlottesville, Virginia

B.S. Geology, Georgia State University, 2014  
M.S. Earth and Environmental Studies, Montclair State University, 2018

A Dissertation presented to the Graduate Faculty  
of the University of Virginia in Candidacy for the Degree of  
Doctor of Philosophy

Department of Environmental Sciences

University of Virginia  
July 2023

Committee Members:  
Professor Lauren Miller  
Professor Matthew Reidenbach  
Professor Patricia Wiberg  
Professor Mark Skidmore  
Professor Sean Agnew



Copyright © 2023 by Allison Paige Lepp. All rights reserved.

“ I see always the steady, unremitting, downward drift of materials from above, flake upon flake, layer upon layer – a drift that has continued for hundreds of millions of years, that will go on as long as there are seas and continents. For the sediments are the materials of the most stupendous ‘snowfall’ the earth has ever seen.”

Rachel Carson, *The Sea Around Us*  
1951

## Abstract.

Understanding processes operating beneath glacial ice is imperative for holistic knowledge of glaciated regions and for accurately projecting future behavior of and sea-level contributions from the Antarctic Ice Sheet. Evolution of subglacial hydrologic networks is one such process where knowledge gaps persist, in large part because of the challenges in observing the subglacial environment and the subsequent paucity of empirical data spanning decadal to millennial temporal scales. Sediment cores from deglaciated continental shelves preserve evidence of subglacial drainage events into the ocean, providing a link between the marine geologic record and the subglacial hydrologic network through time. Yet, several analytical methods with the potential to reveal details of subglacial sedimentary processes and paleo-subglacial hydrological networks from meltwater plume deposits were heretofore unexplored. Five sediment cores from the calving margin of Thwaites Glacier, the most rapidly changing glacial system in West Antarctica today, are used to reconstruct a local meltwater drainage history through the Holocene (Chapter 2, Lepp et al., 2022). Trace elemental ratios for thick meltwater plume deposits reveal persistence, and transience, of subglacial drainage pathways over millennia, contextualizing modern observations. Core stratigraphy revealed by computed tomography scanning reflects distinctive styles of meltwater evacuation beneath eastern and western Thwaites and suggest that higher-magnitude drainage events have occurred in recent centuries compared to past millennia. Such events likely enhance ocean-driven melting, and imply existing models underestimate both ice-shelf melt rates and volume of freshwater input to the ocean in this rapidly changing region of the cryosphere. In Chapter 3, knowledge gaps around production of meltwater plume deposits and subglacial sedimentary processes are addressed by assessing grain shape and microtexture (Lepp et al., *preprint*). Silt-sized sediments from meltwater plume deposits and glacial diamictons from six relict and extant glacial systems in both hemispheres are quantified with metrics describing grain regularity and form, and the most significant grain-shape alteration between populations is observed in grains from systems with widespread melting of the ice surface. Grain surface textures provide comprehensive evidence that meltwater silts are produced widely through subglacial, rather than hydrological, transport. Grain micromorphology is thus a valuable addition to glaciomarine sediment analyses and can support experimental efforts to quantify sedimentary signatures of subglacial stress and deformation. Ice shelves are sensitive to subglacial drainage, but reconstructing plume activity through the Holocene is challenging. Isotopic evidence of subglacial meltwater discharge into the ocean is investigated using stable water isotopes from sediment porewater and the ratio of meteoric to lithogenic beryllium in sediments in Chapter 4 (Lepp et al., *in prep.*). Isotopic diffusion is unable to explain the observed downcore variation in porewater composition. The most depleted porewater, indicating a glacial source, are collected from ice-proximal, clay-rich diamictons, while elevated  $^{10}\text{Be}/^9\text{Be}$  ratios are seen in meltwater plume deposits in ice-proximal and more distal settings. These results suggest that an isotopic approach could be appropriate towards quantifying fluxes sediment into the ocean and mixing of water masses beneath ice shelves. The findings herein advance our ability to link glaciomarine sediment records to subglacial processes, hydrology, and ice-marginal response to subglacial discharge. While this work focuses on late Pleistocene and Holocene-age records, the sedimentological and geochemical methods we employ can be used to examine drill core records from earlier glacial periods, moving towards a more holistic understanding of Antarctic subglacial hydrologic evolution and behavior that are necessary for improving accurate projections of mass loss from the Antarctic Ice Sheet.



## Table of contents.

<i>Abstract</i>	<i>i</i>
<i>Table of contents</i>	<i>ii</i>
<i>List of tables</i>	<i>iv</i>
<i>List of figures</i>	<i>v</i>
<i>Acknowledgements</i>	<i>1</i>
<i>Co-authored research</i>	<i>2</i>
<b>Chapter 1: Introduction</b>	<b>3</b>
1.1 Marine geologic records of paleo-subglacial hydrology	4
1.2 Study site: Thwaites Glacier, West Antarctica	5
<b>Chapter 2: Sedimentary evidence for persistent subglacial meltwater discharge from Thwaites Glacier, West Antarctica</b>	<b>9</b>
2.1 Introduction	9
2.2 Materials and Methods	11
2.2.1 Grain-size and smear slide analyses	11
2.2.2 Physical and chemical analyses	12
2.2.3 Statistical analysis	13
2.3 Results	13
2.3.1 Grain-size distributions	13
2.3.2 Sediment geochemistry	14
2.3.3 Downcore physical properties and sedimentological structures	14
2.3.4 Principal component analysis	16
2.3.5 Facies interpretation	16
2.4 Discussion	17
2.4.1 Source and grain-size production of meltwater deposits	18
2.4.2 Spatial variability in subglacial meltwater plume deposition	19
2.4.3 Connection of meltwater plumes to the contemporary ice-ocean system	22
2.5 Conclusion	24
<b>Chapter 3: Insights into glacial processes from micromorphology of silt-sized sediment</b>	<b>35</b>
3.1 Introduction	35
3.1.1 Bathymetric and glaciological settings of study sites	36
3.2 Materials and Methods	38
3.2.1 Grain-shape analysis	39
3.2.2 Microtexture analysis	39

3.3 Results	40
3.3.1 Grain-shape distributions of meltwater plume deposits and tills	40
3.3.2 Microtexture observations	42
3.4 Discussion	43
3.4.1 Widespread subglacial sediment transport processes	43
3.4.2 Production of meltwater silts	45
3.4.3 Subglacial hydrological inferences from grain micromorphology	46
3.4.4 On subglacial basins as reservoirs and subglacial lake drainage	47
3.5 Conclusions	48
<b>Chapter 4: Isotopic signals of subglacial meltwater drainage into the Amundsen Sea Sector of West Antarctica</b>	<b>58</b>
4.1 Introduction	58
4.2 Methodology	59
4.2.1 Porewater sampling and stable water isotope analysis	59
4.2.2 Sediment porosity and isotopic diffusion modeling	60
4.2.3 Beryllium isotope leaching and analysis	61
4.3 Results and discussion	62
4.4 Conclusions and future work	64
<b>Chapter 5: Concluding Remarks</b>	<b>74</b>
5.1 Dissertation Summary	74
5.2 Suggestions for future research directions	75
<b>Appendix A2</b>	<b>78</b>
<b>Appendix A4</b>	<b>80</b>
<b>References</b>	<b>83</b>

## List of tables.

**Table 2.1.** Location, water depth, and recovery of the five Nathaniel B. Palmer (NBP) cores investigated in this study. Bathymetric highs H2 and H1 as defined by Hogan et al. (2020a). KC = Kasten core. TGT = Thwaites Glacier Tongue; EIS = Eastern Ice Shelf.

**Table 2.2.** Raw and calibrated radiocarbon dates. Calibration was performed using Marine20 in CALIB v.8.2. A marine reservoir age of 1,117  $^{14}\text{C}$  years from living (rose bengal stained) mixed-assemblages of foraminifera in surface sediments of core NBP19-02 MC16 was used to obtain a  $\Delta R$  value of 617 (Figure 2.1B).

**Table 3.1.** Sample identification, coordinates, facies, water depth, associated glacial system or region, and reference for all samples used in Chapter 3. Relict glacial systems and regions that are no longer glaciated are italicized. ^ denotes meltwater plume deposits with no till counterpart. \* indicates samples examined for microtexture analysis. Intervals indicate depth in the sediment core (with core top = 0) from which samples within the facies of interest were collected, and were chosen to avoid lithological boundaries. Negative elevation indicates water depth to core site, while positive elevation is used for reference materials. Diam. = diamicton.

**Table 3.2.** Results of two-tailed Z test and associated p-values performed on grain shape of meltwater plume deposit and till populations from each system. Z scores are absolute values. Shape metrics with statistically significantly different populations ( $Z > 3.0$ ) are shown in bold. Difference in means for those statistically significant metrics is presented with 95 % confidence interval calculated from 1,000 bootstrap replicates. Note the small values reflect both the range of the metric itself [0, 1] and supports the rejection of the null hypothesis that MPD and till sample populations are the same. Abbreviations of the glacial systems/regions are the same as in Figure 3.1.

**Table 4.1.** Geographic and bathymetric details for kasten cores (KC) used in this study. Multicore (MC), box core (BC) and CTD samples from which bottom water isotopes were used as reference are denoted by an asterisk. IS = Ice Shelf. For more context on cores referenced in Lepp et al. (2022) cores, see Chapter 2 of this dissertation.

**Table 4.2.** Range of porosities and diffusion coefficients for each sediment facies used in the porewater diffusion model. Mean porosity shows the average and standard error for a given facies for all 10 sediment cores that sampled that facies. Note that only one core sampled stratified diamicton and the mean porosity and diffusion coefficient for this facies is reported with standard deviation.

**Table 4.3.** Meteoric  $^{10}\text{Be}$  and native  $^9\text{Be}$  beryllium concentrations in Amundsen Sea sediment samples. Refer to Table 4.1 for sample coordinates and water depths. Unc. = uncertainty.

**Table A4.1.** Instrumental operating parameters for inductively-coupled plasma mass spectrometry conducted at Stanford University. The instrument was operated in single quad mode with He as a reaction gas.

## List of figures.

**Figure 1.1.** Study locations presented in this dissertation. Satellite imagery from Google Earth.

**Figure 2.1.** Regional map and locations of sediment cores used in this study. Bathymetry of the eastern Amundsen Sea Embayment (**A**) and in the vicinity of Thwaites Glacier (**B**). Data in Figure 1B were primarily collected on cruises NBP19-02 (Hogan et al., 2020a) and NBP20-02 and are gridded at 50 m. Bathymetry defining much of the eastern margin of the Eastern Ice Shelf was collected during the iStar project cruise JR294. Additional bathymetry and bed topography are from BedMachine (Morlighem et al., 2020), and sub-ice shelf bathymetry is from Jordan et al. (2020). Red and blue arrows denote inflow of warm water and outflow of meltwater-laden fresher water, respectively, from Wåhlin et al. (2021). Grounding-line data are from Rignot et al. (2011) and Milillo et al. (2019) and coastline data are from the Antarctic Digital Database (ADD). Subglacial flux is from the Quantarctica data package and was derived from a subglacial water routing algorithm run at a 1-km resolution, originally published by Le Brocq et al. (2013). Stars approximate where modeled subglacial channels coincide with the Thwaites Glacier grounding zone (Hager et al., 2022).

**Figure 2.2.** Grain-size distributions of sediment core samples (n=196) on a semi-log axis plotted against volume percent. Core locations are denoted by color in the inset map in panel (A). (**A**) All samples exhibit varying degrees of ~5 micron Mode 1 and ~11 micron Mode 2, similar to meltwater deposits described elsewhere along the continental shelf in the Pacific Sector of Antarctica. (**B**) Instrumental comparison for grain-size distributions of previously published meltwater deposits from the western Ross Sea (see inset in Figure 2.1A) collected during cruises NBP98-01 (KC54 26 cm) and NBP1502 (KC17 170 cm; KC24 79 cm) and published in Prothro et al. (2018) and Simkins et al. (2017). In the lower panel are samples KC33 200-202 cm and KC67 50-52 cm from Thwaites Glacier (TG) shown for reference.

**Figure 2.3.** Smear slide images and corresponding grain-size distributions for select samples. Images were taken under plane-polarized light. Grain-size distributions shown for corresponding intervals have the same axis labels as in Figure 2.2B. Panels examine grain-size Modes 1 and 2 in intervals (A) within the same core, (B) from cores from different geographic locations, and (C) in surface sediments. (**A**) Core KC04 is dominated by poorly-sorted, ice-shelf proximal sediments (left) but contains discrete layers of purely terrigenous and relatively well-sorted fine silt (right). (**B**) KC08 (left; offshore from TGT) and KC23 (right; EIS corner). Grain size Modes 1 and 2 are caused by terrigenous grains that are present in variable amounts despite geographical difference between sites. (**C**) KC67 is dominated by Mode 1 grains and features sparse, complete diatom frustules.

**Figure 2.4.** Sediment core geochemistry. (**A**) Downcore concentrations of selected trace elements in ppm. Core legend is given in the upper-right corner of the Ni plot. (**B-C**) Immobile trace elemental ratios Th/Zr and Sr/Th plotted against Ti. Element ratios of surface sediment samples (< 63 microns) representative for the detrital input into the eastern Amundsen Sea Embayment (ASE, sites 30-33 of Simões Pereira et al., 2018) and the western ASE (sites 34, 36, and 38 of Simões Pereira et al., 2018) in the vicinity of Thwaites Glacier are shown for

reference. The vertical dashed line indicates a division between eastern and western geochemical signals.

**Figure 2.5.** Downcore lithology, physical sediment properties, and sedimentary structures for each core. GS = grain size; MS = magnetic susceptibility; WC = water content; SS = shear strength. Sedimentary structures and stratigraphy are further discussed in Figure 2.6 with the added context from computed tomography images. Linescan MS profiles and discrete MS profiles are plotted together as a line and closed circles, respectively. Discontinuous linescan MS profiles can result from uneven core surfaces (e.g., KC04). Note the difference in scale of MS and Mean GS between cores.

**Figure 2.6.** Greyscale computed tomography (CT) images of sediment cores collected offshore Thwaites Glacier. (A) CT image next to linescan photo. Downcore Sr/Th is imposed on core KC33 and reflects a gradual change in sediment source. Dates (cal yr BP) are shown alongside the corresponding interval. Refer to Table 2.2 for error bounds. Colored vertical lines denote core sections shown in (B-F). (B-F) Sediment facies described in this study with annotations. Long-axis orientation for clasts of varying sizes is traced in diamicton facies (C) and (F). Note that more than one sediment facies is observed within each core.

**Figure 2.7.** Biplot projecting results of PCA. Variance in principal component (PC) 1 is largely controlled by grain-size parameters and water content while PC2 variance is influenced by trace element concentrations. The surface sample (0-2 cm) for each core is indicated by an enlarged symbol, and concentration ellipses are drawn to include the 95<sup>th</sup> percentile.

**Figure 2.8.** Frequency analysis of sediment layers observed in cores offshore the TGT. (A) Downcore frequency of sediment facies categorized as massive diamicton (Dm), graded silt layers and stratified diamicton (Ds), in addition to laminations and beds within facies Ds (lams). (B) Representative grain-size distributions for each sediment facies. Note that ice-rafted debris in Ds includes only the sand fraction and not coarser clasts. (C) Thickness of graded layers throughout core KC08. Boxplot denotes 75% of all graded layers are  $\geq 2.5$  cm. While thick (i.e.,  $\geq 5$  cm) graded layers are concentrated in the upper 70 cm of the core, a comparable layer is observed at  $\sim 280$  cm depth.

**Figure 2.9.** Cartoon of contrasting meltwater drainage styles inferred offshore from the EIS and TGT. Callouts show general depositional settings, not exact locations, of sediment facies presented in Figure 2.6. Grounding-line positions are not exact. (A) Persistent, low-magnitude drainage emanating from beneath eastern Thwaites Glacier. Settling from suspension dominates here, likely beneath a perennial canopy of floating ice. (B) Downslope gravitational transport sourced from sediment-laden meltwater plume deposits. Hyperpycnal flow delivers coarse silts and occasionally fine sands to trough, where fine silts and clays settle from suspension.

**Figure 3.1.** Graphical map illustrating components of a glacial system that may influence grain-shape alteration and meltwater production compare between study sites. Subglacial geology is binarized into hard (i.e., crystalline) and soft (clastic or carbonate sedimentary) beds. Relict glacial systems and deglaciated setting names are italicized. TI = Thor Iversenbanken, MTIS =

Marguerite Trough Ice Stream, PIG = Pine Island Glacier, TG = Thwaites Glacier, Ross = Ross Sea, LGM = Last Glacial Maximum.

**Figure 3.2.** Workflow for automated grain shape analysis. (A) Raw images captured by the Bettersizer S3 Plus, images post-processing, and in binarized forms. (B) Metrics and associated equations calculated for each grain.  $c$  = distance between ellipse foci and center;  $a$  = length of semi-major axis;  $A$  = area,  $P$  = perimeter,  $A_c$  = area of the convex hull that encompasses the grain.

**Figure 3.3.** Microtextures observed on quartz grains in the  $<63 \mu\text{m}$  size fraction (silt) from select till and meltwater plume deposit samples. Orange scale bar =  $20 \mu\text{m}$ . Green scale bar =  $5 \mu\text{m}$ . (A) Grain relief and (B) grain shape, following Mahaney (2002) and Vos et al. (2014), respectively. (C) Edge characteristics. (D) Fracture types characteristic of glacial transport, following grain types B-D from Passchier et al. (2021). Note the differences in scale bars. (E) Microtextures associated with fluvial transport, following Křížek et al. (2017). as = arcuate steps, b = breakage block, bc = breakage concavity, bp = broken plates, cf = conchoidal fracture, ea = edge abrasion, er = rounded edges, es = sharp edges, f = fracture face, ip = impact pit, lf = linear fracture, mr = meandering ridges, slf = sublinear fracture, ss = straight steps, up = upturned plates, v = v-shaped percussions.

**Figure 3.4.** Violin plots for paired MPDs and tills, or ice-proximal diamictons (Table 3.1), for each region with the number of samples from each grain type shown at the bottom of grain eccentricity. Box plots within each violin show the interquartile ranges. Those pairs outlined in solid green denote populations that are highly significantly different, while the dashed green line indicates pairs that are significantly different as determined by a two-type Z test. Refer to Figure 3.2 for shape metric equations. TI = Thor Iversenbanken; MTIS = Marguerite Trough Ice Stream, PIG = Pine Island Glacier, TG = Thwaites Glacier, Ross = Ross Sea.

**Figure 3.5.** Circularity of meltwater plume deposit grains with first and third quartiles indicated by dashed lines and the median by a solid line. Glacial systems are grouped and colored by region. Samples with no till counterpart are denoted by ^ (see also Table 3.1).

**Figure 3.6.** Overrepresentation and frequency of occurrence of microtextures in both grain populations observed on 132 quartz grains. Refer to Figure 3.3 for examples of microtextures. Angular grains and all fracture types, as well as edge abrasion, are overrepresented in till grains, whereas MPDs exhibit a higher proportion of subangular and subrounded grains with edge rounding. Many mechanical microtextures (e.g., fracture faces, linear and sublinear fractures) are observed at comparable frequencies in both grain populations.

**Figure 3.7.** Visualization of grain shape evolution. (A), (C), and (E) show grain circularity for supra- or englacial reference material in comparison to glacial-marine diamicton, till, and meltwater plume deposits from a neighboring glacial system. SEM images of (B) cryoconite, (D) basal fringe debris, and (F) basal ice debris show highly fractured and elongated grains that are less common following subglacial transport. Note that in (C) the middle violin includes samples from ice-proximal diamicton from offshore Pine Island and Thwaites glaciers, as well as

subglacial till samples from Pine Island Glacier (Table 3.1). Scale bar in (B), (D), and (F) is 20 microns.

**Figure 4.1.** Location of sediment cores from the Amundsen Sea sector of West Antarctica (A) for which porewater diffusion profiles are examined. (B) Sediment cores collected from ice-marginal locations offshore the Dotson and Getz ice shelves. (C) Sediment cores from inner Pine Island Bay offshore of the Pine Island and Thwaites ice shelves. Grounding line data are from Milillo et al. (2019) and Rignot et al. (2011). BedMachine bathymetry is from Morlighem et al. (2020) and ice surface elevation is from the Reference Elevation Model of Antarctica (REMA; Howat et al., 2022).

**Figure 4.2.** Sampling image of sediment porewater extraction using a Rhizon filter. A minimum of 2 mL of water were collected from each interval for stable water isotope analysis.

**Figure 4.3.** Downcore porosity, facies assignments,  $^{10}\text{Be}/^{9}\text{Be}$  ratios, and both modeled (solid line) and measured (circle) concentrations of  $\delta^{18}\text{O}$  (‰) for select sediment cores. Plots are arranged from western (left) to eastern (right) core sites Sl: laminated silty clay; Sb: bioturbated silty clay; Ssl: laminated sandy silts; Dm: massive diamicton; Ds: stratified diamicton.

**Figure 4.4.** Spatial distribution of oxygen isotope ratio (A-B) and deuterium excess (C-D). Purple lines indicate linear regressions between each pair of variables with standard error bounds shaded in gray, and the Pearson correlation coefficients and  $p$  values are shown in the dark gray boxes. Cruise and core symbology is shown in (A).

**Figure 4.5.** Box and whisker plots showing the range for all measured (A)  $\delta^{18}\text{O}$  and (B) deuterium excess colored by facies. Dashed line represents the most enriched end-member for Antarctic snow from a database with isotopic measurements from over 1,100 locations (Masson-Delmotte et al., 2008). Sl: laminated silty clay; Sb: bioturbated silty clay; Ssl: laminated sandy silts; Dm: massive diamicton; Ds: stratified diamicton.

**Figure A2.1.** Histograms showing skewness and sorting (i.e., standard deviation) statistics for all grain size samples ( $n=196$ ). Note range of axes differ between plots. The majority of samples are fine-skewed, while KC33 and KC67 distributions are closest to symmetrical (skewness=0). Cores KC33 and KC67 are the most well-sorted, with KC67 showing little variation in sorting downcore. Ice-shelf proximal cores KC04 and KC23 show the poorest sorting, consistent with diamicton and glacially-influenced deposits.

**Figure A2.2.** Distance of contemporary plume migration estimated by (A) drawing transects from most proximal, and most recent (as is available), grounding line position to each core site. (B) Projections of horizontal bathymetric profiles of transects. Grounding line position is on the left and core location on the right. Transects were mapped using the 3D Analyst toolbox in ArcGIS. Note the difference in axis values between transects. Grounding line data are from Rignot et al. (2011) and Milillo et al. (2019). Floating ice is from the Reference Elevation Map of Antarctica (REMA; Howat et al., 2019).

**Figure A2.3.** Location of core sites georeferenced onto a map of Thwaites Glacier ice-shelf and ice-tongue extents in 1996 (yellow) and 2008 (red). Adapted from MacGregor et al. (2012).

**Figure A4.1.** Downcore porosity, facies assignments, and modeled (solid line) and measured (circle)  $\delta^{18}\text{O}$  concentrations for sediment cores without beryllium measurements. Plots are arranged from western (left) to eastern (right) core sites. Sl: laminated silty clay; Sb: bioturbated silty clay; Ssl: laminated sandy silts; Dm: massive diamicton; Ds: stratified diamicton.

**Figure A4.2.** Box and whisker plots showing the range of  $\delta\text{D}$  for porewater samples colored by facies. Dashed line represents the most enriched end-member for Antarctic snow from a database with isotopic measurements from over 1,100 locations (Masson-Delmotte et al., 2008). Sl: laminated silty clay; Sb: bioturbated silty clay; Ssl: laminated sandy silts; Dm: massive diamicton; Ds: stratified diamicton.



## Acknowledgements.

It is a surreal feeling to be writing this part of my dissertation, but I am full of gratitude in doing so as my mind floods with the faces of the many folks who have been instrumental in my doctoral journey. First, a profound thank you to Dr. Lauren Miller not only for her scientific guidance, but also her professional and personal support and encouragement. Lauren, thank you for trusting me and supporting me in exploring interests outside of academia. I have learned from you how to navigate challenging situations with grace and diplomacy while never compromising one's self, one's values, or one's scientific integrity.

Thank you to Marion, Santi, Tahi, Medha, and the many others who have come through the Ice & Ocean group at UVA. It has been a privilege to learn from and alongside all of you, and I am without a doubt a kinder, more well-rounded scientist and human as a result of our discussions. I am endlessly inspired by each of you, and I am so excited to continue cheering for y'all in whatever life has in store for you next.

Thank you to my committee members for providing feedback and guidance along the way; this dissertation would undoubtedly be of lower quality without your input. The UVA Nanoscale Materials Characterization Facility is thanked for SEM training and use. Delaney Buskard and Medha Prakash are thanked for their contributions to the grain-shape code used in Chapter 3. Thank you to Dr. Jane Willenbring and the Center for Accelerated Mass Spectrometry at Lawrence Livermore National Lab for the support in conducting the beryllium analysis in Chapter 4. Val Stanley and the curatorial team at Oregon State University Marine and Geologic Repository are thanked for fulfilling several sediment sample requests. To the co-PIs of THOR, it has been a truly impactful experience working (and sailing!) with such knowledgeable and dedicated scientists. Thanks especially to Dr. John Anderson for being generous with his time and expertise, even in retirement.

I want to acknowledge and appreciate professional colleagues who have become dear friends: Rachel, Asmara, Kenzie, and Lisa, thank you for the encouragement, judgement-free discussions, and scientific feedback. To the Polar Impact crew, in particular Prem, Ariel, Julia, Jackie, and Mariama, it's been an absolute honor to support the expansion of the Polar Impact Network over the past three years. Thank you all for trusting me, teaching me, and keeping it real. Can't wait to see what the future of polar research holds!

To those who support my whole being, whether I am pursuing a PhD, hiking for months on end, applying to the Peace Corps, or contemplating leaving it all behind to build a vineyard: Mom, Dad, Zena, Zak, Schyler, Will, Frost, and Rachel – thank you. To Joseph and Cato, you two have provided me with some of the most joyful memories during this time and offered comfort when I've been overwhelmed and downright unpleasant. Thank you both. Thank you to Karl Hamsch at Loving Cup for indulging my never-ending questions about viticulture, for feigning interest in subglacial hydrology, and for offering the Loving Cup as a place of solace and connection to nature.

The funding for this work comes from the National Science Foundation (Grant no. 1738942) and the Natural Environment Resource Council (Grant nos. NE/S0006664/1 and NE/S006672/1) as part of the International Thwaites Glacier Collaboration. I carried out this research largely at the University of Virginia, on the unceded land of the Monacan Nation. I recognize and honor their stewardship over these lands past, present, and future.

## Co-authored Research.

During my doctoral program, I had the privilege to contribute to scientific research projects beyond what comprises this dissertation. Through these positive and collaborative experiences, I learned more about processes outside of my expertise and deepened my appreciation for the interconnectedness of ice, ocean, atmosphere, sediment, and life in the Antarctic. Below are select publications and conference abstracts that I co-authored during my time as a PhD student:

### *Publications*

- Herbert, L.C., **Lepp, A.P.**, and eight others: Volcanogenic fluxes of iron from the seafloor in the Amundsen Sea, *Marine Chemistry*, 104250, doi: 10.1016/j.marchem.2023.104205, 2023.
- Simkins, L.M., Greenwood, S.L., Winsborrow, M.C.W., Bjarnadóttir, L.R., and **Lepp, A.P.**: Advances in understanding subglacial meltwater drainage from past ice sheets, *Annals of Glaciology*, 1-5, doi: 10.1017/aog.2023.16, 2023.
- Clark, R.W. and 14 others *including* **Lepp, A.P.**: Synchronous retreat of Thwaites and Pine Island glaciers in response to external forcings in the pre-satellite era, *Proceedings of the National Academy of Sciences* (*in press*).
- Hojnacki, V., **Lepp, A.P.**, Castaldo, J.H., States, A., Li, X., and Passchier, S.: Impact of Eocene-Oligocene Antarctic glaciation on the paleoceanography of the Weddell Sea, *Paleoceanography and Paleoclimatology*, 37, e2022PA004440, doi: 10.1029/2022PA004440, 2022.

### *Conference Abstracts*

- Herbert, L.C., **Lepp, A.P.**, and six others (2022). A potential benthic source of nutrient iron driving productivity in the Amundsen Sea in the context of current and past glacial retreat. American Geophysical Union (*poster*).
- McKenzie, M.A., Simkins, L.M., and **Lepp, A.P.** (2022). Outcrop perspectives on spatially variable retreat of the marine-terminating southern Cordilleran Ice Sheet. American Geophysical Union. (*poster*)
- Pavia, F., Clark, R., **Lepp, A.**, and four others (2022). Calibrating extraterrestrial <sup>3</sup>He in ice-proximal marine sediments as a quantitative proxy for past West Antarctic Ice Sheet melt rates. WAIS Workshop. (*poster*)
- Wellner, J.S., Clark, R.C., Lehrmann, A., **Lepp, A.P.** and 12 others (2022). Pre-satellite retreat of Thwaites and Pine Island glaciers: Recent results from sediment cores. European Geophysical Union. (*oral; invited*)
- Wiggins, T., Munevar Garcia, S., **Lepp, A.P.**, Simkins, L.M. (2022). Morphometry of glacial lakes in North America. Southeast GSA Annual meeting (*oral*)
- Herbert, L.C., **Lepp, A.**, and four others (2021). Benthic biogeochemistry and trace metal fluxes near the Thwaites and Pine Island Glaciers, Amundsen Sea. Goldschmidt. (*oral*)

## Chapter 1: Introduction

The Antarctic Ice Sheet (AIS) at present contains the approximate equivalent of 58 meters of global sea level rise (SLR; Morlighem et al., 2020). Decades of satellite observations reveal that portions of the West Antarctic Ice Sheet (WAIS), where glaciers flow across land that is largely below sea level and terminate in the ocean, have experienced sustained mass loss from grounded ice and floating ice shelves (Rignot et al., 2019). Interactions between relatively warm ocean masses on the continental shelf and the grounding zones of marine-terminating glaciers (Mankoff et al., 2012; Khazendar et al., 2016; Wåhlin et al., 2021) are the principal driver behind satellite-era glacial retreat (e.g., Holland et al., 2020 and references therein). Ice-sheet models projecting the future contribution of the AIS to global SLR indicate that as much as 3 m could be expected by the year 2300, with the majority deriving from the WAIS (Golledge et al., 2015; DeConto et al., 2021); reducing uncertainty in these projections is critical to develop and implement strategies and policies for coastal resiliency worldwide.

Subglacial hydrology encompasses the storage, transmission, and distribution of liquid water beneath ice sheets and is one such component of glacial systems that is neither well understood, nor widely incorporated into ice-sheet models (Flowers, 2015). In general, subglacial meltwater can reduce effective pressure and basal drag at the ice-bed interface, acting as a lubricant and promoting faster ice-flow velocities than would occur in the absence of water. Remote sensing and on-ice geophysics have revealed spatiotemporal variations in ice flow associated with subglacial lakes (Bell et al., 2007; Stearns et al., 2008), seasonal surface melt cycles (Cowton et al., 2013), and basal water organization (Schroeder et al., 2013). For marine-based glacial systems like the WAIS, subglacial drainage has been theorized (Jenkins, 2011) and observed (Le Brocq et al., 2013; Alley et al., 2016; Marsh et al., 2016; Gourmelen et al., 2017; Wei et al., 2020) to enhance melting of ice shelves (i.e., the floating extensions of grounded glacial ice) which are critical for regulating flux of Antarctic land-based ice into the ocean (e.g., Scambos et al., 2004; Fürst et al., 2016). Organization of subglacial drainage (i.e., water flowing in distributed films, through isolated cavities, or via connected channels) influences effective pressure at the ice-bed interface differently (Greenwood et al., 2016; Dow et al., 2022), but drainage styles are transient in space and time which leads to challenges in reconstructing drainage evolution prior to the advent of satellite technologies.

Knowledge gaps persist due to the challenges of observing subglacial processes, the preservation bias of landform records, and a paucity of work that integrates geomorphic and sedimentological observations into modeling and experimental frameworks. In recent decades, indirect observations of subglacial hydrological conditions have widened the perspective of the spatiotemporal scales over which subglacial plumbing may evolve (e.g., Carter and Fricker, 2012; Cowton et al., 2013; Schroeder et al., 2013; Dowdeswell et al., 2015; Young et al., 2016; Clyne et al., 2020; Dow et al., 2020; Nanni et al., 2020; Chandler et al., 2021). However, an incomplete understanding of subglacial drainage evolution and subsequent ice-sheet response on long time scales (i.e., several decades to millennia) create caveats in extending findings from modern observations in time and space. Similarly, geomorphic analyses of meltwater-derived

and ice-marginal landforms, supported by increased resolution and spatial coverage of bathymetric mapping over deglaciated continental shelves, indicate subglacial hydrologic activity and patterns of grounding-zone retreat are tightly coupled (e.g., Simkins et al., 2021). Yet, geomorphology of submarine landscapes alone fails to convey critical details about paleo-subglacial meltwater drainage frequency, style, and magnitude of meltwater discharge (e.g., Simkins et al., 2017; Munoz and Wellner, 2018; Kirkham et al., 2019, 2020).

This dissertation examines evidence of subglacial drainage into the ocean as recorded by a suite of recently collected (2019-2022) marine sediment cores, as well as legacy cores recovered during various polar research expeditions over the past four decades, and leverages emerging and underused analytical methods to connect offshore records with subglacial hydrological processes. Because evacuation of subglacial meltwater from marine-terminating glaciers delivers glaciogenic sediments into the ocean, well-preserved marine sediment archives are uniquely poised to reconstruct details of meltwater activity on timescales for which neither observational nor seascape records are appropriate. Chapters 2 and 4 focus primarily on Thwaites Glacier and neighboring glaciers draining into the eastern Amundsen Sea, West Antarctica (Figure 1.1), and offer perspectives of meltwater discharge activity as recorded by sediment and porewater chemistry in the context of Holocene glacial retreat (Lepp et al., 2022; Lepp et al., *in prep*). Chapter 3 employs a process-based approach by integrating sediment archives from extant and relict glacial systems in both hemispheres, examining grain micromorphology reflective of different modes of subglacial sediment transport, and connecting grain-scale properties of glacial sediments to (paleo)subglacial hydrologic conditions (Lepp et al., *preprint*).

### *1.1 Marine geologic records of subglacial hydrology*

Subglacial meltwater flow follows a hydraulic gradient that is a function of bed topography and ice thickness (Shreve, 1972), and the volume, distribution, and transmission of this water influence ice behavior (e.g., Fricker et al., 2007; Stearns et al., 2008; Siegfried et al., 2016). Processes like frictional and strain heating (Cuffey and Paterson, 2010) through internal ice deformation and ice flow over topographically rough beds (e.g., Winsborrow et al., 2010; Krabbendam, 2016) contribute to basal meltwater supply, as does a regionally-elevated geothermal heat flux (e.g., Damiani et al., 2014; Dziadek et al., 2021; Reading et al., 2022 and references therein) and, in some glacial systems, till porewater (Christoffersen et al., 2014; Gustafson et al., 2022). Beneath the Greenland Ice Sheet (GrIS), melting of surface ice that drains to the bed (Chu, 2014; Willis et al., 2015; Smith et al., 2015; Poinar et al., 2017) contributes substantially to basal water supply. Recent observations (Bell et al., 2018) and model projections (Trusel et al., 2015; Lenaerts et al., 2016; Gilbert and Kittel, 2021) suggest the same may become true for portions of the AIS under evolving climate conditions. Meltwater production, and the subsequent style, frequency, and magnitude of drainage events, vary in time and space; while it is implied these variations would leave markedly different signatures in the

geologic record, few works have attempted to decipher those signatures using marine sediment cores.

The integration of meltwater plume deposits (MPDs) into glaciomarine facies models and coupled sedimentological-geomorphological studies offshore the AIS and GrIS have revealed clear linkages between post-Last Glacial Maximum (ca. 26,000 ka) grounding-line retreat and active subglacial plumbing systems (e.g., Prothro et al., 2018; O'Regan et al., 2021; Lepp et al., 2022; Clark et al., 2023). Specifically, Antarctic marine sediment cores recovering MPDs stratigraphically positioned above subglacial till or glacial-proximal diamicton and, in some instances, below microfossil-rich glaciomarine sediments have been collected offshore the relict Marguerite Trough Ice Sheet in the West Antarctic Peninsula (Kennedy and Anderson, 1989), Pine Island (Witus et al., 2014) and Thwaites Glaciers (Lepp et al., 2022; Clark et al., 2023) in the eastern Amundsen Sea, and in the eastern and western Ross Sea (Simkins et al., 2017; Prothro et al., 2018). The geographic distribution and frequency with which this sequence is observed suggests widespread subglacial hydrological processes and conditions that connect to overall glacial stability. Additionally, these records implicate that intensive expulsion of subglacial meltwater may be a precursor to grounding-line retreat, associated with heightened meltwater production and/or evacuation of subglacial meltwater reservoirs. While measurements like grain size and sorting, magnetic susceptibility, and water content have been widely used to characterize MPDs, additional properties of these sediments have not been interrogated to the fullest extent that could reveal coveted details of subglacial plumbing through time. To that end, Chapter 3 examines grain shape in order to connect MPDs to styles of subglacial meltwater transmission, and presents the first microtexture analysis focused on the silt-size fraction (4-63 microns ( $\mu\text{m}$ )) to evaluate dominant modes of subglacial sediment transport. An isotopic approach for connecting marine sediment cores with meltwater drainage activity is taken in Chapter 4, wherein stable water isotopes of sediment porewater and beryllium isotopes of solid sediments are evaluated for their potential to record meltwater-driven changes in water chemistry and sediment source.

### *1.2 Study site: Thwaites Glacier, West Antarctica*

The majority of sediment cores presented in this work were collected offshore of Thwaites Glacier, West Antarctica. The Thwaites Glacier contains approximately 65 cm of sea level equivalent and contributes roughly 4 % to global sea level rise every year (Morlighem et al., 2020). Satellite measurements indicate that the preeminent source of ice-mass loss from the AIS is glaciers draining into the Amundsen Sea, including Thwaites Glacier (Rignot et al., 2019). Thwaites Glacier is grounded below sea level on a bed that dips landward; this configuration indicates Thwaites is susceptible to self-sustaining retreat through a feedback known as the marine ice-sheet instability (Weertman, 1974; Schoof, 2007; Robel et al., 2019), and some have posited that such a runaway retreat may already be underway (Joughin et al., 2014). Because the Thwaites catchment extends ~450 km to the interior of the WAIS (Holt et al., 2006),

destabilization or collapse of Thwaites is predicted to trigger an ice-sheet wide response (DeConto et al., 2021).

At the Last Glacial Maximum (LGM; ca. 26,000 thousand years ago (ka)), an expansive Thwaites Glacier was grounded proximal to the outer continental shelf (Larter et al., 2014 and references therein). Ice drainage converged with Pine Island Glacier to the northeast, and radiocarbon dates constrain the initial post-LGM retreat of the former Thwaites-Pine Island system to the late Pleistocene (Kirshner et al., 2012; Hillenbrand et al., 2013; Larter et al., 2014). Glacial retreat history across Pine Island Bay from the outer shelf to the modern position of Thwaites and Pine Island Glaciers has been inferred using marine sediment cores, seafloor geomorphology, and seismic surveys which collectively indicate post-LGM grounding-line retreat was dynamic and episodic (Lowe and Anderson, 2002; Kirshner et al., 2012; Graham et al., 2016). Mapped grounding zone wedges, asymmetrical sedimentary deposits that form through sediment-gravity flows, deformation, and meltout of basal ice debris at the grounding line (Simkins et al., 2018), on the outer- and mid-continental shelf with nearly 100 km between them (Graham et al., 2010) suggests a phase of relatively rapid retreat across the mid-shelf punctuated by periods of grounding-line stability. Retreat from the mid-shelf to the inner shelf of Pine Island Bay positioned the grounding line of a, now distinct, Thwaites Glacier to within ~100 km of its current location by ~10 ka (Hillenbrand et al., 2013; Nitsche et al., 2013; Witus et al., 2014; Lepp et al., 2022). Early Holocene (10.4-7.5 ka) deglaciation of Pine Island Bay was, in large part, driven by the upwelling of warm, circumpolar deep water (CDW) that increased melting of floating and grounding-line ice (Hillenbrand et al., 2017). Upwelling of CDW is tied to strengthened westerly winds that may be related to the Southern Annular Mode and climate variability in the Pacific (e.g., Steig et al., 2012). This Pacific-sector teleconnection is believed to have been reinstated in the mid-1940s, when strong El Niño conditions preceded the synchronous retreat of Thwaites and Pine Island glaciers by only a few years (Hillenbrand et al., 2017; Smith et al., 2017; Clark et al., 2023).

Today, Thwaites Glacier drains into inner Pine Island Bay which is characterized by rugged bathymetry including distinctive highs that promote ice pinning (Hogan et al., 2020a), streamlined bedforms (Graham et al., 2016), and interconnected basins and channels reflecting a subglacial hydrologic network beneath a formerly expanded Thwaites (Nitsche et al., 2013; Kirkham et al., 2019). The Thwaites Eastern Ice Shelf is pinned along one of the aforementioned bathymetric highs while its floating ice tongue, which is fed by the fast-flowing trunk of grounded ice (Rignot et al., 2019), became unpinned from an adjacent high between 2011 and 2019 (Rignot et al., 2011; Hogan et al., 2020a; Lepp et al., 2022). These floating extensions of grounded ice exert backstress on ice upstream, but continued ice-shelf thinning and mass loss is expected to reduce this buttressing effect (Fürst et al., 2016). Upstream of the Thwaites Glacier grounding line, subglacial lithology can be primarily characterized as mafic intrusion, felsic granitoid, basins filled with pre-Oligocene sediments, or other crystalline material of intermediate composition (Hillenbrand et al., 2003; Muto et al., 2016; Jordan et al., 2023 and references therein). While almost certainly spatially variable, regional geothermal heat flux is

elevated compared to typical continental crust (Damiani et al., 2014; Schroeder et al., 2014; Dziadek et al., 2021). The Thwaites Glacier catchment is within the West Antarctic Rift System, a product of Cenozoic tectonics, and is proximal to several active subglacial volcanoes (Quartini et al., 2021).

Subglacial meltwater beneath the contemporary Thwaites Glacier is inferred to drain through both distributed and channelized configurations, and the transition from the former to the latter occurs coincident with a change in ice surface slope and increase in basal meltwater production (Schroeder et al., 2013), consistent with glaciohydrological theory (e.g., Greenwood et al., 2016). Saturated till downstream of topographic bumps is implied from geophysical observations, which implies co-occurring styles of subglacial water and zones of spatially variable pressure at the ice-bed interface (Clyne et al., 2020). Active transmission of water downstream between subglacial basins has been observed from satellite altimetry measurements (Hoffman et al., 2020, Malczyk et al., 2020), albeit unaccompanied with change in ice-flow velocity. Pine Island Glacier, which shares a catchment divide with Thwaites Glacier to the east, is one location where marine sediment cores record a Holocene transition from subglacial to open-marine conditions accompanied by silt-rich, well-sorted sediments interpreted as MPDs (Kirshner et al., 2012; Witus et al., 2014). In fact, meters-thick graded deposits and widespread MPDs implicate high energy, outburst-style subglacial drainage (Witus et al., 2014). Despite extensive evidence for an active subglacial hydrologic system beneath the contemporary Thwaites Glacier, no records had been investigated to assess how long-lived such a system might be or the styles with which meltwater drained into the ocean. Furthermore, the impact of subglacial hydrology on either recent or historical (i.e., pre-satellite era) changes to the Thwaites Glacier grounding line or ice shelf was unknown prior to the study presented in Chapter 2.

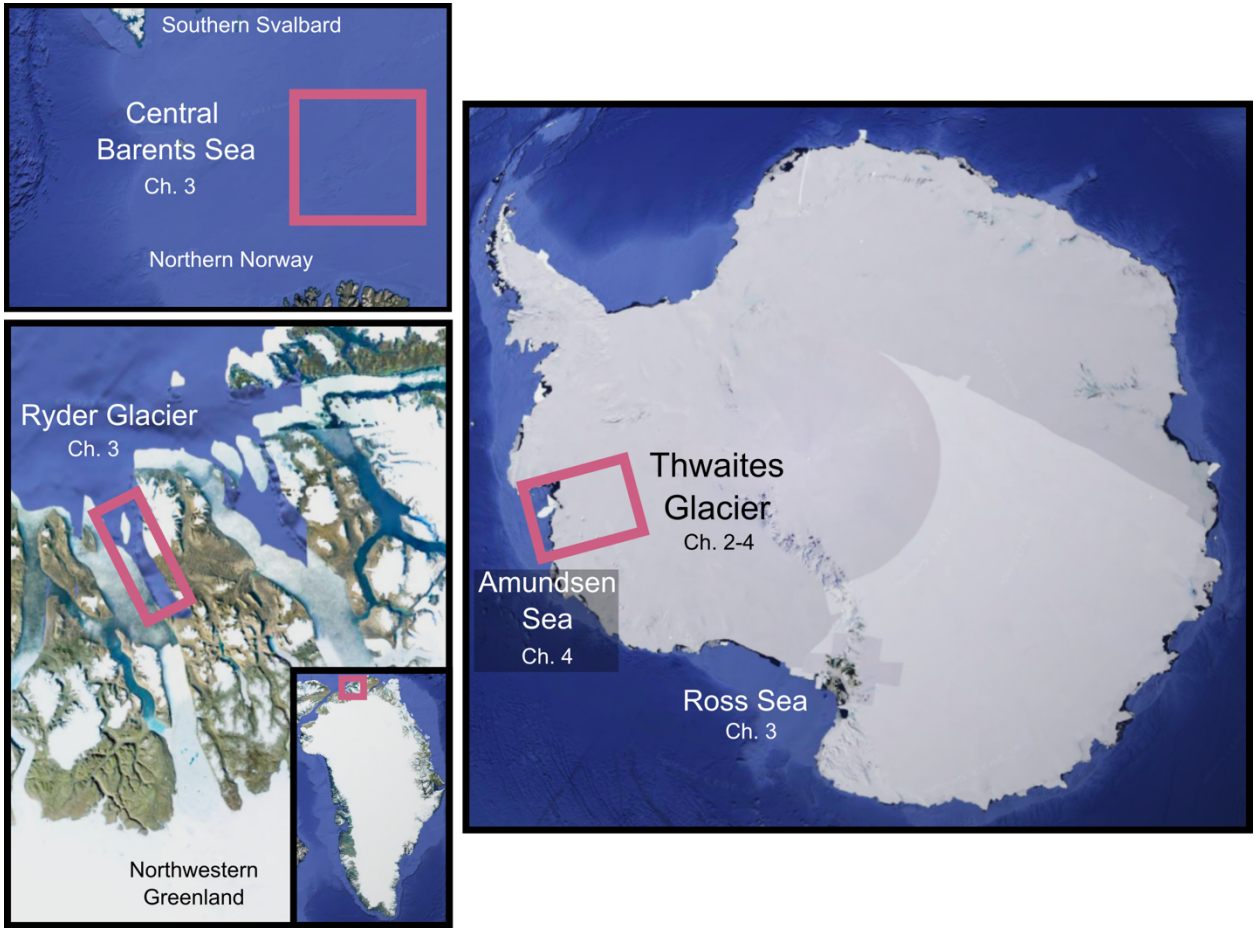


**Figure 1.1.** Study locations presented in this dissertation. Satellite imagery from Google Earth.



## Chapter 2: Sedimentary signatures of persistent subglacial meltwater drainage from Thwaites Glacier, West Antarctica

*Adapted from:* Lepp, A.P., Simkins, L.M., Anderson, J.B., Clark, R.W., Wellner, J.S., Hillenbrand, C-D., Smith, J.A., Lehrmann, A.A., Totten, R., Larter, R.D., Hogan, K.A., Nitsche, F.O., Graham, A.G.C., and Wacker, L.: Sedimentary signatures of persistent subglacial meltwater drainage from Thwaites Glacier, Antarctica, *Frontiers in Earth Science*, 10, 863200, <https://doi.org/10.3389/feart.2022.863200>, 2022.<sup>1 2</sup>

### 2.1 Introduction

Thwaites Glacier drains directly into the Amundsen Sea embayment (ASE) of West Antarctica and is undergoing rapid changes including grounding-zone retreat, dynamic ice thinning, and increased ice discharge into the ocean (Milillo et al., 2019; Rignot et al., 2019). The glacier catchment extends deep into the interior of the West Antarctic Ice Sheet (WAIS; Holt et al., 2006), indicating destabilization of Thwaites Glacier has the potential to trigger widespread collapse of the WAIS (Weertman, 1974; Schoof, 2007). Increased community efforts are now focused on improving predictability of how Thwaites Glacier will likely response to continued climatic warming, in particular for its ice shelf and grounding zone (Scambos et al., 2017). While numerous studies focus on ice-shelf and grounding-zone sensitivity to the incursion of warm, Circumpolar Deep Water (e.g., Joughin et al., 2014; Seroussi et al., 2017; Hoffman et al., 2019), less attention has been paid to understanding ice-shelf and grounding-zone behavior in response to subglacial meltwater drainage beneath and at the grounding zone of Thwaites Glacier.

Subglacial meltwater expulsion into the ocean and subsequent buoyancy-driven turbulence is linked to both enhanced ice melt at or near the grounding zone (Gourmelen et al., 2017; Wei et al., 2020; Nakayama et al., 2021) and ice-shelf basal channel formation (Le Brocq et al., 2013; Marsh et al., 2016). The seaward extension of subglacial channels carved upward into the ice-shelf base encourages concentrated melt by warm marine waters (e.g., Alley et al., 2016) and may lead to ice-shelf fracture (Vaughan et al., 2012; Alley et al., 2016; Dow et al., 2018) and ultimately collapse (Borstad et al., 2012, 2017). Persistent, channelized subglacial drainage at paleo-grounding zones is hypothesized to inhibit sediment deposition needed to construct stabilizing ice-marginal landforms (i.e., moraines and/or grounding zone wedges; Simkins et al., 2017, 2018). Additionally, records from the Ross Sea seafloor suggest grounding zones retreated

---

<sup>1</sup> APL: conceptualization, data curation, formal analysis, investigation, methodology, project administration, resources, software, visualization, writing – original draft. LMS: conceptualization, funding acquisition, methodology, project administration, resources, supervision, writing – review & editing. JBA: conceptualization, funding acquisition, methodology, project administration, writing – review & editing. RWC, AAL: investigation, resources, writing – review & editing. JSW, C-DH, JAS, RT, RDL, KAH, FON, AGCG: funding acquisition, project administration, writing – review & editing. LW: formal analysis, investigation, writing – review & editing.

<sup>2</sup> Co-author contributions denoted for Chapters 2, 3, and 4 follow the Contributor Roles Taxonomy (CRediT, <https://credit.niso.org/>)

greater distances when subglacial channels were actively draining, compared to retreat that occurred when channels were inactive (Simkins et al., 2021).

Today, geophysical and remote sensing observations support an active subglacial plumbing network beneath Thwaites Glacier (Schroeder et al., 2013; Smith, B.E. et al., 2017; Hoffman et al., 2020). Basal shear stress (Joughin et al., 2009) and regionally elevated geothermal heat flux (Damiani et al., 2014; Dziadek et al., 2021) contribute to meltwater production. Numerically estimated steady-state subglacial water fluxes within the Thwaites catchment range from  $\sim 1 \text{ m}^3 \text{ s}^{-1}$  to  $\sim 60 \text{ m}^3 \text{ s}^{-1}$  (Le Brocq et al., 2013). These values are similar to estimates of steady-state subglacial meltwater flux along the Siple Coast that reach the grounding zone through both distributed and channelized drainage pathways (Carter and Fricker, 2012). While no observational evidence of point-source meltwater delivery to the grounding line currently exists, subglacial hydropotential models predict persistent subglacial channels that drain at a few discrete locations along the grounding line (Le Brocq et al., 2013; Hager et al., 2022). Seaward of modern Thwaites Glacier, bathymetric channels connecting paleo-subglacial lake basins indicate subglacial water also flowed beneath the formerly-expanded Thwaites Glacier and neighboring Pine Island Glacier (Lowe and Anderson, 2003; Nitsche et al., 2013; Witus et al., 2014; Kuhn et al., 2017; Kirkham et al., 2019; Hogan et al., 2020a). However, the morphology of these bedrock channels is hypothesized to reflect high-magnitude drainage events over several glacial cycles (Kirkham et al., 2019), and therefore do not provide insight into frequency or magnitude of recent drainage events on decadal to millennial timescales.

Subglacially-sourced meltwater plumes mobilize and distribute glaciogenic sediments into the ocean. Sediment cores from the continental shelf can thus be used to provide details of meltwater drainage events that cannot be inferred from observational records or bathymetric landform analysis. Meltwater plume deposits on the continental shelf are characterized as silt-rich sediments with high water content and low biogenic and ice-rafted debris (IRD) content, low shear strength, and low magnetic susceptibility (Kirshner et al., 2012; Hillenbrand et al., 2013; Witus et al., 2014; Smith, J.A. et al., 2017; Streuff et al., 2017; Simkins et al., 2017; Prothro et al., 2018, 2020; Majewski et al., 2020). These properties allow for the distinction of meltwater plume deposits from subglacial, ice-proximal, and seasonally open-marine sediment facies. Incorporation of meltwater plume deposits into traditional facies models of glacier retreat has clarified a connection between subglacial hydrologic activity and grounding-zone position (Simkins et al., 2017, 2021; Prothro et al., 2018). This study employs a suite of sedimentological, geochemical, and statistical analyses of sediment cores from seaward of Thwaites Glacier to identify evidence of subglacial meltwater drainage events into the surrounding ocean. We seek not only to characterize styles of subglacial meltwater drainage that may be distributing sediments offshore of other Antarctic glaciers, but evaluate the relative persistence of meltwater drainage from Thwaites Glacier through the pre-satellite era. These advancements in knowledge will help illuminate connections between meltwater drainage and grounding-zone conditions, thereby broadening the framework within which contemporary subglacial hydrologic observations are interpreted.

## 2.2 Materials and Methods

The Thwaites Offshore Research project of the International Thwaites Glacier Collaboration conducted two cruises aboard the RVIB Nathaniel B. Palmer during the austral summers of 2019 and 2020 (*NBP19-02* and *NBP20-02*). High-resolution multibeam bathymetric and acoustic sub-bottom surveys were conducted on both cruises with a hull-mounted Kongsberg EM122 echo sounder at 12 kHz frequency (Figure 2.1; Hogan et al., 2020a) and a hull-mounted Knudsen Chirp 3260 3.5 kHz sub-bottom profiler, providing geomorphological and acoustic stratigraphic context for sediment cores used in this study. Sediment pockets in bathymetric lows and sediment drapes were targeted for coring. Based on core site locations, core recovery, and on-board core descriptions, five sediment cores recovered with a Kasten corer seaward of the Thwaites Glacier Tongue (TGT) and Eastern Ice Shelf (EIS) were selected to examine spatiotemporal evidence of meltwater drainage and associated sedimentation processes (Figure 2.1; Table 2.1). The cores were photographed, lithologically described, and sampled on board.

Bulk sediment samples for trace-elemental and grain-size analyses were taken at 10-cm depth intervals using plastic sampling tools from ~2 cm inward from the core barrel to avoid metal contamination. Archive trays from the cores are stored in the Antarctic Core Collection at the Oregon State University (OSU) Marine Geology Repository. A GEOTEK XZ system at the OSU repository was used to measure magnetic susceptibility (MS) with a point sensor at 1-cm resolution downcore. Computed tomography (CT) scans were acquired through the OSU College of Veterinary Medicine and grayscale images were processed using the SedCT package in Matlab (Reilly et al., 2017). Where CT imagery revealed suspected plume deposits and other distinct sediment types between 10-cm sampling intervals, additional 1-cm thick samples were collected and underwent the same suite of analyses described above.

Sediments were wet-sieved for calcareous foraminifera in 5- to 8-cm intervals. Where present, mixed-assemblage calcareous foraminifera, which are very rare in Antarctic shelf sediments, were utilized for radiocarbon dating with the MICADAS system at ETH Zurich (Wacker et al., 2010). Radiocarbon ages in  $^{14}\text{C}$  years were calibrated using the CALIB 8.2 Marine20 curve (Heaton et al., 2020) and corrected for marine reservoir effects using the age from live (mixed assemblage) calcareous foraminifera in seafloor sediments (1,117  $^{14}\text{C}$  years) from the area (Table 2.2). Collectively, these constraints provide an absolute age framework for which to interpret meltwater drainage persistence.

### 2.2.1 Grain-size and smear slide analyses

Laser diffraction particle analysis was carried out using a Bettersizer S3 Plus that is equipped with a green laser optimized for fine-grained sediments. Representative subsamples (~0.5 g wet sediment) were treated with sodium hexametaphosphate and allowed to deflocculate in deionized water for a minimum of 48 hours prior to analysis. A magnetic stir bar was used to create a homogenized slurry from which aliquots were pipetted into the Bettersizer S3 Plus

reservoir. Each aliquot run consisted of seven individual readings that were averaged and binned by cumulative volume percentages. The maximum (D100) and median (D50) grain size, along with other distribution percentiles, for each sample were identified by Bettersizer S3 Plus software and used to calculate grain-size statistics. Grain-size classifications and statistics follow Folk and Ward (1957). We note that, due to pipette width and instrument limitations, the grain-size measurements do not include material coarser than 3 mm and thus larger grains (i.e., clasts) are not represented in the grain-size distributions. This caveat reduces the efficacy of this method for capturing potential IRD. Interpretations of grain-size distributions are therefore supplemented with CT images, which fundamentally discern material based on density and allow us to comment on relative frequency of downcore IRD (cf. Cederstrøm et al., 2021).

Prior characterizations of meltwater deposits from Pine Island Bay (Witus et al., 2014) and Ross Sea (Simkins et al., 2017; Prothro et al., 2018) used a Malvern Mastersizer for grain-size analysis. In order to compare those deposits to sediments collected offshore from Thwaites Glacier, duplicate samples from the Ross Sea were run on the Bettersizer S3 Plus ( $n = 3$ ). Representative smear slide analysis of Thwaites Glacier sediment cores was conducted under plane-polarized light to characterize the general composition of the measured grain-size modes.

### *2.2.2 Physical and chemical analyses*

Shear strength was measured with a hand-held shear vane at ca. 10-cm depth intervals on board. Water content was determined on bulk sediment samples (minimum of 3.5 g wet sediment) by oven-drying for at least 48 hours at 60 °C and calculating the difference in weight percent. Dried samples were then powdered by gently crushing with a ceramic mortar and pestle and sieved through a 125-micron stainless steel mesh. Homogenized samples finer than 125  $\mu\text{m}$  were analyzed for trace and rare earth elements with x-ray fluorescence (XRF) using a ThermoFisher Scientific Niton XL5 Handheld Analyzer. While hand-held XRF analyzers are unable to measure elemental concentrations on discrete sediment samples with the precision of conventional XRF or other spectrometry methods (Dunnington et al., 2019; Hahn et al., 2019), the results allow comparison of general concentrations downcore and between cores. Furthermore, discrete XRF measurements allow for direct comparison of various measurements conducted on the same sediment samples and are less prone to porewater bias when compared to XRF scanner data. Instrument calibration and performance was tested using a NIST 2709 soil standard prior. The elemental concentrations in parts per million (ppm) were measured by taking the average of three energy spectra filters with a 90-second sampling window for each filter. For those elements used in analysis, two sigma values ranged from  $\pm 8.08\%$  to  $\pm 0.18\%$  (mean  $\pm 2.34\%$ ), with the exception of Ni which has two sigma values ranging from  $\pm 27.1\%$  to  $\pm 15.5\%$  in cores KC33 and KC08, respectively (mean  $\pm 18.5\%$ ). Discrete MS was measured with a Bartington MS2 dual-frequency sensor on the homogenized samples used for the XRF analyses. Readings were corrected for drift and sample mass, and the final values were used in statistical analysis.

### 2.2.3 Statistical analysis

To compare sedimentological and geochemical analyses between and within cores through a non-qualitative approach, principal component analysis (PCA) was conducted on all samples using the “prcomp” function in R. PCA is a statistical method useful in identifying trends and the factors driving variability within large, multivariate datasets. Input variables included physical sediment properties (water content, discrete MS), grain-size parameters, and trace element concentrations. All measurements input into this analysis were collected on the same sample or sub-sample at the University of Virginia. Variables were centered and scaled (i.e., normalized) within the code to prevent bias based on variable magnitude, and the package “factoextra” was used to create a biplot visualizing statistical results. Collectively, the results of PCA were interpreted with geochemical and physical sedimentological results to establish sediment lithofacies.

## 2.3 Results

### 2.3.1 Grain-size distributions

Grain-size distributions for all samples reveal striking consistency, with a prominent mode at approximately 5 microns (hereafter referred to as Mode 1) present in nearly all, and dominant in most, samples (Figure 2.2A). A secondary mode at 11 microns (Mode 2) also occurs in varying concentrations. Mode 2 typically increases at the expense of Mode 1 and comprises the highest volume percent in cores closest to the Thwaites Glacier ice-shelf margin (KC04, KC23; Figure 2.1B). Additionally, many sediment intervals feature a minor (less than 2 % by volume) sub-micron component. Coarse “tails” in the distributions, often interpreted in glaciomarine settings as IRD (e.g., Witus et al., 2014) are observed most commonly in cores closest to the ice-shelf margin and, in few discrete instances, in one relatively distal core (KC08). Overall, cores are dominated by fine silt and clay, and the relative contribution of the sand fraction is minimal and varies with proximity to the modern calving line. The instrument comparison conducted on meltwater deposits from the Ross Sea shows the Bettersizer was able to resolve the previously described 10-micron mode into a primary grain-size mode and secondary grain-size ‘shoulder’ identical in size and volume percent to those observed in this study (Figure 2.2B). Smear slides show that, in all cores, grain size Modes 1 and 2 are composed of terrigenous grains, and in-tact or fragmented microfossils are rare or absent except in some surface sediment samples (Figure 2.3). Observed mineral assemblages vary slightly between cores, but are in all cases dominated by low relief, transparent grains presumed to be quartz (Figure 2.3).

### 2.3.2 Sediment geochemistry

Downcore geochemistry reflects distinct geographic regions offshore of the eastern and western margins of Thwaites Glacier and variable proximity to the ice-shelf margin (Figure 2.4). Cores near the EIS are characterized by lower Ti and Sr, and elevated Th and Rb compared to those collected near the TGT. Zr and Rb appear strongly controlled by grain size, as more distal cores with very low sand fractions have higher Rb and lower Zr concentrations while ice-shelf proximal cores have the highest concentrations of Zr. Additionally, more ice-distal deposits have lower Ca and higher Fe concentrations than the ice-shelf proximal cores from the same geographic region. All cores have comparable concentrations of Cr, Ni, and V, trace elements common in intermediate and mafic minerals. KC04 shows a prominent enrichment of Ni at 150 cm that is not mirrored by other geochemical or sedimentological data. Ti content (ppm) in bulk sediment is also plotted against Th/Zr and Sr/Th, ratios of immobile trace elements that are unique for particular geologic settings and not significantly influenced by physical weathering processes (e.g., Hawkesworth et al., 1997; Figure 2.4B-C). Geographic clusters emerge, where data from cores collected from offshore either the TGT or the EIS plot close together (Figure 2.4C), as do samples within individual cores (Figure 2.4B-C). Core KC33 is the only exception, because the geochemical composition of some samples more closely resembles sediments from the EIS cores whereas others are geochemically more similar to that of the TGT cores (Figure 2.4B-C). While Th/Zr ratios for core KC23 are lower than ice-distal cores from the same region (Figure 2.4B), this is likely explained by the relatively elevated sand fraction throughout this core (Figure 2.2A) and a subsequent Zr enhancement (cf. Rothwell and Croudace, 2015).

### 2.3.3 Downcore physical properties and sedimentological structures

Core KC08 was collected from a deep trough west of the TGT and is largely composed of rhythmic layers of silt-rich sediments with high water content (max. 49 %, mean 40 %; Figure 2.5). Lithologic descriptions suggest the layers are normally graded, which is supported by grain-size distributions that show finer and coarser modes varying in volume percents (Figure 2.2A). Additionally, this core shows the greatest standard deviation of mean grain size ( $10.4 \mu\text{m} \pm 7.11$ ; Figure 2.5), reflective of grain-size variation within the graded layers. CT imagery clearly shows these graded silt layers and reveal layer thicknesses range from <0.5 cm to 8 cm (Figure 2.6A-B). We do not observe these graded silt layers in other sediment cores analyzed for this study. While overall sand content is low or zero (average 2.9 %), two exceptions that elevate mean grain size coincide with the bases of graded silt layers at 25-26 cm and 273-274 cm (11 % and 25 % sand, respectively; Figure 2.5). MS increases slightly downcore with occasional excursions and one prominent maximum at 233 cm, coincident with reduced water content within a discrete unit of stratified diamicton (Figure 2.5). A single radiocarbon date of 520 ( $2\sigma$  318-674) cal BP (Table 2.2) comes from an interval with several graded silt layers (52-60 cm; Figure 2.6A-B). Shear strength increases slightly downcore but does not exceed 2 kPa.

Core KC04, collected on bathymetric high H2 ~20 km from KC08, exhibits high variability in most measured properties (Figure 2.5). Water content is ~41 % in the upper 30 cm and decreases to ~26 % downcore with the exception of two discrete intervals (88-89 cm, 210-212 cm) where water content increases to ~35 %. MS fluctuates downcore, reflective of the highly variable sand fraction (range: <1 – 34 %), while mean grain size shows little downcore variability ( $13.7 \mu\text{m} \pm 4.38$ ). This matrix material is poorly sorted (mean 1.84) with a maximum of 3.21 at 46-47 cm (very poorly sorted). Core stratigraphy reveals several sediment types including massive and stratified diamictons (Figure 2.6A). Fine-grained, parallel to sub-parallel laminations and beds ranging from <1 cm to ~10 cm in thickness are observed within stratified diamicton, as are gravel and pebbles oriented with their long axes parallel to lamination (Figure 2.6C). Pebbles largely disappear upcore from the most poorly-sorted interval at 46-47 cm. Dates from three intervals between 130 cm and 62 cm core depth span 490 ( $2\sigma$  302-654) to 270 ( $2\sigma$  26-478) cal BP and are in stratigraphic order (Table 2.2). Shear strength increases slightly downcore from ~0.25 kPa to 2 kPa.

Core KC33, collected farthest offshore of the EIS, is characterized by high water content (range, 37-52 %; mean 46 %) and low shear strength that increases slightly downcore, coincident with a modest decrease in water content (Figure 2.5). The mean grain size hardly varies downcore ( $7.37 \mu\text{m} \pm 1.77$ ) although volume percent of Mode 2 grains increases slightly upcore from ~50 cm (Figures 2.2A, 2.5). Sediments are, on average, better sorted than the matrix material of ice-proximal diamictons (mean 1.29). The core base shows faint, irregular lamination that transitions into sediment which appears bioturbated and mottled from ~210 cm core depth to the core top (Figure 2.6D). MS varies moderately, but remains generally low except for peaks at 217 cm and 257 cm that align with coarse-grained layers apparent in the CT scan (Figure 2.6A). Calcareous microfossils from the core base (290-295 cm) yield a single date of 9,630 cal BP ( $2\sigma$  9325-9967).

Sediments in core KC67 from the eastern side of the EIS have high water content (range, 42-51 %; mean, 46 %), similar to cores KC33 and KC08, and consistently low MS (Figure 2.5). Shear strength fluctuates between 0 and 2.5 kPa and increases slightly downcore, while the average grain size remains remarkably uniform throughout ( $5.53 \mu\text{m} \pm 0.28$ ). Sediments show strong laminations with sharp contacts, interspersed with scarce IRD below ~130 cm core depth (Figure 2.6E). Above this depth, sediments are heavily bioturbated. The clear lamination suggests alternations between thin coarser- and finer-grained layers, but the 1 to 2-cm thickness (i.e., depth range) of the grain-size samples is too large to resolve grain-size differences between individual laminae (Figure 2.2A). Overall, KC67 exhibits the highest sorting values that are consistent downcore (mean 1.09; Figure 2.5).

East of the EIS, core KC23 consists predominantly of massive diamicton (Figures 2.5, 2.6A, 2.6F). The diamicton below 15 cm core depth is characterized by low water content (mean 18 %), fluctuating MS, and a strikingly consistent grain-size matrix ( $11.5 \mu\text{m} \pm 1.29$ ; Figure 2.5). Mean sorting of the diamicton (1.81) is very similar to the matrix material of KC04. Between ~8 and 15 cm core depth, a normally-graded, oblique sand bed ~5 cm thick separates the diamicton

from overlying silty-clays with notably higher water content (average 39 %). MS is lower in the silty-clay unit than in the sand bed and the diamicton. Shear strength through the diamicton is low ( $\leq 1$  kPa) but increases up to 4 kPa below 140 cm (Figure 2.5).

#### 2.3.4 Principal component analysis

The first two principal components (PC1 and PC2) account for 40.4 % and 27.1 % of variability in the dataset, respectively. Samples are plotted along PC1 and PC2 axes, along which sample positioning is controlled by the magnitude and relative sign (i.e., positive or negative) of the eigenvectors driving the variance (Figure 2.7). For PC1, the eigenvectors for Fe, V, water content, and clay percent push samples into negative PCA space, and sand percent, D100, D50, and Ca drive samples into positive PCA space. Negative space of PC2 is largely influenced by Rb, Th, Ti, and clay and silt percentages, while positive PC2 space is defined by Sr, MS, and Zr. Grain-size parameters appear to be the dominant control over PC1, separating finer-grained samples with higher water content, total Fe, and clay-sized grains from samples with higher sand fraction, more variable sorting, and overall coarser grains. While grain-size parameters also influence PC2, geochemistry seems to play a more important role as cores are divided by geographic region and presumably by sediment source. Cores KC08 and KC04 straddle the zero line of PC1, indicating these cores contain intervals deposited by variable sedimentary processes. In contrast, KC33 and KC67 plot entirely in negative PC1 space with the exception of two sample outliers in KC33. Core KC23 samples cluster tightly except for sample outliers including the surface sediments (Figure 2.7, denoted by an enlarged icon) that plot in negative PC1 space and others that plot high on the PC1 axis. These outliers correspond to samples collected from the sorted sand bed (Figures 2.5, 2.6A).

#### 2.3.5 Facies Interpretation

The multi-proxy analysis employed in this study, including CT imagery and the integration of PCA, is valuable in characterizing and distinguishing between sediment types recovered offshore of Thwaites Glacier. We interpret PC1 as distinguishing glacially-sourced sediment (i.e., via ice rafting, basal melt out, gravity flows, or till from the glacier base) from sediment transported by subglacial meltwater processes, including within plumes emanating from the grounding line. High water contents, clay percentages, and Fe contents are shown to be statistically important characteristics for identifying meltwater plume deposits (Figure 2.7), largely consistent with studies characterizing such deposits from the Antarctic continental shelf (e.g., Witus et al., 2014; Simkins et al., 2017; Prothro et al., 2018). Sediment samples from KC33 and KC67 plot almost exclusively in negative PC1 space (Figure 2.7), and thus we interpret these cores to reflect pure meltwater endmembers that manifest as both laminated and bioturbated sediment facies.

Two diamicton facies, massive and stratified, were recovered in ice-shelf proximal cores



KC04 and KC23. Additionally, a discrete unit of stratified diamicton is observed in the lower part of KC08 (Figure 2.6A). Clast orientation in the stratified diamicton, along with observed soft-sediment deformation and sediment draping above clasts, is characteristic of ice rafting, where debris released from the base of floating ice settles through the water column. The sediments comprising laminations and beds in stratified diamicton are rich in Mode-1 grains (Figure 2.3A). In glaciomarine settings, diamictons indicate deposition subglacially or through processes at or near the grounding zone (e.g., Domack and Harris, 1998; Prothro et al., 2018; Smith et al., 2019). Because this study is focused on sediments that inform meltwater processes, we do not explore the specific depositional processes responsible for recovered diamictons in depth.

Much of the sediment from KC08 plots in negative PC1 space (Figure 2.7) and shares similarities with sediments from KC33 and KC67, including high water contents and high Fe contents (Figure 2.5). We therefore interpret core KC08 as consisting of primarily meltwater-derived sediments, composing a normally graded silt facies that reflects deposition from hyperpycnal flows, possibly as turbidity currents. To further characterize this unique facies offshore of the TGT, we examine the downcore frequency of different sediment types found in cores KC08 and KC04. Within units of stratified diamicton, both beds and individual, continuous laminae are counted collectively as ‘laminations’ because of the similarity in grain-size. Laminae and normally-graded silt layers are counted in 10-cm intervals, and layers that cross an interval boundary are counted in both intervals (Figure 2.8A). The abundance of graded silt layers within KC08 fluctuates slightly but remains common throughout (mean 4.7 layers per 10-cm depth intervals), while few instances of similar layers are observed in the upper 120 cm of KC04 (Figure 2.8A). We also quantify downcore variability in thickness of graded silt layers in KC08, and find that 75 % of the layers are 4 cm thick or less, while outliers with thicknesses between 4.5 and 8 cm thick are concentrated in the upper 70 cm of the core (Figure 2.8C).

## 2.4 Discussion

Surface sediments throughout Pine Island Bay, which receives drainage from both Thwaites and Pine Island glaciers, are dominated by meltwater plume deposits (Witus et al., 2014), indicating the sustained and widespread importance of sediment delivered by meltwater drainage into the ASE. Meltwater deposits are particularly thick in basins and deep channels on the inner continental shelf (Lowe and Anderson, 2003; Nitsche et al., 2013; Kuhn et al., 2017), and become thicker with increasing proximity to the modern grounding zone of Pine Island Glacier (Witus et al., 2014). This spatial pattern of meltwater deposits indicates uniform dispersal by sediment-laden plumes, and accumulation of plume deposits in bathymetric lows, possibly remobilized across the seafloor by hyperpycnal flows or downslope gravity flow processes (e.g., turbidity currents). In Marguerite Bay (Kennedy and Anderson, 1989) and the in Ross Sea (Simkins et al., 2017; Prothro et al., 2018), similar meltwater deposits overlie proximal glaciomarine sediments and are capped by or interspersed with distal, diatom-bearing

glaciomarine muds. This stratigraphic sequence is characteristic of the most recent deglaciation of the Antarctic continental shelf and onset of open-marine conditions, typically as the result of rapid grounding-zone retreat (Bentley et al., 2011; Bart et al., 2017; Prothro et al., 2018). However, unique to Pine Island Bay is the absence of the diatomaceous mud which is not observed in any cores described to date (Lowe and Anderson, 2003; Kirshner et al., 2012; Hillenbrand et al., 2013; Nitsche et al., 2013; Smith et al., 2014; Witus et al., 2014; Kuhn et al., 2017), and is similarly absent in the cores used in this study. Instead, surface sediments from each core analyzed here are characterized by high water content (Figure 2.5), a prominent Mode 1 (Figure 2.2A), and plot in negative PC1 space (Figure 2.7), indicating that meltwater drainage is the primary mode of sedimentation seaward of contemporary Thwaites Glacier.

Here, we discuss the source of meltwater plume deposits offshore Thwaites Glacier, the variability in styles of meltwater drainage, and consider processes associated with meltwater evacuation, as well as floating ice and oceanographic responses. Calibrated radiocarbon dates presented here (Table 2.2) are useful in conjunction with core stratigraphy for evaluating persistence and frequency of subglacial meltwater drainage through time (Figure 2.6A). Radiocarbon at the base of core KC33, the northern-most core in this study, suggests sediment accumulation on the H1 high spanning the last ~9,000 to 10,000 years (Table 2.2). This is consistent with regional reconstructions of deglaciation (Larter et al., 2014) and radiocarbon dates that indicate grounding-zone retreat from the H1 high by ~10,300 years ago (Hillenbrand et al., 2017; Hogan et al., 2020a). In the vicinity of Thwaites Glacier, sedimentation rates for similar glaciomarine facies range from  $0.095 \text{ cm yr}^{-1}$  beneath the Pine Island Ice Shelf (Smith et al., 2019 and references therein) to  $0.02\text{-}0.086 \text{ cm yr}^{-1}$  for core NBP99-02 TC49 which sampled meltwater plume deposits in inner Pine Island Bay (Figure 2.1B; Witus et al., 2014). Altogether, these data allow for meaningful considerations of sediment depositional processes through time.

#### *2.4.1 Source and grain-size production of meltwater deposits*

Rates of sub-ice shelf melt from observations ( $17.7 \text{ m a}^{-1}$ ; Rignot et al., 2013) and models ( $11.6 \text{ m a}^{-1}$ ; Pelle et al., 2019) of Thwaites Glacier implicate the formation of buoyant, meltwater plumes without a subglacial origin. Such plumes would, similarly, influence stratification and ocean circulation in an ice-shelf cavity and could entrain and transport debris melted out from the ice-shelf base. Albeit dependent on basal debris thickness and ice-shelf melt rates, debris advected by basal ice is largely melted out within the first few kilometers of the grounding line (e.g., Prothro et al. 2018), restricting the area over which sediment entrainment by ice-shelf melt plumes would be expected. Downstream refreezing would decrease the carrying capacity of sediment-laden plumes and promote deposition beneath the ice shelf. Furthermore, the rate at which a plume entrains ambient water in an ice-shelf cavity (in this instance, warm CDW at depth) is a function of plume speed (Jenkins, 2011). Discharge of subglacial meltwater, therefore, has an inherently greater capacity to drive sub-ice shelf melt through entrainment of warm water than plumes that originate in ice-shelf cavities. Given the widespread distribution of

meltwater plume deposits and the distance of meltwater endmember core sites from the recent grounding-line and ice shelf-margin positions (Figures 2.1B, A2.2), a subglacial source better explains these silt-rich deposits than a basal-ice shelf source. We acknowledge, however, that Mode 1 grains mobilized in sub-ice shelf plumes and deposited some distance offshore Thwaites Glacier would have the geochemical signatures as plume deposits sourced from the subglacial environment.

The unique geochemical signals observed in sediment cores offshore of the EIS and TGT reflect spatial variations in source material, and therefore subglacial geology, beneath the eastern and western portions of Thwaites Glacier (Figure 2.4). This is consistent with geochemical fingerprinting of fine-grained surface sediments from the inner shelf of Pine Island Bay (Simões Pereira et al., 2018). Planar, seemingly non-erosional contacts and the absence of sand-rich, winnowed deposits in ice-distal cores suggest marine currents have not remobilized sediments deposited at these core sites (Figure 2.6). Similarly, geochemical consistencies between diamictons recovered near the ice-shelf margin and meltwater plume deposits further offshore (Figure 2.4) imply Mode-1 rich sediments offshore Thwaites Glacier were not delivered to core sites by currents originating offshore another glacial system.

The ubiquity of grain-size Modes 1 and 2, despite spatial variations in subglacial geology, strongly supports that grain-size production of meltwater deposits is a process-controlled, rather than a source-controlled, phenomenon. Previous studies have inferred subglacial till as the source of meltwater plume deposits based on a shared grain-size mode (e.g., Witus et al., 2014; Simkins et al., 2017; Prothro et al., 2018), a relationship that is similarly evident from grain-size distributions of ice-shelf proximal diamicton and ice-distal sediments in this study (Figure 2.2A). Grain surface micromorphology of meltwater deposits from Pine Island Bay shows evidence of glacial influence without significant surface alteration by hydrologic transport (Witus et al., 2014), suggesting the grain-size distribution of meltwater deposits reflects the process of glacial abrasion rather than size reduction through meltwater transport. The sedimentological likeness of Thwaites Glacier meltwater deposits to those produced by other Antarctic glaciers and paleo-ice streams across a range of space and time implies widespread and consistent subglacial erosion and hydrologic transport to the Thwaites Glacier grounding zone.

#### *2.4.2 Spatial variability in subglacial meltwater plume deposition*

The stratigraphy revealed by CT imagery suggests contrasting depositional processes associated with subglacial meltwater drainage offshore from the TGT and EIS (Figure 2.9). Cyclical, normally-graded silt layers dominated by meltwater deposits indicate persistence of sedimentary processes largely unique to core site KC08 (Figure 2.8A). Calcareous benthic foraminifera are found in several discrete intervals of KC08, but rarely in sufficient numbers for radiocarbon dating. The corresponding layers could reflect infrequent gravitational downslope sediment transport (e.g., Smith et al., 2009) as the core site lies approximately 400 m below the local carbonate compensation depth (Hillenbrand et al., 2003; Majewski, 2013). Alternatively,

preservation of calcareous foraminifera could result from rapid sediment deposition that limited exposure to corrosive bottom waters. Contacts separating normally-graded silt layers are sharp but appear non-erosive, suggesting insufficient depositional energy to erode underlying sediments. Additionally, intervals with continuous bands of IRD (Figure 2.6A) possibly mark periods of meltwater drainage cessation when sedimentation was temporarily dominated by IRD deposition (e.g., Prothro et al., 2018). These combined observations support the interpretation that the normally-graded silt layers in core KC08 were deposited by hyperpycnal flows generated during episodic meltwater drainage events of varying magnitudes (Figure 2.9B). If we hypothetically consider these silt layers in the context of a fixed grounding-zone position, which can be inferred from the presence of a grounding zone wedge on the northern crest of H2 (Hogan et al., 2020a), layer thickness between 0.5 and 4 cm may reflect punctuated, lower-magnitude meltwater discharge, as this describes 75 % of such units (Figure 2.8C). Hence, the thicker (4.5-8 cm) normally graded silt layers may result from relatively higher-magnitude drainage events. In the context of a grounding zone that has been retreating landward, thicker graded silt layers still implicate higher-magnitude drainage events, as in this scenario the source of drainage is moving progressively further from the core site.

Sediments in core KC04, recovered from within a ~60 m deep channel on the H2 high (Figure 2.1), record the recent unpinning of the TGT (Rignot et al., 2011; Hogan et al., 2020a) and the transition to seasonally open-marine conditions at this core site. The stratified diamictos comprising most of the sediments in this core (Figure 2.6A, 2.8A) feature laminated and stratified intervals with large clasts and a matrix dominated by Mode 1, and are consistent with deposition in an ice-proximal environment (e.g., Prothro et al., 2018; Smith et al., 2019). Estimated sedimentation rates of stratified diamicton in core KC04 (between 62 and 130 cm core depth; Table 2.2, Figure 2.6A) are an order of magnitude higher than sub-ice shelf and grounding-zone distal sediment facies observed in the region (Witus et al., 2014; Smith et al., 2019). Clast orientation is parallel to bedding (Figure 2.6C), which along with observed soft-sediment deformation and sediment draping above clasts is characteristic of IRD released from the base of floating ice settling through the water column. The prevalence of concentrated meltwater silt laminae within clast-rich diamicton in core KC04 may record subglacial meltwater drainage beneath this region of western Thwaites Glacier when the grounding zone was nearer to the core site (Figure 2.9B). Lithology transitions upcore of ~30 cm (Figures 2.5, 2.6A) from stratified diamicton to laminated and bedded sediments with IRD-rich layers. These sediments are characterized by higher water content, finer mean grain size, and better sorting compared to the diamicton downcore (Figure 2.5), all of which are consistent with meltwater plume deposition.

Pervasive bioturbation in meltwater endmember core KC33 is consistent with deposition in an open-marine setting. Various configurations of the TGT over the last ~12 years, prior to calving of iceberg B22, confirm open-marine conditions at the core site (cf. MacGregor et al., 2012; Figure A2.3). Interestingly, the source of detritus in core KC33 appears to shift upcore from material originating from beneath eastern Thwaites Glacier to material from below western

Thwaites Glacier (Figures 2.4, 2.6A). This geochemical shift is not mirrored by substantial changes in grain size or other physical properties (Figure 2.5), suggesting consistent depositional processes for the sediments recovered at this site. Sediment mixing by bioturbation does not explain this shift, as the preserved laminae at the core base and the overlying bioturbated sediments have a distinct geochemical composition (mean Sr/Th from 250 cm core depth to core base = 6.4) from bioturbated sediments at the core top (mean Sr/Th from core top to 52 cm core depth = 8.3; Figure 2.6A). Given the strong meltwater signature of the sediments, we interpret the shift in geochemical signature to indicate rerouting of subglacial drainage beneath or emanating from Thwaites Glacier. Subglacial channel reorganization may be driven by changes in subglacial hydropotential, resulting from changes in glacier geometry (e.g., Carter et al., 2013) or supply of basal meltwater to the grounding zone (Simkins et al., 2021). Whether this shift in source material in KC33 reflects a migration or shutdown of a former meltwater drainage pathway, or the development of a new preferential drainage pathway cannot be constrained. A change in sediment source could also result from blocking or siphoning of sediment-laden meltwater plumes by the rugged bathymetry on the inner shelf seaward of Thwaites Glacier. Mean grain size increases slightly in the upper ~40 cm of the core, which may suggest strengthening of ocean currents, but this grain-size change doesn't occur contemporarily with the geochemical change. Stronger currents transporting meltwater plume deposits from offshore western Thwaites Glacier to the H1 high therefore does not explain this observed change in source material. These findings from KC33 provide evidence for a dynamic subglacial hydrologic network beneath Thwaites Glacier over the last ~10,000 years and implicate drainage reorganization in association with major ice-configuration changes.

Structurally, the laminations defining over half of the sediments in core KC67, and the lowermost part of core KC33, resemble those of modern sub-ice shelf sediments recovered from below the Pine Island Glacier ice shelf (Smith, J.A. et al., 2017), paleo-sub ice shelf sediments in the Ross Sea (Simkins et al., 2017; Prothro et al., 2018), and sediments offshore the eastern Antarctic Peninsula (Subt et al., 2017) and of Ryder Glacier in Greenland (O'Regan et al., 2021). The consistency of laminae thicknesses in KC67 (Figures 2.6A, 2.6E) suggests a pulsing outflow of sediment-laden subglacial meltwater while the uniform downcore geochemistry (Figure 2.4) implies drainage along a persistent subglacial pathway. Hydropotential calculations predict regionally-significant fluxes of subglacial meltwater to the grounding zone ~50 km from the site of core KC67 (Figure 2.1B; Le Brocq et al., 2013). This suggests that lateral plume migration and interactions between sediment-laden plumes and ocean currents may exert important controls on meltwater deposit distribution offshore the EIS. Preservation of laminations in KC67 and lowermost KC33, which may be destroyed by bioturbation following ice-shelf retreat (Jung et al., 2019), supports deposition beneath a perennial ice canopy – floating ice that may include an ice shelf, ice mélange, and/or fast ice (cf. Milliken et al., 2009; Minzoni et al., 2015; Lamping et al., 2020). No age constraints are available for core KC67, although nearby core NBP99-02 TC49, which consists of similar meltwater plume deposits (Figure 2.1B; Unit 1 from Witus et al., 2014) that accumulated at ~0.086 cm yr<sup>-1</sup>. While the grounding-zone position is not assumed to

be static through the deposition of meltwater-derived sediments in KC33 and KC67, the absence of diamictons and general lack of IRD indicate a depositional environment consistently seaward of the sub-ice shelf basal debris zone (Smith et al., 2019; Prothro et al., 2018). The transition from the laminated to bioturbated facies above ~130 cm core depth occurs without major changes in grain size (Figure 2.5), suggesting suspension settling from buoyant meltwater plumes remains the primary mechanism of sedimentation (Figure 2.9A). Individual burrows are observed within laminated sediments as deep as 190 cm in this core (Figure 2.6A) which might indicate the presence of infaunal benthic organisms coeval with meltwater drainage beneath a floating ice canopy.

The inferred spatial variation in subglacial drainage style is intriguing, as floating ice and grounding-zone characteristics of the eastern and western parts of Thwaites Glacier also exhibit unique, albeit connected, patterns of behavior (Schroeder et al., 2016; Milillo et al., 2019; Miles et al., 2020; Alley et al., 2021). Overall, meltwater drainage delivering detritus offshore the slow-flowing EIS is characterized as low-magnitude, yet persistent, with important implications for nutrient supply to marine ecosystems (Gerringa et al., 2012; Vick-Majors et al., 2020). Offshore the TGT, extending from the fast-flowing central axis of the glacier, stratified diamictons and normally-graded silts with occasional occurrence of IRD-bearing layers implicate meltwater drainage preceded floating ice-tongue (or ancestral ice shelf) retreat and a relatively recent increase in intensity of meltwater discharge events and volume of freshwater in the ice-shelf cavity.

#### *2.4.3 Connection of meltwater plumes to the contemporary ice-ocean system*

Release of subglacial meltwater into the ocean is thought to initiate hyperpycnal flows through rapid sediment loading (e.g., Noormets et al., 2009; Sutherland et al., 2020; King et al., 2022). Although such interpretations are largely based on findings from the continental shelf edge and uppermost continental slope, the relative relief of H2, the established position of grounded ice on this high, and presence of sediment fans on its northern flank (Hogan et al., 2020a) suggests similar processes are feasible close to Thwaites Glacier (cf. Dowdeswell et al., 2015). In flume experiments, hyperpycnal currents initiated by convective sedimentation (i.e., driven by suspension settling) are most likely to form when the buoyant inflow is carrying a greater particle load (Davaranah Jazi and Wells, 2020). Conceptually, the concentration of suspended detritus increases with discharge and hydraulic pressure gradients in subglacial channels (e.g., Alley et al., 1997; Swift et al., 2005; Gimbert et al., 2016), thus supporting a possible connection between observed thicker normally-graded silt layers and relatively higher magnitude of drainage events with heightened particle load mobilized by plumes. The intervals of KC08 that bear few calcareous microfossils, including foraminifera, suggest processes including meltwater-induced hyperpycnal transport, recycling and reworking by glacial advance and subsequent transport as IRD or buoyant interflows (i.e., plumes) are all possible. The single age of 520 cal BP ( $2\sigma$  318-674) from 52-60 cm core depth therefore provides a maximum

depositional age, and the concentration of relatively thicker graded silt layers above this depth may imply an increase in magnitude of drainage events in recent centuries.

Based on the spatial distribution of core sites and collective data presented here, we find evidence that plume deposits blanket the upper 5-10 cm of seafloor along the EIS and TGT. Thickness of deposits increases substantially (i.e., 3+ meters; the thickness of meltwater endmember cores) with increasing distance from the ice margin. These results suggest that contemporary plumes transport suspended detritus between 5 and 66 km from grounded ice to these core sites (Figure A2.2). Plume deposits on shallow topographic highs (<400 m water depth) and in deep troughs (>1000 m water depth) indicate plumes travel at relatively shallow depths in the water column, consistent with observations of the glacial meltwater-enriched layer in the ASE (Biddle et al., 2019). Furthermore, recent oceanographic work has detected fresher, glacial meltwater emanating from beneath the TGT (Wåhlin et al., 2021). This water is routed seaward toward the trough from which KC08 was recovered (Figure 2.1B; Wåhlin et al., 2021). While the source is presumed to be sub-ice shelf and/or grounding-zone ice melt, the sedimentary evidence of meltwater-derived deposition in cores KC04 and KC08 suggests subglacial drainage is an important contributor to this freshwater signal. Conversely, the substantial inflow of warm water to the east of H2 (Figure 2.1B; Wåhlin et al., 2021) supports the likelihood of enhanced turbulent mixing with fresh meltwater outflow along the grounding zone of western Thwaites Glacier, as is recently suggested for neighboring Pine Island Glacier (Nakayama et al., 2021). Numerical modelling of channelized drainage pathways beneath Thwaites Glacier predicts persistent drainage that discharges beneath the TGT (Hager et al., 2022). In some instances, these predicted locations of channelized drainage coinciding with grounding-zone embayments, which has also been observed in bathymetric records from the Ross Sea (Simkins et al., 2018).

Release of large quantities of freshwater and sediment into the marine system from paleo-subglacial basins can occur due to changes in subglacial hydraulic conditions (Lowe and Anderson, 2003; Nitsche et al., 2013; Witus et al., 2014; Kuhn et al., 2017; Simkins et al., 2017; Prothro et al., 2018). Bathymetry in the modern Thwaites ice-shelf cavity inferred from airborne gravity measurements reveals isolated basins (Millan et al., 2017; Jordan et al., 2020) similar in scale to those seaward of the grounding zone (Nitsche et al., 2013; Hogan et al., 2020a) in which subglacial meltwater is likely to have ponded (Witus et al., 2014; Kuhn et al., 2017; Kirkham et al., 2019). It is possible that these paleo-subglacial basins now beneath the contemporary ice tongue served as reservoirs for subglacial meltwater and sediment, and that higher-magnitude drainage events responsible for thicker graded silt packages were triggered by grounding-zone retreat. This model is also called on to explain the extensive meltwater facies observed seaward of Pine Island Glacier (Witus et al., 2014) and in association with previously expanded ice streams elsewhere, such as in Marguerite Bay (Anderson and Fretwell, 2008). The role of basins as reservoirs of subglacial meltwater helps resolve discrepancies between higher-magnitude drainage events implied by the sediment record and annual estimates of subglacial meltwater production within the Thwaites Glacier catchment (Joughin et al., 2009; Le Brocq et al., 2013;

Kirkham et al., 2019).

Subglacial lakes and channelized and distributed drainage beneath Thwaites Glacier have been inferred from airborne and on-ice geophysical investigations (Schroeder et al., 2013, 2016; Clyne et al., 2020) and remote sensing data (Smith B.E. et al., 2017; Hoffman et al., 2020). We can envision a subglacial plumbing network wherein efficiency and connectivity increase downstream with increasing basal water and ice-surface slope (cf. Schroeder et al., 2013). With the integration of sediment core interpretations, we hypothesize these ‘higher order’ channels transport detritus characterized by Mode 1 in suspension to the grounding zone and release it into the marine environment within discrete meltwater plumes. Channelized subglacial drainage could also be responsible for the distinct and consistent geochemical signal of meltwater plume deposits observed offshore from the EIS and the TGT (Figure 2.4). Such a conceptual model is in line, both in scale and in space, with outputs from recent hydrologic modeling studies predicting subglacial meltwater pathways and channelized drainage beneath past and modern Thwaites Glacier (Kirkham et al., 2019; Hager et al., 2022). While the ‘cascading’ of subglacial water between lake basins upstream of the modern grounding zone (Smith B.E. et al., 2017) is not associated with significant changes in ice-flow dynamics (Hoffman et al., 2020), the release of such volumes of water to the grounding zone, where it could induce a dramatically different ice response, has not yet been observed. Catchment-wide estimates of basal melt production beneath Thwaites Glacier in its modern (Joughin et al., 2009) and Last Glacial Maximum (Kirkham et al., 2019) configurations vary between  $\sim 5\text{-}12 \text{ km}^3 \text{ a}^{-1}$ ; subglacial meltwater pooling and episodic evacuation from such reservoirs may be responsible for triggering downslope gravity flows and producing the thicker graded silt layers recovered offshore the TGT. As grounding-zone retreat of Thwaites Glacier is expected to continue through the coming decades (Joughin et al., 2014; Seroussi et al., 2017; Yu et al., 2018), changes in subglacial hydraulic potential may cause the release of increasing amounts of freshwater from upstream reservoirs, leading to potential amplification of existing drivers of submarine ice melt and delivery of sediments to the ocean.

## 2.5 Conclusion

Sedimentary evidence seaward of Thwaites Glacier confirms the existence and persistence of a frequently active and historically long-lived subglacial hydrologic system. We find quantitative and qualitative evidence that sediments transported in, and deposited from, meltwater plumes generated beneath Thwaites Glacier are not only similar to those extinct sedimentary systems described offshore from other Antarctic glacier systems, but are also suggestive of subglacial erosive and/or hydrologic processes that occur independent of subglacial geology. Geochemical signatures demonstrate the utility in evaluating meltwater drainage persistence, or transience, of subglacial drainage pathways through time. We identify sedimentary evidence that suggests an increase in magnitude of meltwater drainage beneath the TGT in recent centuries, and speculate that subglacial drainage may have preceded or accompanied recent ice-tongue unpinning. Drainage patterns inferred in association with



Western Thwaites Glacier differ from those of Eastern Thwaites Glacier, where persistent, low-magnitude meltwater drainage is long-lasting, yet transient in its preferred pathways. The evidence of persistent drainage beneath floating ice underscores the potential for turbulent mixing at the grounding zone to be an important factor for the Thwaites Glacier system. Omission of processes related to subglacial meltwater drainage from models of grounding-zone retreat (Yu et al., 2018), calculations of ice-shelf melt rates (Seroussi et al., 2017), evaluations of ice-shelf stability (Alley et al., 2021), and flux of freshwater into the Southern Ocean (Adusumilli et al., 2020) likely leads to inaccurate estimations and results. In the context of several prior studies presenting evidence of active subglacial drainage accompanying and preceding grounding-zone retreat, our results demonstrating persistent drainage of subglacial meltwater in recent millennia are potentially another ominous signal pointing toward the impending retreat of Thwaites Glacier.

**Table 2.1.** Location, water depth, and recovery of the five Nathaniel B. Palmer (NBP) cores investigated in this study. Bathymetric highs H2 and H1 as defined by Hogan et al. (2020a). KC = Kasten core. TGT = Thwaites Glacier Tongue; EIS = Eastern Ice Shelf.

Cruise	Core	Latitude °S	Longitude °W	Water Depth m	Recovery cm	Geographic Region
NBP19-02	KC08	74.94	107.38	1186	297	~20 km offshore TGT; deep trough
NBP19-02	KC04	74.95	106.88	469	252	West of TGT; localized basin on H2 high
NBP20-02	KC33	74.64	106.18	397	297.5	Thwaites EIS; northwest corner of H1 high
NBP20-02	KC67	74.84	104.46	613	297	Bathymetric high east of Thwaites EIS
NBP19-02	KC23	75.07	104.23	677	213.5	Thwaites EIS corner

**Table 2.2.** Raw and calibrated radiocarbon dates. Calibration was performed using Marine20 in CALIB v.8.2. A marine reservoir age of 1,117 <sup>14</sup>C years from living (rose bengal stained) mixed-assemblages of foraminifera in surface sediments of core NBP19-02 MC16 was used to obtain a  $\Delta R$  value of 617 (Figure 2.1B).

ETH Lab ID	Cruise	Core	Interval cm	<sup>14</sup> C Age yr BP	CALIB Age cal yr BP	CALIB Age 2σ cal yr BP	Dated Material
105650	NBP19-02	KC04	62-70	1430 ± 90	270	26-478	Calcareous foraminifera
105651	NBP19-02	KC04	92-100	1630 ± 50	450	282-622	Calcareous foraminifera
105652	NBP19-02	KC04	122-130	1675 ± 60	490	302-654	Calcareous foraminifera
105656	NBP19-02	KC08	52-60	1705 ± 60	520	318-674	Calcareous foraminifera
113920	NBP20-02	KC33	290-295	9695 ± 90	9630	9325-9967	Calcareous foraminifera

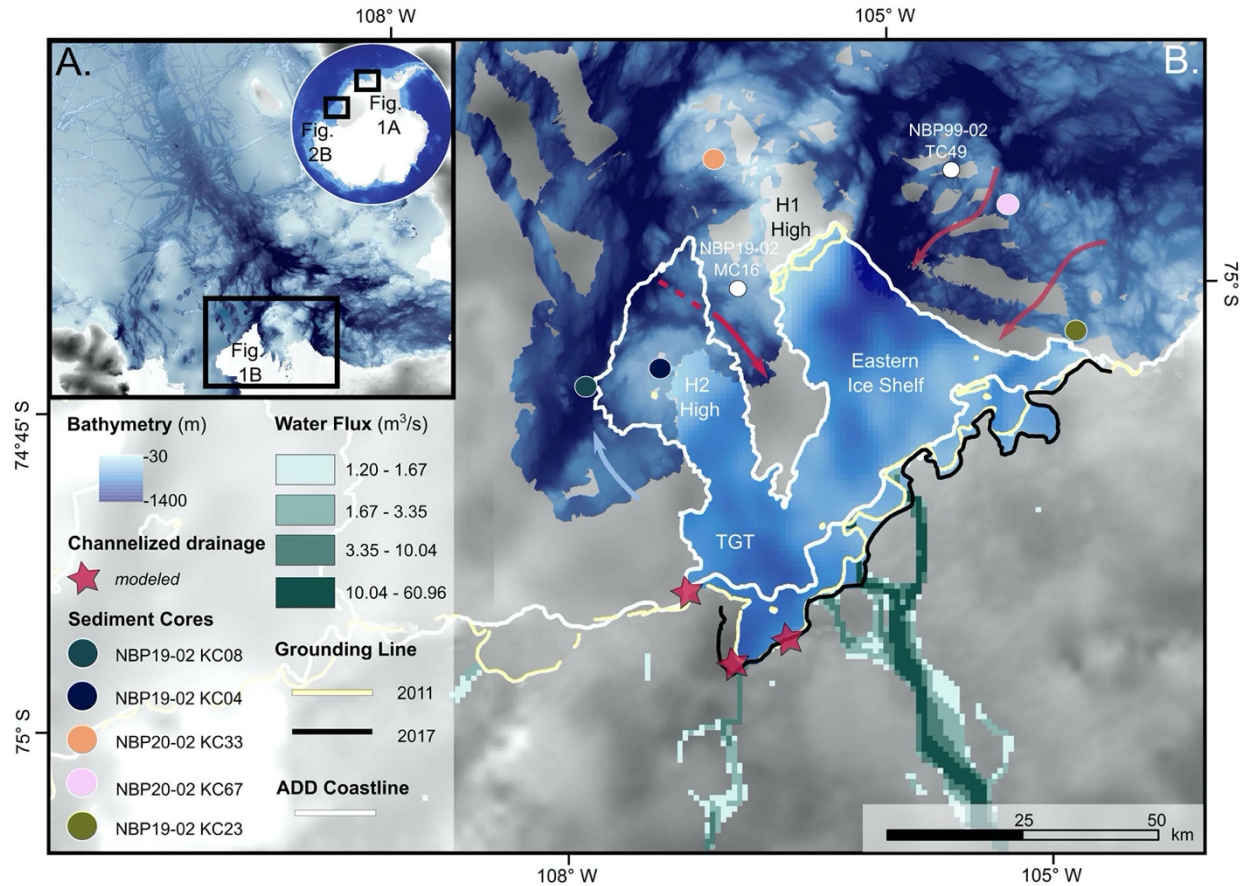


**Figure 2.1.** Regional map and locations of sediment cores used in this study. Bathymetry of the eastern Amundsen Sea Embayment (**A**) and in the vicinity of Thwaites Glacier (**B**). Data in Figure 1B were primarily collected on cruises NBP19-02 (Hogan et al., 2020a) and NBP20-02 and are gridded at 50 m. Bathymetry defining much of the eastern margin of the Eastern Ice Shelf was collected during the iStar project cruise JR294. Additional bathymetry and bed topography are from BedMachine (Morlighem et al., 2020), and sub-ice shelf bathymetry is from Jordan et al. (2020). Red and blue arrows denote inflow of warm water and outflow of meltwater-laden fresher water, respectively, from Wåhlin et al. (2021). Grounding-line data are from Rignot et al. (2011) and Milillo et al. (2019) and coastline data are from the Antarctic Digital Database. Subglacial flux is from the Quantarctica dataset and was originally published by Le Brocq et al. (2013). Stars approximate where modeled subglacial channels coincide with the Thwaites Glacier grounding zone (Hager et al., 2022).

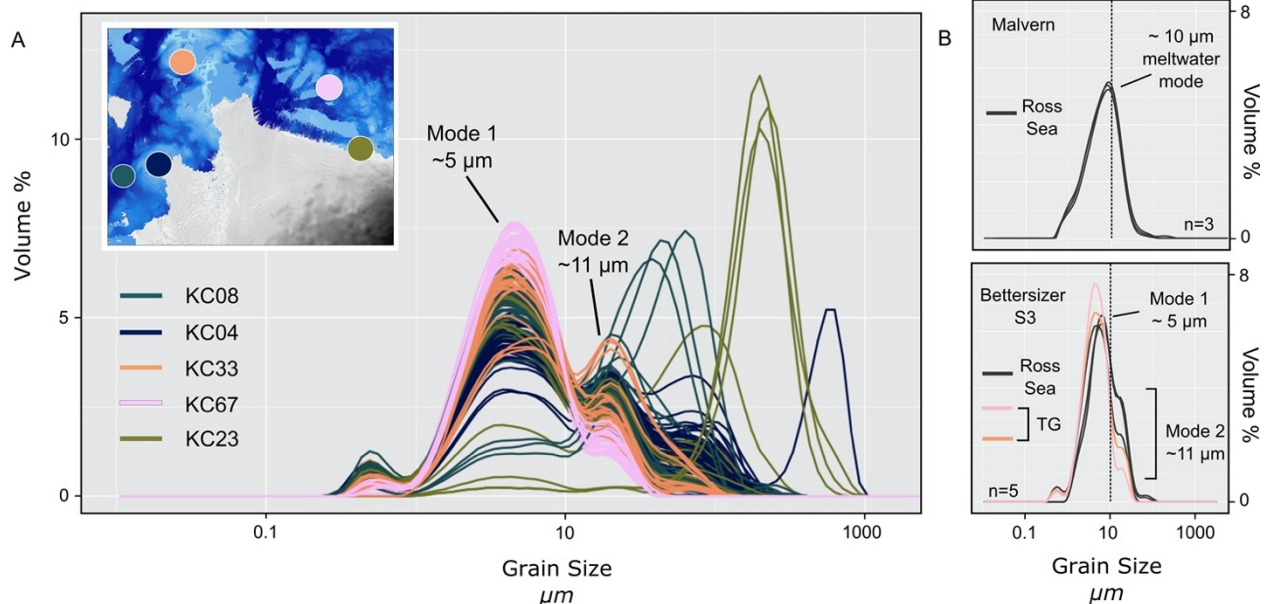


**Figure 2.2.** Grain-size distributions of sediment core samples ( $n=196$ ) on a semi-log axis plotted against volume percent. Core locations are denoted by color in the inset map in panel (A). (A) All samples exhibit varying degrees of  $\sim 5$  micron Mode 1 and  $\sim 11$  micron Mode 2, similar to meltwater deposits described elsewhere along the continental shelf in the Pacific Sector of Antarctica. (B) Instrumental comparison for grain-size distributions of previously published meltwater deposits from the western Ross Sea (see inset in Figure 2.1A) collected during cruises NBP98-01 (KC54 26 cm) and NBP1502 (KC17 170 cm; KC24 79 cm) and published in Prothro et al. (2018) and Simkins et al. (2017). In the lower panel are samples KC33 200-202 cm and KC67 50-52 cm from Thwaites Glacier (TG) shown for reference.



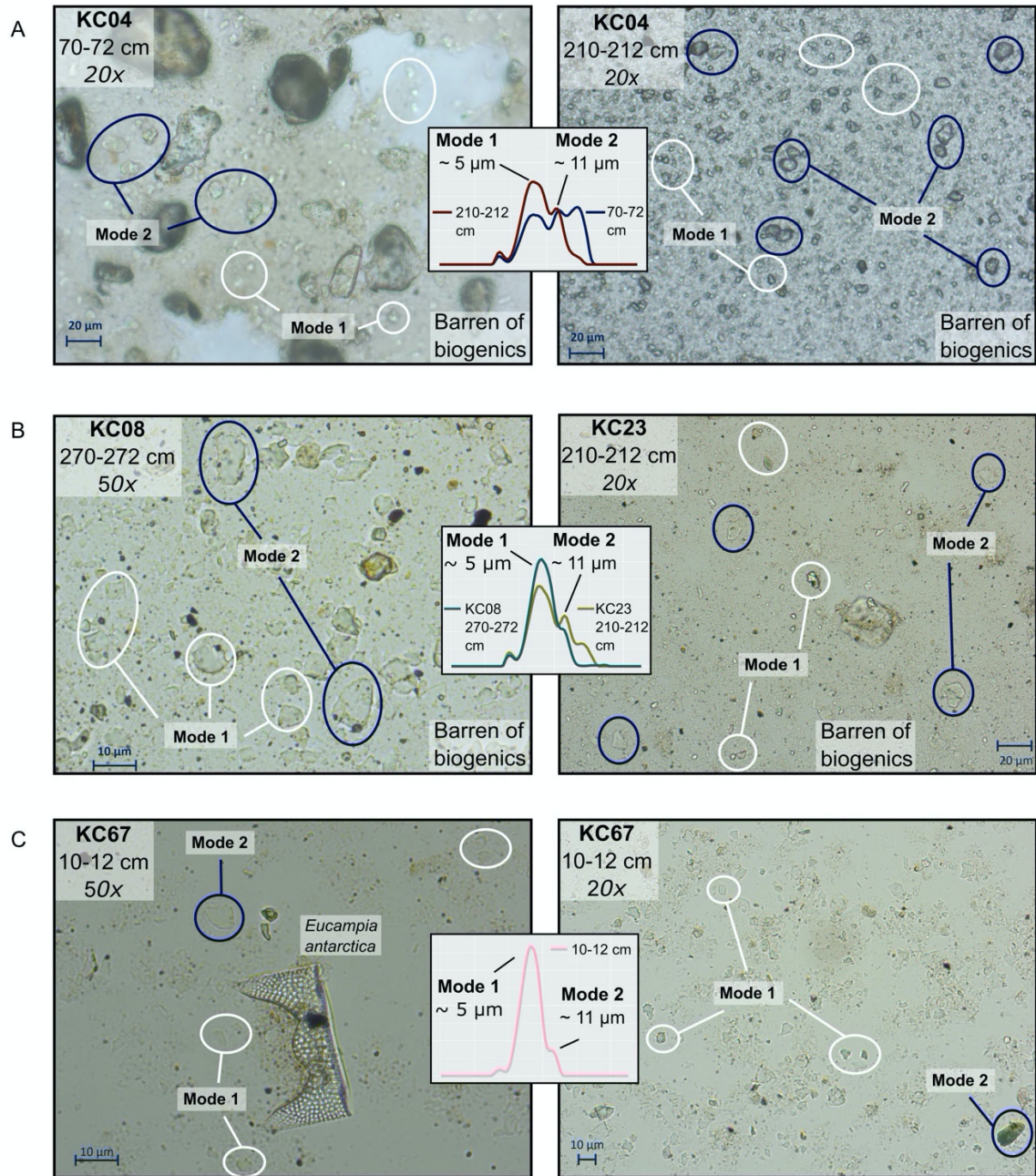


**Figure 2.3.** Smear slide images and corresponding grain-size distributions for select samples. Images were taken under plane-polarized light. Grain-size distributions shown for corresponding intervals have the same axis labels as in Figure 2.2B. Panels examine grain-size Modes 1 and 2 in intervals (A) within the same core, (B) from cores from different geographic locations, and (C) in surface sediments. (A) Core KC04 is dominated by poorly-sorted, ice-shelf proximal sediments (left) but contains discrete layers of purely terrigenous and relatively well-sorted fine silt (right). (B) KC08 (left; offshore from TGT) and KC23 (right; EIS corner). Grain size Modes 1 and 2 are caused by terrigenous grains that are present in variable amounts despite geographical difference between sites. (C) KC67 is dominated by Mode 1 grains and features sparse, complete diatom frustules.

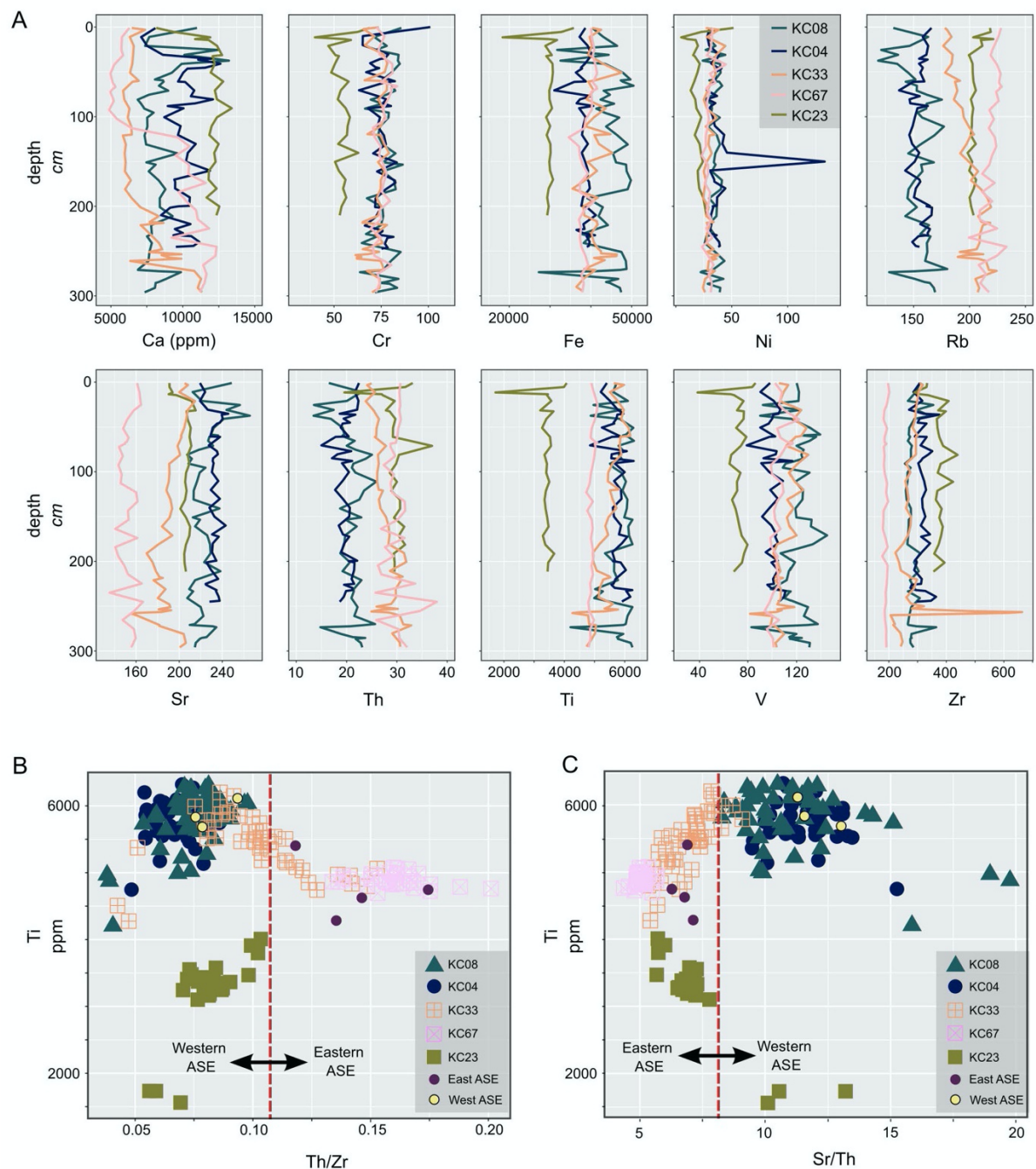


**Figure 2.4.** Sediment core geochemistry. **(A)** Downcore concentrations of selected trace elements in ppm. Core legend is given in the upper-right corner of the Ni plot. **(B-C)** Immobility trace elemental ratios Th/Zr and Sr/Th plotted against Ti. Element ratios of surface sediment samples (< 63 microns) representative for the detrital input into the eastern Amundsen Sea Embayment (ASE, sites 30-33 of Simões Pereira et al., 2018) and the western ASE (sites 34, 36, and 38 of Simões Pereira et al., 2018) in the vicinity of Thwaites Glacier are shown for reference. The vertical dashed line indicates a division between eastern and western geochemical signals.



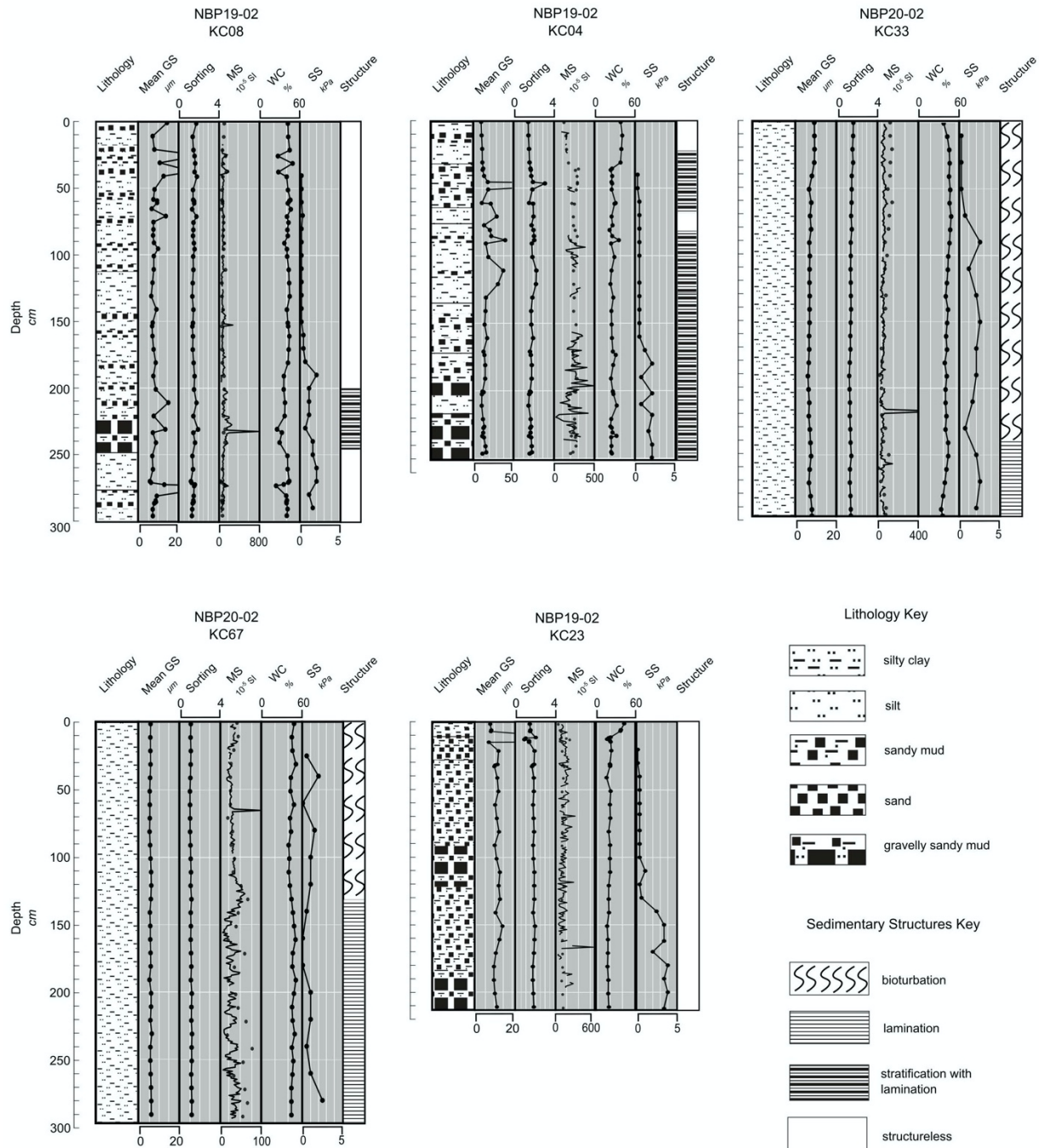


**Figure 2.5.** Downcore lithology, physical sediment properties, and sedimentary structures for each core. GS = grain size; MS = magnetic susceptibility; WC = water content; SS = shear strength. Sedimentary structures and stratigraphy are further discussed in Figure 6 with the added context from computed tomography images. Linescan MS profiles and discrete MS profiles are plotted together as a line and closed circles, respectively. Discontinuous linescan MS profiles can result from uneven core surfaces (e.g., KC04). Note the difference in scale of MS and Mean GS between cores.

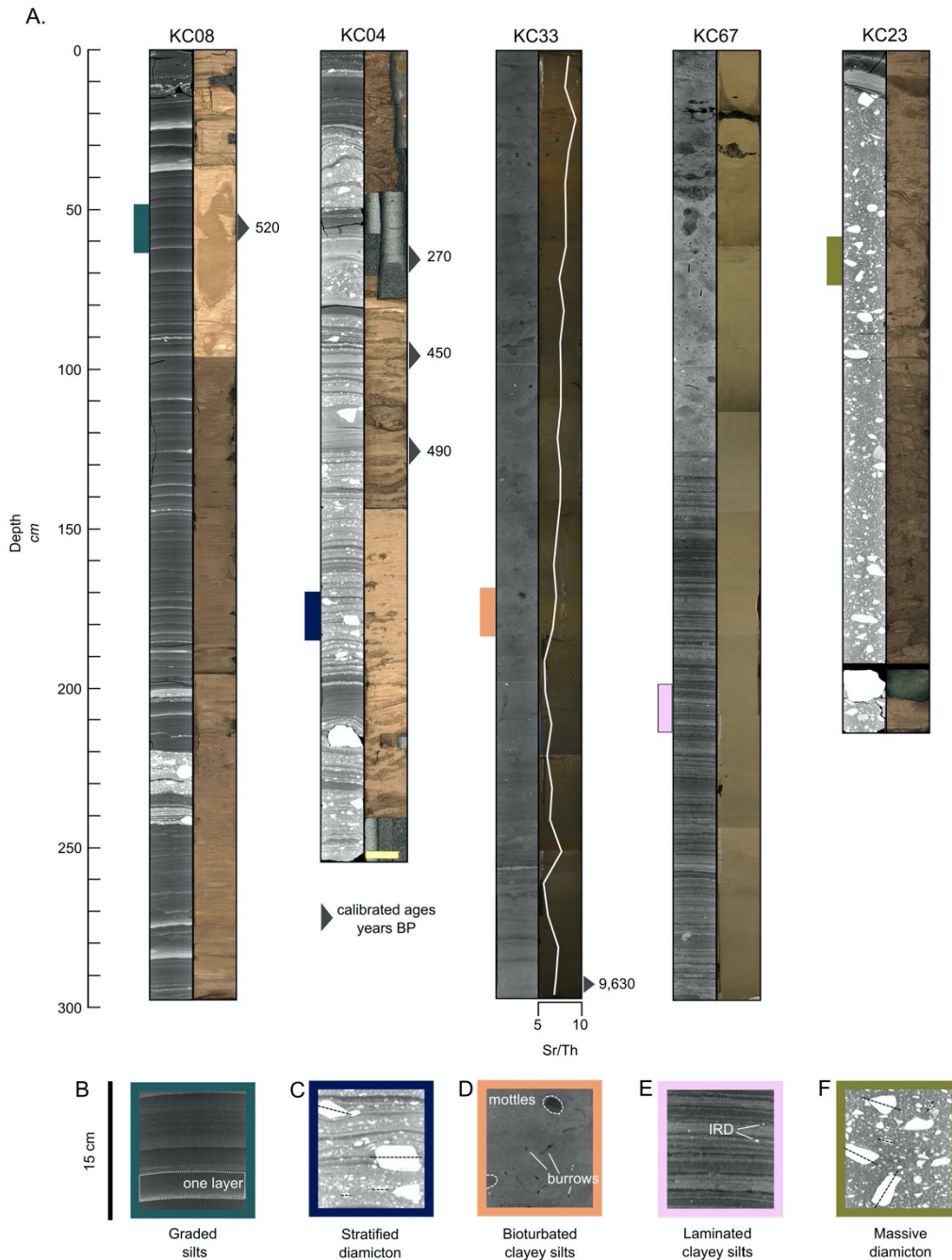


**Figure 2.6.** Greyscale computed tomography (CT) images of sediment cores collected offshore Thwaites Glacier. **(A)** CT image next to linescan photo. Downcore Sr/Th is imposed on core KC33 and reflects a gradual change in sediment source. Dates (cal yr BP) are shown alongside the corresponding interval. Refer to Table 2.2 for error bounds. Colored vertical lines denote core sections shown in **(B-F)**. **(B-F)** Sediment facies described in this study with annotations. Long-axis orientation for clasts of varying sizes is traced in diamicton facies **(C)** and **(F)**. Note that more than one sediment facies is observed within each core.



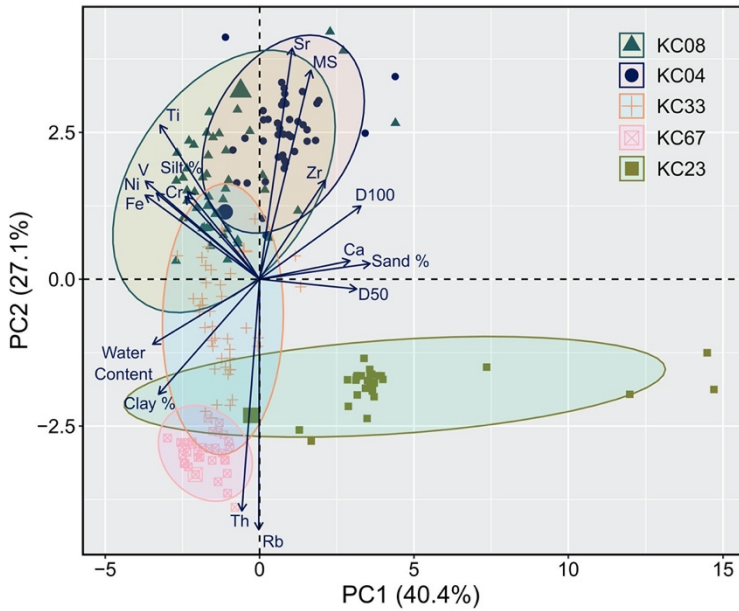


**Figure 2.7.** Biplot projecting results of PCA. Variance in principal component (PC) 1 is largely controlled by grain-size parameters and water content while PC2 variance is influenced by trace element concentrations. The surface sample (0-2 cm) for each core is indicated by an enlarged symbol, and concentration ellipses are drawn to include the 95<sup>th</sup> percentile.

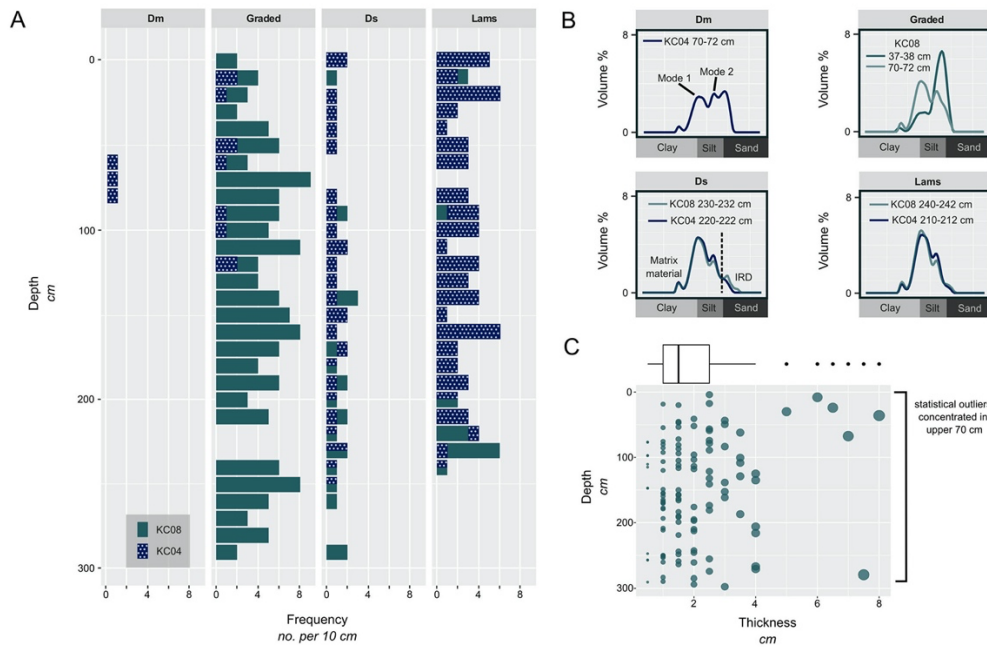


**Figure 2.8.** Frequency analysis of sediment layers observed in cores offshore the TGT. **(A)** Downcore frequency of sediment facies categorized as massive diamicton (Dm), graded silt layers and stratified diamicton (Ds), in addition to laminations and beds within facies Ds (lams). **(B)** Representative grain-size distributions for each sediment facies. Note that ice-rafted debris in Ds includes only the sand fraction and not coarser clasts. **(C)** Thickness of graded layers throughout core KC08. Boxplot denotes 75% of all graded layers are  $\geq 2.5$  cm. While thick (i.e.,  $\geq 5$  cm) graded layers are concentrated in the upper 70 cm of the core, a comparable layer is observed at ~280 cm depth.

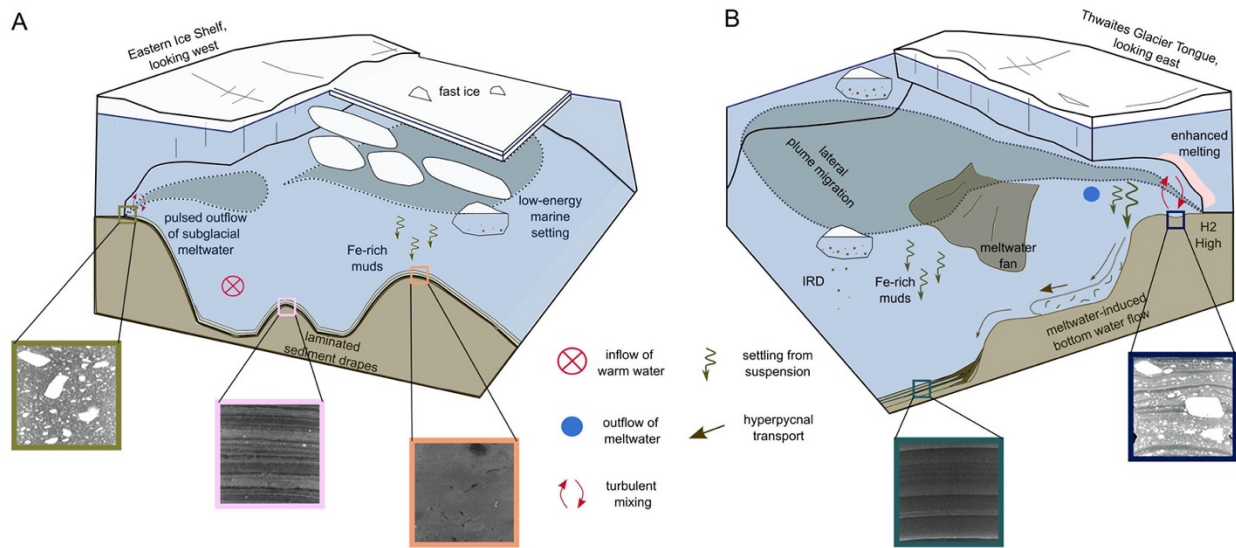


**Figure 2.9.** Cartoon of contrasting meltwater drainage styles inferred offshore from the EIS and TGT. Callouts show general depositional settings, not exact locations, of sediment facies presented in Figure 6. Grounding-line positions are not exact. **(A)** Persistent, low-magnitude drainage emanating from beneath eastern Thwaites Glacier. Settling from suspension dominates here, likely beneath a perennial canopy of floating ice. **(B)** Downslope gravitational transport sourced from sediment-laden meltwater plume deposits. Hyperpycnal flow delivers coarse silts and occasionally fine sands to trough, where fine silts and clays settle from suspension.

## Chapter 3: Insights into glacial processes from micromorphology of silt-sized sediment

*Adapted from: Lepp, A.P., Miller, L.E., Anderson, J.B., O'Regan, M., Winsborrow, M.C.M., Smith, J.A., Hillenbrand, C.-D., Wellner, J.S., Prothro, L.O., and Podolskiy, E.A., The Cryosphere, <https://tc.copernicus.org/preprints/tc-2023-70> (preprint).<sup>3</sup>*

### 3.1 Introduction

The distribution and transmission of water beneath ice sheets influences subglacial sediment deformation (Alley et al., 1986; Boulton et al., 2001; Iverson, 2010) and, subsequently, ice-flow dynamics (e.g., Stearns et al., 2008; Gustafson et al., 2022; Livingstone et al., 2022 and references therein). As quantities of ice sheet surface melt production and drainage to the ice sheet bed are modeled to increase in coming decades (Trusel et al., 2015; Lenaerts et al., 2016; Flowers, 2018; Gilbert and Kittel, 2021), continued efforts towards a nuanced understanding of subglacial hydrology at all scales is needed. Marine sediment cores collected from deglaciated continental shelves record discrete meltwater drainage events and persistence of subglacial drainage pathways with temporal resolutions of centuries to millennia (Witus et al., 2014; Prothro et al., 2018; O'Regan et al., 2021; Jennings et al., 2022; Lepp et al., 2022). Numerous marine sediment cores collected offshore of extant continental ice sheets have recovered distinctive meltwater plume deposits (MPDs) that, upon integration into glaciomarine facies models and bathymetric observations, have revealed connections between subglacial hydrologic activity and ice-marginal behavior prior to and during glacial retreat (Simkins et al., 2017; Prothro et al., 2018; O'Regan et al., 2021). However, very little work has been done to infer pertinent details of paleo-subglacial hydrology, such as evolution of drainage pathways or sediment mobilization within subglacial meltwater flow, using subglacially-sourced MPDs.

Research characterizing MPDs has largely relied on grain size (Witus et al., 2014; Simkins et al., 2017; Prothro et al., 2018, 2020), magnetic susceptibility (Witus et al., 2014; Smith et al., 2017), stratigraphy (O'Regan et al., 2021; Lepp et al., 2022; Lešić et al., 2022; Jennings et al., 2022; Clark et al., 2023), and water content (Streuff et al., 2017; Lepp et al., 2022; Clark et al., 2023). In acoustic data, sediments comprising MPDs appear stratified and drape the seafloor topography (Witus et al., 2014; Hogan et al., 2020b; Jennings et al., 2022; Lepp et al., 2022; Roseby et al., 2022) reflective of suspension settling, and may infill bathymetric lows or basins (e.g., Nitsche et al., 2013; Witus et al., 2014; Roseby et al., 2022). In sediment cores, MPDs are often laminated or thinly bedded, where subtle variation in grain size between laminae may be indicative of varying plume dynamics, magnitude, or proximity of the ice margin (Ó Cofaigh and Dowdeswell, 2001; O'Regan et al., 2021; Jennings et al., 2022; Lepp

---

<sup>3</sup> APL: conceptualization, data curation, formal analysis, investigation, methodology, project administration, software, visualization, writing – original draft. LEM: conceptualization, funding acquisition, methodology, project administration, resources, supervision, writing – review & editing. JBA: conceptualization, funding acquisition, writing – review & editing. MO, MCMW: conceptualization, resources, writing – review & editing. JAS: funding acquisition, resources, writing – review & editing. CDH, JSW: funding acquisition, writing – review & editing. LOP, EAP: resources, writing – review & editing.

et al., 2022; Roseby et al., 2022). Shared grain size modes (Simkins et al., 2017; Prothro et al., 2018), and more recently geochemical similarities (Lepp et al., 2022), between tills, ice-proximal deposits, and MPDs from the same region reflect a common subglacial origin. Furthermore, the grain-size distributions of MPDs collected offshore several Antarctic glacial systems are strikingly similar despite regional variations in subglacial geology (Halberstadt et al., 2016; Simkins et al., 2017; Prothro et al., 2018; Lepp et al., 2022), suggesting the glacial and/or glaciofluvial processes that produce these distinctive sedimentary deposits operate on an ice-sheet scale. The aforementioned processes, however, are poorly understood and hypothesized mechanisms for subglacial mobilization and sorting of MPDs observed offshore (e.g., Schroeder et al., 2019) have not been empirically evaluated.

Grain shape is considered to be a cumulative function of bedrock geology, effects of weathering on preexisting sediments, and sediment transport mechanisms (Mahaney, 2002) and is a powerful proxy for inferring sediment transport history and depositional setting (e.g., Oakey et al., 2005; Campaña et al., 2016; van Hateren et al., 2020), but has been underused in studies that characterize glacial deposits. Of those sparse works, many employ Fourier grain-shape analysis to identify harmonic ranges describing grain elongation, roughness, and transport history (Wellner et al., 2011; Livsey et al., 2013; Witus et al., 2014; Charpentier et al., 2017; Robinson et al., 2021; Clark et al., 2023). In Pine Island Bay, West Antarctica, a comparison of grains from tills and meltwater deposits showed differences in elongation but little variation in grain roughness (Witus et al., 2014), providing support for the use of grain shape in glaciomarine environments as an indicator of subglacial sediment transport. Complementary to grain shape, grain microtextures have been more widely examined on glaciogenic grains (Mahaney, 2002; Vos et al., 2014). Suites of microtexture assemblages are associated with different geneses, and have been useful in distinguishing sources of ice-rafted debris (Immonen, 2013; St. John et al., 2015; Passchier et al., 2021), inferring relative ice volume on glacial-interglacial timescales (Cowan et al., 2008), and evaluating distance of proglacial transport (Sweet and Brannan, 2016; Křížek et al., 2017). A micromorphologic (i.e., grain shape and microtexture) approach to examine MPDs and the tills from which they are sourced thus has the potential to reveal process-based details of hydraulic transport and grain-size production in subglacial environments.

This study combines a quantitative and qualitative approach to characterize grain micromorphology (encompassing grain shape and microtexture) of MPDs and tills, or ice-proximal diamictos, from six glaciated and formerly glaciated settings in both hemispheres: Ryder Glacier, Thor Iversenbanken, Marguerite Trough, Pine Island Glacier, Thwaites Glacier, and the Ross Sea (Figure 3.1). We aim to determine whether MPDs have diagnostic grain-shape distributions and microtexture assemblages and to explore how grain-shape alteration of MPDs from their source materials may record details of subglacial sediment transport and subglacial plumbing through time.

### *3.1.1 Bathymetric and glaciological settings of study sites*

Ryder Glacier drains from the northwestern Greenland Ice Sheet into the Lincoln Sea through the Sherard Osborn Fjord (O'Regan et al., 2021). Cores sampled for this study were recovered from an along-fjord transect at sites ranging in water depths from 238 m to 633 m (Table 3.1). Cores from the shallowest water depths (RYDER19-8PC and RYDER19-9PC) were collected atop a prominent bathymetric sill lying close to the modern ice tongue calving line (O'Regan et al., 2021). Glaciomarine sediments derive from both clastic and carbonate sedimentary sources (Henriksen et al., 2009; O'Regan et al., 2021). Early Holocene retreat of Ryder Glacier from the fjord mouth, as well as late Holocene retreat following a glacial readvance, coincide with periods of relatively warm Arctic air temperatures (Lecavalier et al., 2017; O'Regan et al., 2021).

Cores from Thor Iversenbanken in the central Barents Sea were collected from a bathymetric region featuring interconnected basins and channels (Esteves et al., 2022) approximately 15 km from the flow path of the Sentralbankrenna paleo-ice stream (Bjarnadóttir et al., 2014, Esteves et al., 2017). This basin-channel system is interpreted as a series of paleo-subglacial lake basins located beneath non-streaming ice (Esteves et al., 2022), and sedimentological analyses of cores from this region provide evidence for active subglacial drainage between basins (Esteves et al., 2022). The cores included in our study, CAGE-15-5-1221 and CAGE-15-5-1222, were recovered from an adjacent bank area and from within the lower-most basin, respectively (Esteves et al., 2022). Deglaciation of the central Barents Sea is constrained to the late Pleistocene (e.g., Winsborrow et al., 2010) and supraglacial input to the subglacial hydrological system is inferred from the deglacial landform record (Shackleton et al., 2023). The relict Barents Sea Ice Sheet is heralded as a good analog for the West Antarctic Ice Sheet, due in part to similarities in size and sedimentary subglacial geology (Andreassen and Winsborrow, 2009).

The relict Marguerite Trough Ice Stream drained the Antarctic Peninsula Ice Sheet, extending nearly 400 km from the modern coastline to the continental shelf break during the Last Glacial Maximum (LGM; Ó Cofaigh et al., 2014). Geomorphic evidence of ice streaming and a network of channels and remarkably deep (900 m) basins is preserved on the deglaciated continental shelf (Ó Cofaigh et al., 2005; Anderson and Fretwell, 2008; Livingstone et al., 2013). Cores in this study were recovered from within moderately deep basins (Table 3.1) to the west of George VI Trough (Kennedy and Anderson, 1989). The tills sampled for this study are composed primarily of metamorphic rock fragments and quartz, while the MPDs are rich in silt-sized quartz and feldspar grains (Kennedy and Anderson, 1989). While sediment cores recovered from Marguerite Bay often contain thick units of diatomaceous and organic-rich sediments, the MPD samples in this study were taken from units where siliceous microfossils and organic materials were virtually absent (Kennedy and Anderson, 1989). Initial retreat of the Marguerite Trough Ice Stream occurred coeval with meltwater pulse 1a approximately 14 thousand years (ka) before present (Kilfeather et al., 2011).

Thwaites and Pine Island glaciers drain into the eastern Amundsen Sea Embayment and, during the LGM, coalesced, reaching the outer continental shelf (Kirshner et al., 2012; Larter et

al., 2014 and references therein). Retreat across Pine Island Bay initiated during the late Pleistocene and continued in distinct stages until the grounding lines for Pine Island and Thwaites glaciers largely stabilized within ~100 km of their current positions by ~10 ka ago. (Hillenbrand et al., 2013; Nitsche et al., 2013; Witus et al., 2014; Lepp et al., 2022). Cores used in this study (Table 3.1) were collected on the mid- and inner shelf from a variety of bathymetric settings, including atop an ice-proximal bathymetric high and on a ridge beneath the Pine Island Ice Shelf (Smith et al., 2017). Volcanic and plutonic rocks, largely felsic in composition, underlie the Pine Island and Thwaites glaciers (Smith et al., 2013; Schroeder et al., 2014; Simões Pereira et al., 2020), and large sedimentary basins upstream have been identified by aeromagnetic surveys (e.g., Muto et al., 2016) and inferred by observations of kaolinite-rich sediments offshore (Hillenbrand et al., 2003; Ehrmann et al., 2011; Simões Pereira et al., 2020). Geothermal heat flux is elevated in the region (Damiani et al., 2014; Schroeder et al., 2014; Dziadek et al., 2021).

Cores collected from the western Ross Sea were recovered from bank tops (NBP1502 KC22; Halberstadt et al., 2018) and from topsets and toes of grounding-zone wedges (NBP1502 KC17, KC19; Prothro et al., 2018) in water depths ranging from 354-549 m (Table 3.1). At the LGM, the East Antarctic Ice Sheet occupied the western Ross Sea (e.g., Anderson et al., 2014), however, unlike other glacial systems described, landforms on the seafloor indicate that grounded ice did not extend to the continental shelf margin (Greenwood et al., 2012; Halberstadt et al., 2016). High geothermal heat flux is inferred in the western Ross Sea (Simkins et al., 2017) based on the proximity of core sites to volcanic seamounts (Rilling et al., 2009), a rifting zone (Cooper et al., 1987), and measurements (Blackman et al., 1987 and references therein). Tills from this region are composed largely of felsic lithic fragments (Licht et al., 2005).

### **3.2 Materials and Methods**

A total of 49 sediment samples from MPDs, tills, and ice-proximal glaciomarine diamictons from the regions described in Section 3.1.1 were gathered for grain-shape analysis (Figure 3.1; Table 3.1). For glacial systems from which subglacial till was not available (e.g., Thwaites Glacier), MPD grains were compared directly to ice-proximal diamicton grains. Other systems from which both subglacial till and ice-proximal diamicton were available (e.g., Pine Island Glacier) compared MPD grains against all diamicton grains, merging grains from both subglacial and ice-proximal deposits. While subglacial till and ice-proximal diamicton differ in their depositional environments and processes, the sediment transport processes responsible for grain-shape alteration are largely the same and are distinctly different from sediment transport via subglacial meltwater; therefore, incorporating materials from both subglacial till and ice-proximal diamicton in comparison against MPDs is appropriate to address the goals of this study.

In addition, sediments from basal ice recovered from Siple Dome in the Ross Sea drainage sector of West Antarctica, fringe debris (i.e., sediment entrained into basal ice through infiltration of ice into sediment pore spaces; Rempel, 2008; Meyer et al., 2019) from Pope

Glacier in the Amundsen Sea drainage sector of West Antarctica, and supraglacial cryoconite debris from Qaanaaq Glacier in Northwest Greenland, underwent the same suite of analyses and are used to contextualize the micromorphologies observed in our primary sample populations (Table 3.1).

### *3.2.1 Grain-shape analysis*

Bulk sediment samples were treated with sodium metaphosphate to deflocculate clays for 48 hours prior to analysis. Tills, ice-proximal diamictons, and basal ice debris were sieved at 500 microns ( $\mu\text{m}$ ) to isolate matrix material. To remove organics from cryoconite, samples were placed in a hot water bath at 100 °C and 15%  $\text{H}_2\text{O}_2$  was added in 1 mL increments until at least two hours elapsed with no observable reaction. While it is possible for glaciomarine sediments containing organics to be reworked in till and ice-proximal diamicton and for organics to occur within MPDs, prior studies of the samples used here report organics are either barren or occur in trace amounts in sediments (e.g., Kennedy and Anderson, 1989; Prothro et al., 2018; O'Regan et al., 2021; Lepp et al., 2022; Clark et al., 2023). Therefore,  $\text{H}_2\text{O}_2$  treatment was not applied to all core samples. Aliquots of sediment from a homogenized slurry were introduced into a Bettersizer S3 Plus sampling reservoir where grain size was measured through laser diffraction. Thousands of images of grains from the same aliquot were subsequently captured using the integrated microscope charge-coupled device camera. Images captured with the 10x objective were exported for shape analysis because this magnification preferentially captures finer grain sizes, including the silt-sized range prevalent in MPDs, than the 0.5x objective. The lower detection limit for the 10x objective is 0.8  $\mu\text{m}$ ; to avoid sampling bias skewed towards that threshold or towards clay minerals, images of grains finer than 2.4  $\mu\text{m}$  were excluded from analysis (Crompton et al., 2019).

A MATLAB script for grain-shape analysis (doi to PANGAEA dataset pending) randomly selected 200 unique images from each sample, processed images to distinguish foreground from background, converted images from grayscale to binary, and calculated three dimensionless metrics on the binarized shapes using the “regionprops” function (Figure 3.2). The metrics considered include eccentricity, circularity, and solidity, and collectively provide information about grain form (i.e., roundness) and shape (regularity). Evaluating distinct shape metrics, rather than harmonic ranges or grain roughness as employed by studies referenced above, allows us to consider the magnitude of variability for each parameter within the context of the other measurements. To test the null hypothesis that grain shapes found in meltwater deposits and subglacial/ice-proximal diamictons from the same glacial systems are indistinguishable, we performed a two-type Z-test on the means of each group for each shape metric considered (probability  $p < 0.05$ ). We calculate 95 % confidence intervals from 1,000 bootstrap replicates for those samples and metrics showing statistically significant differences in means.

### *3.2.2 Microtexture analysis*

Based on the quantitative grain shape output, a subset of samples was imaged by a scanning electron microscope (SEM) for microtexture analysis. An aliquot of the deflocculated sample was pipetted from a homogenized slurry and dispensed onto a 63  $\mu\text{m}$  sieve, where a fraction that passed through was collected onto a piece of weigh paper. Once dried, a section of the weigh paper was mounted, sputter coated (Au-Pd), and imaged using an FEI Quanta 650 field-emission gun in high vacuum mode. We followed the traditional approach to microtexture analysis, targeting quartz grains as they are widespread across depositional environments and highly resistant to weathering (Vos et al., 2014). Grain composition was verified as quartz through the Oxford AZtec energy dispersive x-ray spectrometer (EDS) program prior to imaging.

Grains were categorized by relief (high to low, following Mahaney, 2002) and roundness (angular to rounded, after Vos et al., 2014). Presence or absence of a suite of microtextures associated with glacial transport (cf. Passchier et al., 2021) and fluvial environments (cf. Vos et al., 2014; Křížek et al., 2017) were identified and calculated in frequency of occurrence (%) for each sample (Figure 3.3). Percent overrepresentation is calculated as the difference between mean frequencies of occurrence by sample type for each texture. Microtexture identification primarily followed Mahaney (2002), yet because this canonical reference focuses on the sand fraction, textures on some grains were counted based on appearance rather than the specified scale. For example, Mahaney (2002) specifies arcuate and straight steps occur on the  $>5 \mu\text{m}$  scale, while we observed this feature on finer scales (Figure 3.3).

### 3.3 Results

#### 3.3.1 Grain-shape distribution of meltwater plume deposits and tills

Of the metrics considered, eccentricity shows the greatest statistical variance between glacial systems, with standard deviations of 3.4 % and 4 % between medians of all MPD and till or ice-proximal diamicton samples, respectively. Grains from the Marguerite Trough Ice Stream encompass the widest spread of eccentricities for all regions considered, with an average interquartile range of 0.25. Thor Iversenbanken and Marguerite Trough samples contain grains that are generally more eccentric relative to the other four systems. Of those other four systems, Ryder Glacier, Thwaites Glacier, Pine Island Glacier, and Ross Sea, distributions of grain eccentricity are strikingly similar with interquartile ranges from 0.38 to 0.66 for both grain populations (Figure 3.4), though the median eccentricity for Thwaites Glacier grains is slightly elevated at 0.53. Marguerite Trough Ice Stream is the only system where eccentricities of MPD and till grains are highly significantly different, reflecting MPD grains that are notably less elongate compared to their source material. Eccentricity of MPD and till grains from Pine Island Glacier were determined to be significantly different, again with MPD grains being less elongate (Table 3.2).



On average, the most circular grains are found in Ross Sea MPDs (mean: 0.63, median: 0.64) while the least circular grains are found in tills from the Thor Iversenbanken (mean: 0.55, median: 0.56). The median circularity of MPD grains is higher compared to tills for all six systems, but differences in means are statistically significant only for Ryder Glacier, Pine Island Glacier, and Ross Sea samples (Figure 3.4). Interestingly, interquartile ranges for MPDs from Marguerite Trough Ice Stream and Thwaites Glacier do not show enhanced circularity relative to source material. Instead, compared to their respective source populations, these MPDs appear to have restricted subsets of circularities with similar medians as their corresponding till samples. An intercomparison of MPDs from all systems, with the addition of plume deposits from three systems with no till counterparts, reveals modest variability between interquartile range for all MPDs (0.51-0.69) with no clear regional trend (Figure 3.5). MPDs from Marguerite Trough are less circular than other Antarctic deposits and have interquartile ranges very similar to those samples from the Barents Sea (Thor Iversenbanken and Kveithola) and the Nares Ice Stream. Ryder Glacier and Petermann Ice Stream MPDs have the widest interquartile ranges with median values similar to samples from PIG and the Ross Sea, respectively. Some regional differences in circularity, like in NW Greenland where glaciers have similar catchment areas and meltwater sources (Figure 3.1, 3.5), likely reflect varied mineralogy: Petermann Glacier detritus is higher in calcite and dolomite (Jennings et al., 2022), Nares Ice Stream detritus in quartz and micas (Jennings et al., 2022), while Ryder Glacier detritus consists of both carbonate and clastic sedimentary materials (O'Regan et al., 2021) and shows an interquartile range of grain circularity between the other two. Yet, NW Greenland MPDs have similar distributions of grain circularity to West Antarctica MPDs (Figure 3.5) and Ryder Glacier tills are more irregular than West Antarctic tills (Figure 3.4), alluding to impacts on MPD grain shape unrelated to source geology. We also note that the circularity distributions for MPDs from all systems overlap with one another and are largely confined between values of 0.4 and 0.8 (Figure 3.5).

Solidity describes regularity of grain perimeters, and the interquartile ranges for Ryder Glacier, Thor Iversenbanken, Pine Island Glacier, and the Ross Sea demonstrate shifts to enhanced grain regularity from tills to MPDs, with highly statistically significant differences for all but the Thor Iversenbanken (Figure 3.4). As with circularity, MPD grains from Marguerite Trough and Thwaites Glacier exhibit a narrower interquartile range of solidities than is found in corresponding till samples; the mean and median distribution for each grain population is virtually the same for these systems. The median solidity for tills from Ryder Glacier, Thor Iversenbanken, and Marguerite Trough is all 0.61, while those from Pine Island Glacier, Thwaites Glacier, and the Ross Sea are slightly higher (0.628-0.634).

We acknowledge that grain size, and therefore image resolution (Figure 3.2), may have some influence on the observed grain-shape distributions. However, none of the distributions for any metric considered are strongly skewed towards upper or lower limits as we would expect if image resolution were controlling the distribution of shape values. These results suggest that the preventative measures integrated into the methodology (removing grains below 2.4  $\mu\text{m}$ ; random

selection of grains to use in analysis) sufficiently removed any grain-size bias from the quantitative grain-shape results.

### 3.3.2 *Microtexture observations*

A total of 132 grains were imaged from four MPDs (n grains = 63) and four tills/ice-proximal diamicton (n grains = 69; Table 3.1). Imaging was attempted on approximately twice that number of samples, however the fine-grained and electrostatic nature of MPDs presented challenges in isolating quartz grains in the silt fraction, and many samples imaged were dominated by clays and had fewer than 10 quartz grains. The eight samples included in microtexture observations imaged between 12 and 20 quartz grains, which is within the range considered to be representative for any given SEM sample (cf. Vos et al., 2014).

We observe suites of microtextures characteristic of glacial transport on quartz grains at the micron to sub-micron scale (e.g., Figure 3.3d) in both till and MPD populations, indicating microtexture analysis on glaciogenic silts is both feasible and results in meaningful data. Angular grains and grains with high relief are found to be overrepresented in till samples compared to MPDs by 31 % and 10 %, respectively (Figure 3.6). Conversely, grains with subangular and subrounded shape, as well as low relief grains, occur in higher abundance in MPDs (Figure 3.6). Round grains are comparably rare in till and MPD samples, and grains with medium relief are the most abundant relief type in both sample populations (Figure 3.6). All step and fracture textures that are attributed to high stress, grinding, plucking, and abrasion in glacial environments (Vos et al., 2014; Passchier et al., 2021) are overrepresented in till grains, ranging from 3 % (sawtooth fractures) to 18 % (straight steps) more common than in MPDs (Figure 3.6). Additionally, breakage features including blocks, concavities, and plates are observed in moderate ( $\leq 50$  %) abundance in both grain types and are largely overrepresented in tills.

Fluvial microtextures imparted to grain surfaces through intergranular collisions during transport in suspension are observed on both till and MPD grains, but with abundances  $\leq 25$  % are not pervasive features (Figure 3.6). V-shaped percussion cracks and impact pits are overrepresented in MPD grains by only 5 % and 2 %, respectively, while meandering ridges are, somewhat surprisingly, overrepresented in till/ice-proximal diamicton grains by 4 %. Notably, grains in MPDs exhibit edge rounding 26 % more often than is observed in till and ice-proximal diamicton samples. It is important to note that, while differences in average frequencies allow us to compare microtexture abundance between tills and MPDs, nearly all textures are observed in some abundance in both populations. In other words, overrepresentation of a suite of textures in one grain type does not reflect absence, or even low abundance, of that feature in the other grain type. Edge abrasion and linear fractures, for example, are both overrepresented in till grains, but are seen on over 50 % of grains in both populations.

## 3.4 Discussion

We find that quantifiable, significant differences in grain shape exist between MPDs and tills in some regions, as well as between MPDs from different regions, and that those differences can be both quantified using an automated imaging approach and, generally, verified qualitatively with microscopy. Here, we consider potential reasons for those variations and discuss implications for subglacial sediment transport processes, with an emphasis on subglacial hydrology.

### 3.4.1 Widespread subglacial sediment transport processes

Despite the variation in subglacial lithology, catchment size, glacial histories, and source(s) of basal meltwater for the glacial systems considered (Figure 3.1), we find that three-quarters of all grains studied can be described by approximately one-quarter of possible grain morphologies, alluding to highly efficient and ubiquitous erosive processes that likely operate on catchment-wide scales. Through these processes, grains with extreme morphometries (i.e., highly elongated/rounded, or highly irregular/regular) are either not produced in abundance or such extremes are short-lived. Variability between glacial systems likely reflects differences in regional substrate geology and mineralogy, glacial history (i.e., textural maturity of sediments), distance of transport, volume of meltwater present, or some combination of those factors (Figure 3.1). If regional geological and mineralogical variability were driving differences in grain shape distributions, it is likely that would manifest most clearly in eccentricity because this metric could capture relative proportions of equant and elongated or platy minerals (e.g., Marsaglia et al., 2013). Yet, median eccentricity for all MPD grains varies by only ~8 % between systems (Figure 3.4), suggesting geological differences do not fully explain all variation in the dataset. Additionally, no distinctive grain-shape populations emerge that separate (predominately) hard bed from soft bed systems (Figure 3.1), further implying that source material alone does not explain the minor intrasystem variance.

When we consider the shape distributions for supraglacial debris, basal ice debris, and basal fringe debris in relation to tills and MPDs from those regions, the erosive power of subglacial sediment transport becomes abundantly clear (Figure 3.7). Circularity of cryoconite grains from Qaanaaq Glacier, NW Greenland, and basal ice debris from Siple Dome, West Antarctica, is highly significantly different ( $Z \gg 3.0$ ) from grain circularity of tills recovered from nearby glacial systems. These references reflect materials completely or relatively unaltered through subglacial transport, both at the ice surface and beneath an ice dome where ice advection and subglacial sediment transport is expected to be minimized compared to basal ice debris from beneath ice streams or at ice margins (e.g., Knight et al., 2002; Christoffersen et al., 2010).

Less pronounced alteration is observed between grains from “dirty ice” of Kay Peak, Pope Glacier and those tills and ice-proximal diamictons in the eastern Amundsen Sea (Thwaites and Pine Island glaciers; Figure 3.7c, d). Sediment entrainment, transport, and release from the

ice fringe depends on the thermal and pressure conditions of basal ice (Rempel, 2008; Iverson et al., 2017) and is, therefore, spatiotemporally transient in nature. It logically follows that differences in grain circularity are more pronounced between till and basal ice debris or cryoconite grains than between till and fringe debris, because the latter has likely undergone transport processes at the ice-bed interface prior to fringe entrainment. Within our suite of samples from the Ross Sea, a clear grain-shape continuum emerges from basal ice debris, ice-proximal diamicton, subglacial till, and MPDs where interquartile ranges incrementally shift towards higher abundance of circular grains (Figure 3.7e). The intermediate grain characteristics implied within glacial-marine diamicton samples likely reflect inclusion of till pellets (Domack et al., 1999; Cowan et al., 2012; Prothro et al., 2018; Robinson et al., 2021) from basal ice into ice-marginal or gravity flow deposits. The differences we see between MPDs and till sources are more subtle than those between tills and basal ice debris, with the exception of Ryder Glacier (discussed in more detail in the next section).

The added context gleaned from grain micromorphology of supraglacial and basal ice debris indicates that all MPD, till, and diamicton grains in this study experienced alteration through subglacial sediment transport processes, like grain rotation and grinding, that occur predominantly in dilatant, deforming tills (Evans et al., 2006; Robinson et al., 2021). Such tills are associated with high basal water pressures and streaming of glacial ice (e.g., Boulton et al., 2001; Evans et al., 2005; Reinardy et al., 2011; Rütther et al., 2012). Thus, this finding suggests most grains experienced some degree of transport and alteration beneath fast-flowing ice, i.e. conditions that were also inferred from other paleo-subglacial records, such as subglacial bedforms and till properties, in the studied regions (Nitsche et al., 2013; Esteves et al., 2017; Jakobsson et al., 2018; Munoz and Wellner, 2018; Simkins et al., 2018; Kirkham et al., 2019, 2020; Hogan et al., 2022). No geomorphic evidence of ice streaming exists on Thor Iversenbanken (Esteves et al., 2022), however, and sediment grains from this area may have experienced morphological alteration through shearing or brittle deformation (e.g., Evans et al., 2006) that produced a slightly more irregular, elongate shape signature (Figure 3.4).

The general homogeneity in grain morphology we observe may reflect the lasting impact of grain cushioning, whereby fines fill interstitial spaces between larger till clasts and, through grain rolling, act to absorb and dissipate tensile stresses along grain bridges (Iverson et al., 1996; Menzies, 2012; Robinson et al., 2021). This effect has been shown to produce a self-similar grain-size distribution (Iverson et al., 1996), and it is possible the same may be true for grain shape. While the volume of subglacial meltwater influences how grains through a till column will be mobilized and therefore indirectly affects grain-shape alteration through the processes discussed above, our data suggest subglacial sediment transport is chiefly responsible for producing the largely homogenized grain shape distributions we observe. We acknowledge, of course, the Sisyphean challenges associated with untangling inherited grain shape from earlier glacial cycles or interglacial subaerial sediment transport (Evans et al., 2006), but do not think our inability to do so detracts from the findings of near grain-shape homogeneity in tills and MPD silts from a geographically-diverse sample population.

### 3.4.2 Production of meltwater silts

Subglacial processes responsible for generating glacial silts and the “terminal grain-size mode”, or the smallest size to which a grain can be comminuted based on its mineralogical structure, have been explored through field observations and controlled experiments (e.g., Dreimanis and Vagners, 1971, 1972; Iverson et al., 1996; Crompton et al., 2019). Those works have largely converged on abrasion as a widespread, dominant process in subglacial environments (Alley et al., 2019) that drives comminution by exploiting weaknesses in the mineral fabric of larger grains (Haldorsen, 1981; Crompton et al., 2019), and the microtextural signatures of abrasion on grain surfaces include different step and fracture types (e.g., Mahaney, 2002; Passchier et al., 2021). Furthermore, abrasion beneath glacial ice has been credited with rounding grain shape (Hart, 2006; Rose and Hart, 2008), which is consistent with the degrees of solidity and circularity in our results, particularly for those most mature (i.e., undergone reworking by multiple glacial advance and retreat cycles) sediments from West Antarctica (Figures. 3.4, 3.5).

We observe microtextures resulting from abrasive processes, including conchoidal fractures, arcuate and straight steps, parallel and sub-parallel fractures, on a large proportion of grains from both MPD and till samples (Figure 3.6). The abundance of fracture types, edge abrasion, and other microtextures imparted through sustained stress and grinding in addition to the low occurrence of v-shaped percussions on both grain populations strongly suggests the grain-size production of the ~10  $\mu\text{m}$  meltwater-silt mode results from abrasion and grinding at the base of glacial ice, rather than the comminution of grains during subglacial hydrologic transport (e.g., Schroeder et al., 2019). Witus et al. (2014) reached a similar conclusion after examining sand microtextures from MPDs and tills collected offshore PIG (material which we also include in this study, Table 3.1). Collectively, our results provide grain-scale evidence supporting an inferred subglacial origin for MPDs based on shared grain-size modes (Witus et al., 2014; Simkins et al., 2017; Prothro et al., 2018) and geochemical similarities (Lepp et al., 2022) with till and ice-proximal diamicton.

Although we did not include samples from each study region due to methodological challenges (e.g., insufficient number of quartz grains present on sample stub, adhering particles obscuring quartz grain surfaces), we have found meaningful results from the data subset and have conducted what we believe to be the first quartz microtextural analysis on the silt grain-size fraction. In addition to mechanical textures that offer insight into subglacial sediment transport, we also observed silt grains that retained pre-weathered surfaces and showed signs of silica dissolution. We encourage future microtextural investigations inclusive of, or focused on, the silt fraction because of the additional context those grains may hold for glacial histories, sediment transport processes, or paleoclimate reconstructions of glaciated or formerly glaciated regions.

### 3.4.3 Subglacial hydrological inferences from grain micromorphology

While we do not observe homogeneity in grain-shape distributions of MPDs as striking as is seen with grain size (e.g., Witus et al., 2014; Prothro et al., 2018; Jennings et al., 2022; Lepp et al., 2022), we do find that median circularity (Figure 3.5) and eccentricity of all MPDs in this study vary by less than 10 % and that distributions overlap with one another; however, because shape distributions also overlap with till and ice-proximal diamicton grains, we cannot describe the MPD grain-shape distributions as diagnostic. Similarly, we do not observe pervasive evidence of glaciofluvial transport in surface microtextures on MPDs (Figure 3.6). These deposits are described as comprising largely silt and clay with grain-size modes at or below the sortable silt fraction (10–63  $\mu\text{m}$ ; Witus et al., 2014; Prothro et al., 2018; Jennings et al., 2022; Lepp et al., 2022). Fine silts in coastal settings (e.g., Manning et al., 2013) and glacial environments (e.g., Greco and Jaeger, 2020) behave cohesively and will form floccules with clays, which has important implications for plume migration and dispersal of MPDs into the marine environment. Silt floccules in the same size range as MPDs are experimentally shown to be stable in both freshwater and saline conditions at current speeds up to 25  $\text{cm s}^{-1}$  (Yawar and Schieber, 2017). In non-outburst style subglacial flow, aggregated meltwater silts would have less exposed surface area onto which intergranular collisions could impart microtextures (Vos et al., 2014). This aggregate shielding effect could explain both the paucity of fluvial microtextures and retention of mechanical textures observed on MPDs, and is consistent with inferred episodic, low-magnitude drainage styles offshore eastern Thwaites Glacier (Lepp et al., 2022).

Alternatively, sluggish flow conditions and/or short transport distances may suffice to reduce grain relief and round edges but be insufficient to impart abundant fluvial microtextures (Figure 3.6). Microtexture studies on proglacial stream sediments find a positive correlation between transport distance and abundance of fluvial microtextures, but only after downstream transport distances between 3 km (Křížek et al., 2017) to at least 80 km (Sweet and Brannan, 2016) of downstream transport. For an evolving or transient subglacial drainage network through which flow is not constant or channelized, grains may be mobilized in suspension for only brief (i.e., sub-kilometer) distances before being deposited or entrained in basal ice via supercooling, where alteration through intergranular collisions is minimal (Alley et al., 1997; Creyts and Clark, 2010; Alley et al., 2019). In the absence of supraglacial input to the bed, such continuous flow over several or tens of kilometers may not be sustained. Rather, grains comprising MPDs experience short “bursts” of energy and entrainment (i.e., during subglacial lake drainage events) or mobilization within a sluggish, lower flow regime (i.e., through water films or distributed drainage) wherein fluvial microtextures are not expected (Mahaney, 2002; Sweet and Brannan, 2016). Low flow regimes and modest grain alteration in sediments from Thwaites Glacier is consistent with stratigraphic inferences from marine sediment cores collected from the Thwaites Eastern Ice Shelf (Lepp et al., 2022; Clark et al., 2023), while for other systems, like Pine Island Glacier and the eastern Ross Sea, some MPDs are interpreted to have rapidly accumulated through intensive, potentially catastrophic, subglacial drainage events (Lowe and Anderson,

2003; Kirshner et al., 2012; Witus et al., 2014; Prothro et al., 2018). MPD grains are significantly more regular and rounded than till and ice-proximal diamicton grains in these systems, which may be the result of intensive, but short-lived, drainage events not recorded in the other glacial settings.

The most significant intra-site grain-shape alteration we see is between subglacial tills and MPDs from Ryder Glacier. In some locations, MPDs deposited during early to mid-Holocene retreat of Ryder Glacier are three to over five meters thick (O'Regan et al., 2021) indicating a highly active, well-connected subglacial drainage network coeval with elevated air temperatures and enhanced surface melt production (Lecavalier et al., 2017; McFarlin et al., 2018). Such a drainage configuration and supply of meltwater to the ice bed would likely be capable of transporting water and sediments over long (i.e.,  $10^1$ - $10^2$  km) distances. We interpret grain-shape alteration for this system to result from the combination of younger, less rounded grains in the till source (Figure 3.4) and the input of supraglacial melt to the bed, as would be most common in temperate glacial conditions. While some glacial systems in West Antarctica show significant differences in grain solidity and circularity between grain populations, it is to a lesser magnitude than is observed in Ryder Glacier. We therefore infer that quantifiable alteration of grains through meltwater action can be achieved through continuous sediment entrainment over long distances (i.e., many tens of kilometers) or through high-energy outburst-style flow, where a supraglacial supply of meltwater to the bed and younger, less reworked till grains can further enhance alteration. Conversely, the combination of mature till grains with poorly-developed channel networks, sluggish flow, and/or brief sediment transport distances may minimally or negligibly alter MPD grains from till sources. Results from Ryder Glacier suggest that a grain micromorphological approach may be valuable in distinguishing MPDs that have been sourced from subglacial systems with the influence of significant supraglacial input to the subglacial environment, compared to those with no supraglacial input.

#### *3.4.4 On subglacial basins as reservoirs and subglacial lake drainage*

Both model results (e.g., Carter et al., 2011) and satellite observations (Wingham et al., 2006; Fricker et al., 2007; Bowling et al., 2019; Hoffman et al., 2020) indicate subglacial water can be stored in, and actively transmitted between, subglacial basins, demonstrating connected subglacial plumbing that mirrors basin-channel systems preserved on deglaciated continental shelves (e.g., Lowe and Anderson, 2003; Anderson and Fretwell, 2008; Kuhn et al., 2017; Simkins et al., 2017; Kirkham et al., 2019; Hogan et al., 2020b). The importance of subglacial lakes as reservoirs of glacial melt and sediments has been evoked to explain discrepancies between annual production of basal melt and volume of water required to mobilize quantities of MPDs observed offshore (e.g., Witus et al., 2014; Schroeder et al., 2019; Lepp et al., 2022). For example, the distribution of  $\sim 120$  km<sup>3</sup> of silts deposited offshore of Pine Island Glacier is interpreted to have been sourced in part by high-magnitude purging events of subglacial reservoirs of water and sediments (Witus et al., 2014). While our study includes samples from

those deposits (Table 3.1) and results indicate significant alteration in MPD grain regularity from Pine Island Glacier tills (Figure 3.4), neither our study nor the original found microtexture evidence expected from such high-energy sediment transport (Witus et al., 2014).

In general, the discrepancies between our grain-shape results and theories and observations of subglacial hydrologic transport prompt a consideration of the extent to which sediments are cascaded (Siegfried et al., 2016; Malczyk et al., 2020; Livingstone et al., 2022) downstream along with water during subglacial lake drainage events. Beneath the contemporary West Antarctic Ice Sheet, flux of meltwater between subglacial lake basins has been indirectly observed over tens of meters beneath Thwaites Glacier (Hoffman et al., 2020; Malczyk et al., 2020). Channelized meltwater drainage under modern Thwaites Glacier is inferred to extend to the grounding line from 50 km upstream (Schroeder et al., 2013), yet MPD morphologies from this region suggest discontinuous grain entrainment and sluggish flow (Figure 3.4). In the Thor Iversenbanken region of the central Barents Sea, paleo-subglacial channels connecting basins are ~3-5 km in length (Esteves et al., 2022). While no Thor Iversenbanken samples were included in the microtexture analysis, the Z-scores indicate that grain shapes in till and MPDs are statistically the same (Table 3.2). This observation supports the importance of distance of subglacial hydrologic transport in altering glacial silt morphology (Sweet and Brannan, 2016; Křížek et al., 2017). Drainage between East Antarctic subglacial lakes is recorded over distances an order of magnitude higher (Wingham et al., 2006), implying that MPDs offshore the East Antarctic Ice Sheet could show a higher abundance of glaciofluvial microtextures and/or shape alteration from till grains. Recent insights from modern subglacial lake sediments recovered in the Siple Coast region of the Ross Sea drainage sector suggest that silt-sized sediment can indeed be mobilized downstream between basins (Hodson et al., 2016) and cores from subglacial lakes could represent a high-resolution record of drainage activity (Siegfried et al., 2023). We infer from the grain micromorphology results presented here, however, that a linear, downstream transport of glacial silt through subglacial plumbing networks enroute to the ocean is unlikely. Rather, the continued dominance of features indicating subglacial transport through till deformation, with only minimal overprint of fluvial or meltwater features, suggests that while the final mode of transport and grain sorting may be by subglacial meltwater, it is unlikely this sediment transport process dominates over large areas or for extended periods of time (cf. Simkins et al., 2023).

### **3.5 Conclusions**

Quantitative grain shape and microtexture analyses elucidate whether the shape of silt grains abundant in MPDs record alteration by subglacial meltwater action from their till origins. By calculating grain shape metrics on thousands of grains from six different glacial systems, we find that three-quarters of grains can be described by approximately one-quarter of possible grain circularities, solidities, and eccentricities, providing evidence for efficient subglacial transport and erosive processes operating at the catchment-wide scale. We find that MPD grains preserve



surface textures diagnostic of sustained stress and subglacial grinding but only modest evidence of fluvial transport. This indicates that glacial processes are responsible for the unique grain-size production of MPDs and that, in general, alteration of grain micromorphology through hydrologic transport is recorded more prominently by edge rounding and enhanced grain regularity than by imparting of surface textures. We posit this may be due to an aggregate shielding effect and discontinuous transport distances and processes that are insufficient to leave a pervasive microtextural mark. While regional geology, glacial history, and catchment size likely influence variability in grain-shape distributions to a degree, these data suggest that the greatest grain-shape alteration occurs when till sources are younger and subglacial meltwater flux is in part supplied by supraglacial input. Grain micromorphology can be a valuable addition to traditional glacial and glaciomarine sediment analyses, in particular when subglacial drainage networks are suspected to have been very active (i.e., due to the input of significant supraglacial melt to the bed). Further, we encourage combined empirical and experimental studies that incorporate grain micromorphology to quantifiably connect grain-shape alteration with transport distance to better understand realistic subglacial sediment transport pathways to the ocean.

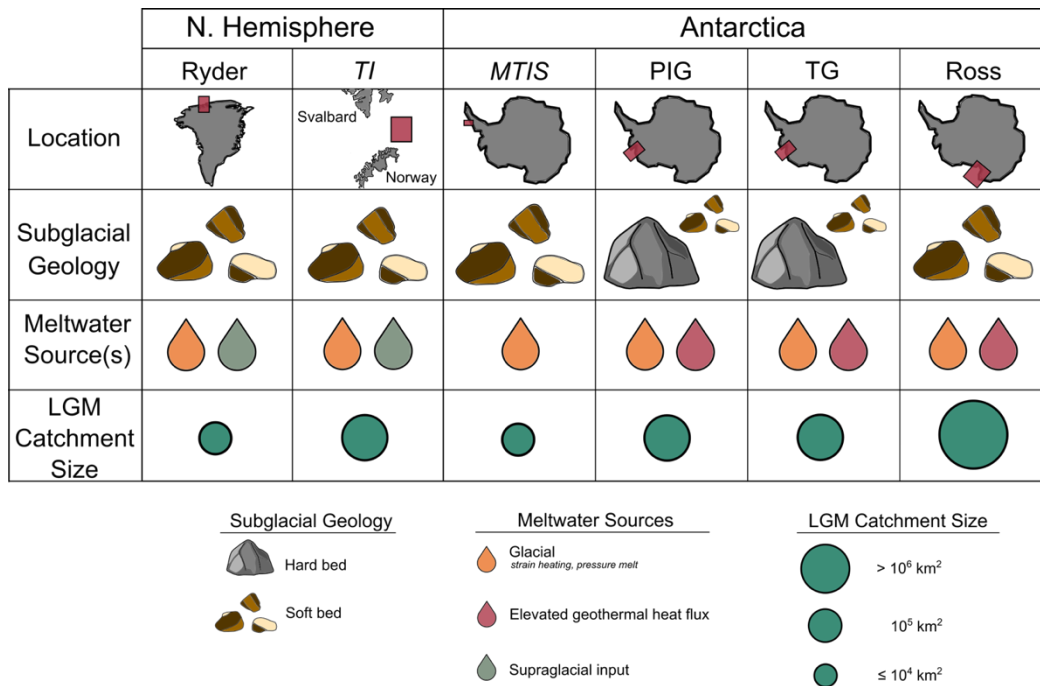
**Table 3.1:** Sample identification, coordinates, facies, water depth, associated glacial system or region, and reference for all samples used in this study. Relict glacial systems and regions that are no longer glaciated are italicized. ^ denotes meltwater plume deposits with no till counterpart. \* indicates samples examined for microtexture analysis. Intervals indicate depth in the sediment core (with core top = 0) from which samples within the facies of interest were collected, and were chosen to avoid lithological boundaries. Negative elevation indicates water depth to core site, while positive elevation is used for reference materials. Diam. = diamicton.

Core ID	Interval <i>cm</i>	Latitude	Longitude	Elevation <i>m</i>	Facies	Glacial System/Region	Reference
Ryder19-6-GC	184-185	80.0095	-51.7408	-633	Meltwater	Ryder Glacier	O'Regan et al., 2021
Ryder19-7-PC	594-595	81.9518	-51.5878	-559	Meltwater	Ryder Glacier	O'Regan et al., 2021
Ryder19-7-PC *	878-879	81.9518	-51.5878	-559	Subglacial till	Ryder Glacier	O'Regan et al., 2021
Ryder19-8-PC *	920-921	81.8928	-51.1315	-238	Subglacial till	Ryder Glacier	O'Regan et al., 2021
Ryder19-9-PC *	622-623	81.8908	-50.9682	-274	Meltwater	Ryder Glacier	O'Regan et al., 2021
Ryder19-9PC *	830-831	81.8908	-50.9682	-274	Meltwater	Ryder Glacier	O'Regan et al., 2021
OD1507-18-GC ^	160-161	81.6266	-62.2989	-520	Meltwater	Petermann Glacier	Jennings et al., 2022
OD1507-31-PC ^	560-561	81.6106	-64.3522	-569	Meltwater	Nares Ice Stream	Jennings et al., 2022
CAGE-15-5-1221-GC	17-18	73.6098	34.6908	-253	Meltwater	<i>Thor Iversenbanken</i>	Esteves et al., 2022
CAGE-15-5-1221-GC	32-33	73.6098	34.6908	-253	Meltwater	<i>Thor Iversenbanken</i>	Esteves et al., 2022
CAGE-15-5-1221-GC	48-49	73.6098	34.6908	-253	Subglacial till	<i>Thor Iversenbanken</i>	Esteves et al., 2022
CAGE-15-5-1221-GC	61-62	73.6098	34.6908	-253	Subglacial till	<i>Thor Iversenbanken</i>	Esteves et al., 2022
CAGE-15-5-1222-GC	103-104	73.6173	34.6011	-310	Meltwater	<i>Thor Iversenbanken</i>	Esteves et al., 2022
CAGE-15-5-1222-GC	117-118	73.6173	34.6011	-310	Meltwater	<i>Thor Iversenbanken</i>	Esteves et al., 2022
CAGE-15-5-1222-GC	126-127	73.6173	34.6011	-310	Subglacial till	<i>Thor Iversenbanken</i>	Esteves et al., 2022
CAGE-15-5-1222-GC	133-134	73.6173	34.6011	-310	Subglacial till	<i>Thor Iversenbanken</i>	Esteves et al., 2022
JM-KA09-GC ^	341-342	74.8819	17.2035	-274	Meltwater	<i>Kveithola Ice Stream</i>	Rüther et al., 2012
DF85-115-PC	145-146	-68.4433	-70.7633	-726	Meltwater	<i>Marguerite Trough Ice Stream</i>	Kennedy & Anderson, 1989
DF85-115-PC	180-181	-68.4433	-70.7633	-726	Meltwater	<i>Marguerite Trough Ice Stream</i>	Kennedy & Anderson, 1989
DF85-115-PC	200-201	-68.4433	-70.7633	-726	Subglacial till	<i>Marguerite Trough Ice Stream</i>	Kennedy & Anderson, 1989
DF85-115-PC	205-206	-68.4433	-70.7633	-726	Subglacial till	<i>Marguerite Trough Ice Stream</i>	Kennedy & Anderson, 1989
DF85-116-PC	26-27	-68.4833	-70.6000	-650	Meltwater	<i>Marguerite Trough Ice Stream</i>	Kennedy & Anderson, 1989
DF85-116-PC	82-83	-68.4833	-70.6000	-650	Meltwater	<i>Marguerite Trough Ice Stream</i>	Kennedy & Anderson, 1989
DF85-116-PC	102-103	-68.4833	-70.6000	-650	Subglacial till	<i>Marguerite Trough Ice Stream</i>	Kennedy & Anderson, 1989

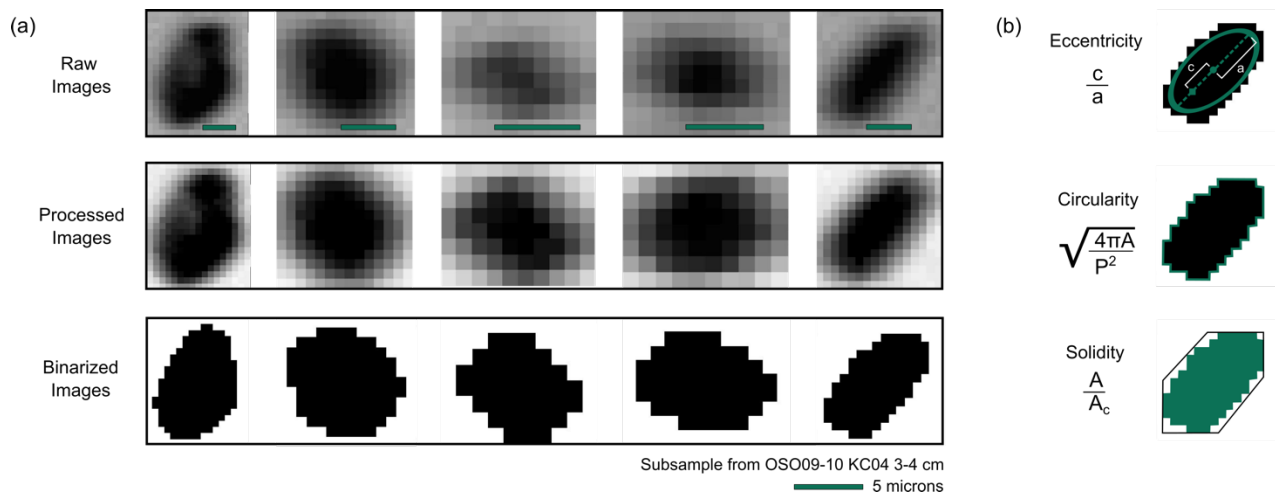
Core ID	Interval <i>cm</i>	Latitude	Longitude	Elevation <i>m</i>	Facies	Glacial System/Region	Reference
DF85-116-PC	143-144	-68.4833	-70.6000	-650	Subglacial till	<i>Marguerite Trough Ice Stream</i>	Kennedy & Anderson, 1989
OSO09-10 KC04*	3-4	-72.6971	-107.1105	-729	Meltwater	Pine Island Glacier	Witus et al., 2014
OSO09-10 KC04	200-201	-72.6971	-107.1105	-729	Subglacial till	Pine Island Glacier	Witus et al., 2014
OSO09-10 KC18	30-31	-73.3835	-106.871	-894	Meltwater	Pine Island Glacier	Kirshner et al., 2012
OSO09-10 KC25	75-76	-73.2570	-107.1057	-838	Subglacial till	Pine Island Glacier	Kirshner et al., 2012
PIG-B	1-2	-75.0754	-100.432	-725	Meltwater	Pine Island Glacier	Smith et al., 2017
PIG-B	18-19	-75.0754	-100.432	-725	Ice- proximal diam.	Pine Island Glacier	Smith et al., 2017
PIG-B	80-81	-75.0754	-100.432	-725	Ice- proximal diam.	Pine Island Glacier	Smith et al., 2017
NBP20-02 KC26 *	70-72	-75.0215	-100.7513	-805	Ice- proximal diam.	Pine Island Glacier	This study
NBP19-02 KC04	170-172	-74.94	-106.18	-469	Ice- proximal diam.	Thwaites Glacier	Lepp et al., 2022
NBP19-02 KC13	10-12	-74.911	-106.953	-463	Meltwater	Thwaites Glacier	Clark et al., 2023
NBP19-02 JGC11	62-63	-75.058	-107.299	-752	Ice- proximal diam.	Thwaites Glacier	Clark et al., 2023
NBP19-02 KC15 *	80-82	-74.871	-106.333	-545	Meltwater	Thwaites Glacier	Clark et al., 2023
NBP19-02 JGC17	6-7	-74.887	-106.316	-507	Meltwater	Thwaites Glacier	Clark et al., 2023
NBP19-02 JGC17	106-107	-74.887	-106.316	-507	Ice- proximal diam.	Thwaites Glacier	Clark et al., 2023
NBP19-02 KC23	60-62	-75.07	-104.23	-677	Ice- proximal diam.	Thwaites Glacier	Lepp et al., 2022
NBP19-02 KC23	130-132	-75.07	-104.23	-677	Ice- proximal diam.	Thwaites Glacier	Lepp et al., 2022
NBP20-02 KC33	200-202	-74.64	-106.18	-397	Meltwater	Thwaites Glacier	Lepp et al., 2022
NBP20-02 KC67	50-52	-74.84	-104.46	-613	Meltwater	Thwaites Glacier	Lepp et al., 2022
NBP15-02 KC17	170-171	-75.874	179.666	-549	Meltwater	Western Ross Sea	Prothro et al., 2018
NBP15-02 KC19	115-116	-76.03	177.210	-455	Subglacial till	Western Ross Sea	Halberstadt et al., 2016
NBP15-02 KC19	145-146	-76.03	177.210	-455	Subglacial till	Western Ross Sea	Prothro et al., 2018
NBP15-02 KC22 *	115-116	-75.43	176.196	-354	Subglacial till	Western Ross Sea	Halberstadt et al., 2016
NBP15-02 KC22	120-121	-75.43	176.196	-354	Subglacial till	Western Ross Sea	Halberstadt et al., 2016
NBP15-02 KC24	79-80	-75.671	176.446	-450	Meltwater	Western Ross Sea	Simkins et al., 2017
Qaanaaq_1A	-	77.493	-69.242	372	Cryoconite	Qaanaaq Glacier	This study
Qaanaaq_2A	-	77.496	-69.229	456	Cryoconite	Qaanaaq Glacier	This study
Qaanaaq_3A	-	77.497	-69.200	556	Cryoconite	Qaanaaq Glacier	This study
SDM94	-	-81.643	-148.773	615	Basal ice debris	Siple Dome	This study
19-KP-H6	-	-75.215	-110.960	84	Fringe debris	Kay Peak, Pope Glacier	This study

**Table 3.2:** Results of two-tailed Z test and associated p-values performed on grain shape of meltwater plume deposit and till populations from each system. Z scores are absolute values. Shape metrics with statistically significantly different populations ( $Z > 3.0$ ) are shown in bold. Difference in means for those statistically significant metrics is presented with 95 % confidence interval calculated from 1,000 bootstrap replicates. Note the small values reflect both the range of the metric itself [0, 1] and supports the rejection of the null hypothesis that MPD and till sample populations are the same. Abbreviations of the glacial systems/regions are the same as in Figure 3.1.

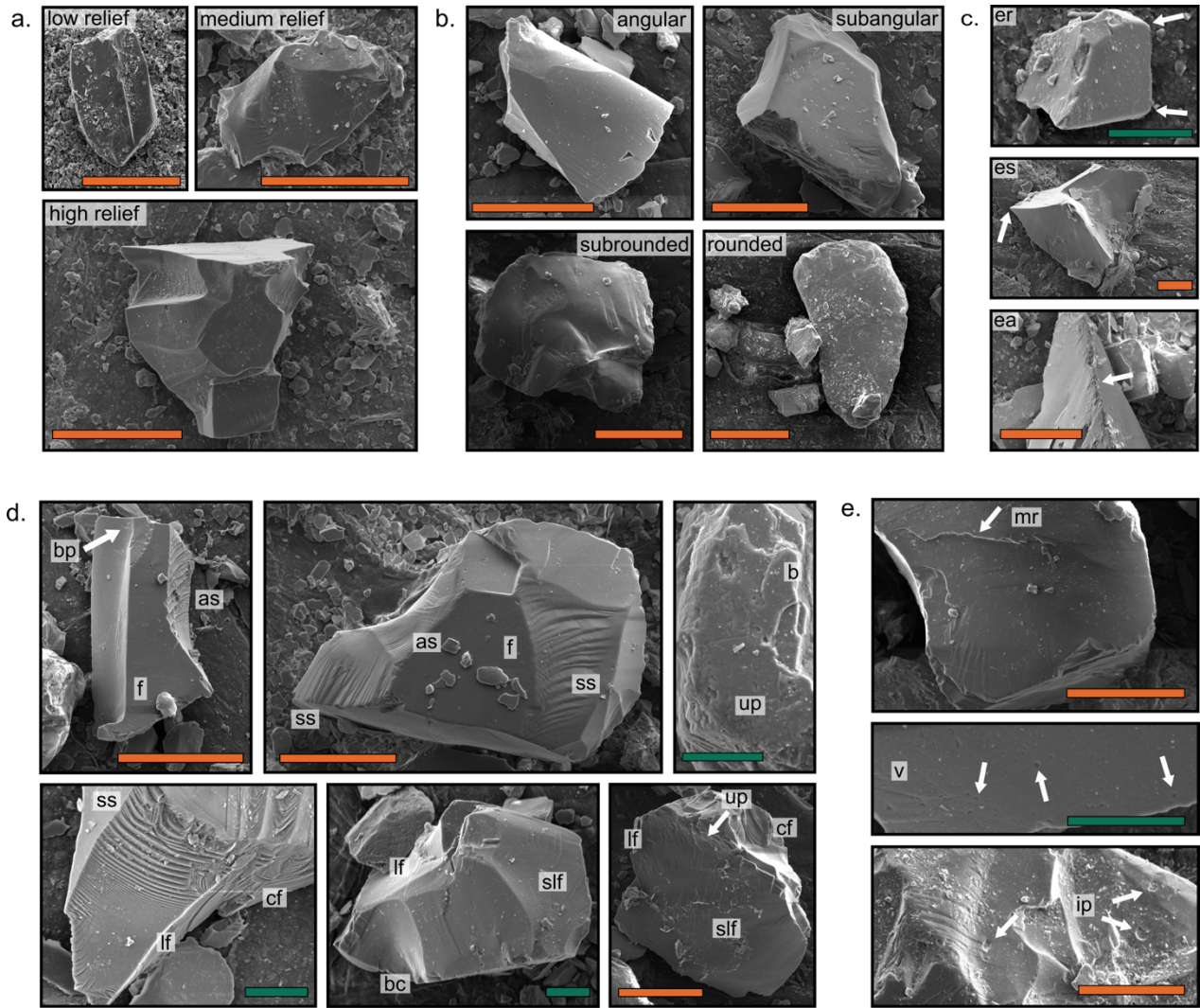
		Ryder	TI	MTIS	PIG	TG	Ross Sea
Aspect Ratio	Z-Score	0.4131	0.01381	<b>5.8839</b>	2.9297	0.1616	0.3673
	p-value	0.680	0.581	4.008e <sup>-9</sup>	3.39e <sup>-3</sup>	0.872	0.713
	Difference in Means	-	-	$\frac{1.91e^{-2}}{+6.31e^{-3}} - 6.49e^{-3}$	-	-	-
Circularity	Z-Score	<b>11.313</b>	2.1265	0.6375	<b>3.7678</b>	0.5258	<b>6.4984</b>
	p-value	< 2.2e <sup>-16</sup>	0.173	0.5238	1.65e <sup>-4</sup>	0.599	8.12e <sup>-11</sup>
	Difference in Means	$\frac{5.30e^{-2}}{+9.92e^{-3}} - 9.68e^{-3}$	-	-	$\frac{1.60e^{-2}}{+8.34e^{-3}} - 8.66e^{-3}$	-	$\frac{3.36e^{-2}}{+1.06e^{-2}} - 9.68e^{-3}$
Eccentricity	Z-Score	0.6247	0.4847	<b>4.7231</b>	2.5914	0.0144	0.2989
	p-value	0.532	0.386	2.32e <sup>-6</sup>	9.56e <sup>-3</sup>	0.989	0.765
	Difference in Means	-	-	$\frac{3.95e^{-2}}{+1.64e^{-2}} - 9.52e^{-2}$	-	-	-
Solidity	Z-Score	<b>9.1276</b>	1.832	0.1234	<b>3.214</b>	1.056	<b>5.377</b>
	p-value	< 2.2e <sup>-16</sup>	0.0570	0.9018	1.31e <sup>-3</sup>	0.291	7.57e <sup>-8</sup>
	Difference in Means	$\frac{3.34e^{-2}}{+7.13e^{-3}} - 6.67e^{-3}$	-	-	$\frac{1.05e^{-2}}{+6.52e^{-3}} - 6.28e^{-3}$	-	$\frac{2.02e^{-2}}{+6.88e^{-3}} - 7.22e^{-3}$



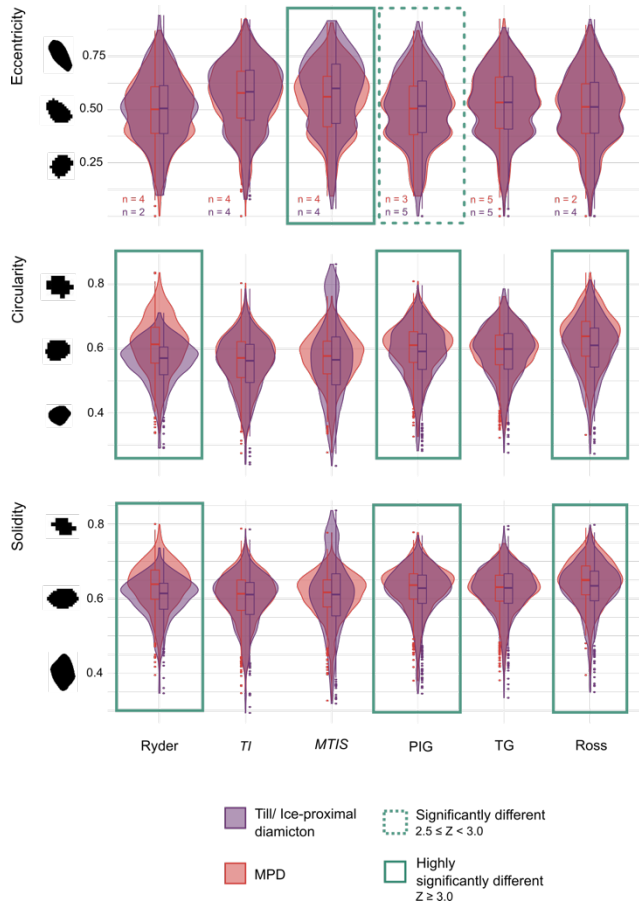
**Figure 3.1.** Graphical map illustrating components of a glacial system that may influence grain-shape alteration and meltwater production compare between study sites. Subglacial geology is binarized into hard (i.e., crystalline) and soft (clastic or carbonate sedimentary) beds. Relict glacial systems and deglaciated setting names are italicized. TI = Thor Iversenbanken, MTIS = Marguerite Trough Ice Stream, PIG = Pine Island Glacier, TG = Thwaites Glacier, Ross = Ross Sea, LGM = Last Glacial Maximum.



**Figure 3.2.** Workflow for automated grain shape analysis. (A) Raw images captured by the Bettersizer S3 Plus, images post-processing, and in binarized forms. (B) Metrics and associated equations calculated for each grain.  $c$  = distance between ellipse foci and center;  $a$  = length of semi-major axis;  $A$  = area,  $P$  = perimeter,  $A_c$  = area of the convex hull that encompasses the grain.

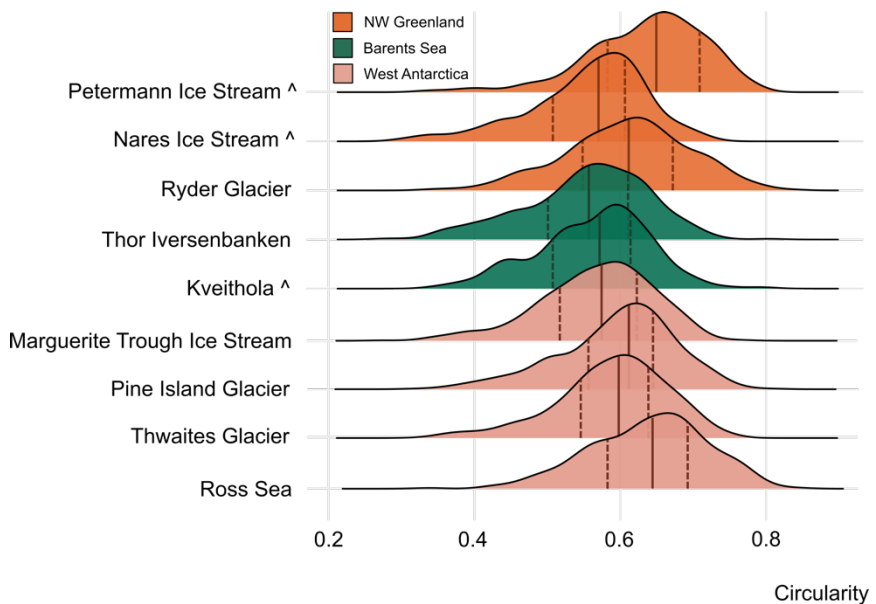


**Figure 3.3.** Microtextures observed on quartz grains in the <math><63\ \mu\text{m}</math> size fraction (silt) from select till and meltwater plume deposit samples. Orange scale bar =



**Figure 3.4.** Violin plots for paired MPDs and tills, or ice-proximal diamictos (Table 3.1), for each region with the number of samples from each grain type shown at the bottom of grain eccentricity. Box plots within each violin show the interquartile ranges. Those pairs outlined in solid green denote populations that are highly significantly different, while the dashed green line indicates pairs that are significantly different as determined by a two-type Z test. Refer to Figure 3.2 for shape metric equations. TI = Thor Iversenbanken; MTIS = Marguerite Trough Ice Stream, PIG = Pine Island Glacier, TG = Thwaites Glacier, Ross = Ross Sea.

**Figure 3.5.** Circularity of meltwater plume deposit grains with first and third quartiles indicated by dashed lines and the median by a solid line. Glacial systems are grouped and colored by region. Samples with no till counterpart are denoted by ^ (see also Table 3.1).



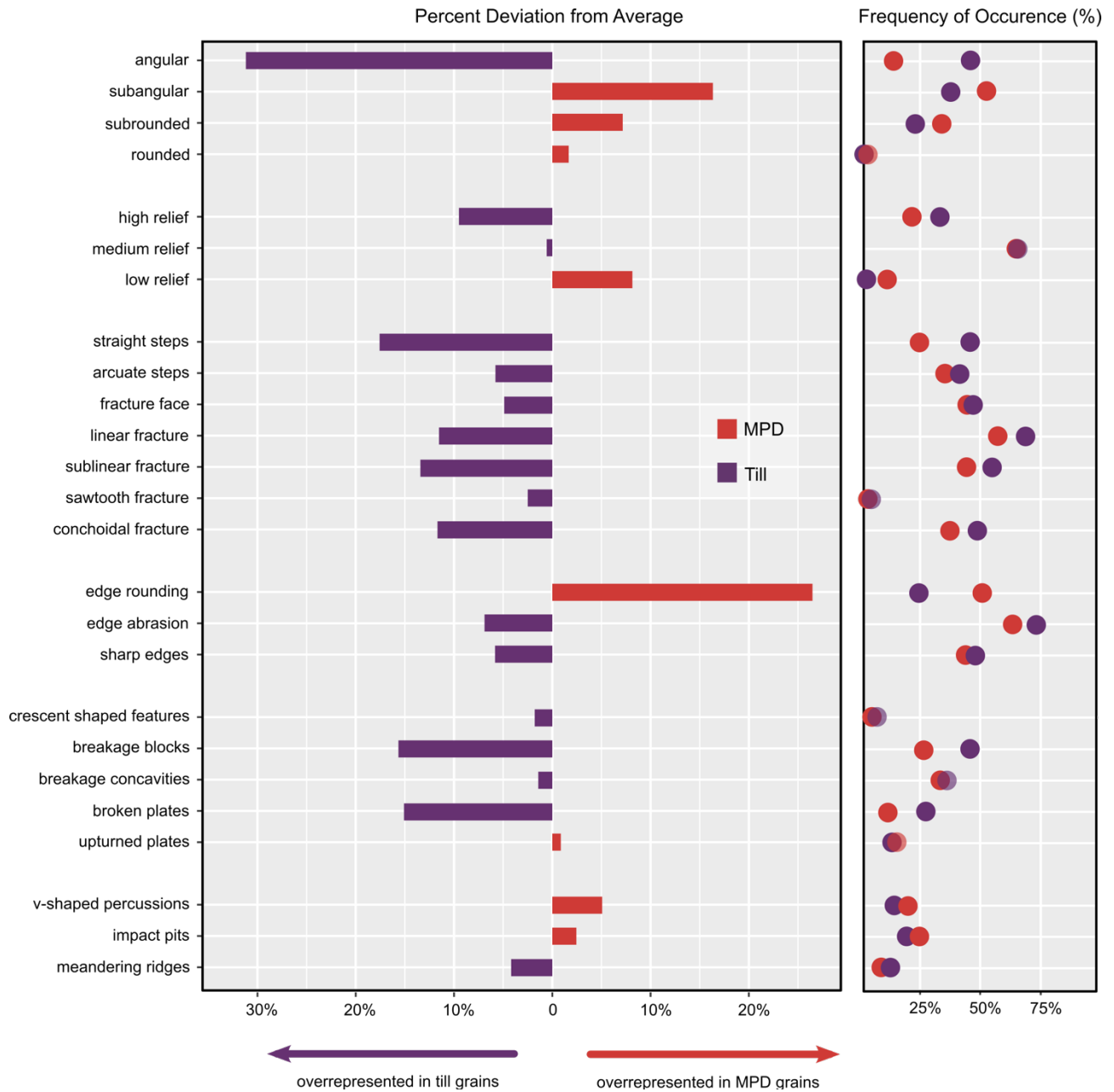


**Figure 3.6.** Overrepresentation and frequency of occurrence of microtextures in both grain populations observed on 132 quartz grains (63 MPD grains, 69 till/ice-proximal diamicton grains). Refer to Figure 3.3 for examples of microtextures. Angular grains and all fracture types, as well as edge abrasion, are overrepresented in till grains, whereas MPDs exhibit a higher proportion of subangular and subrounded grains with edge rounding. Many mechanical microtextures (e.g., fracture faces, linear and sublinear fractures) are observed at comparable frequencies in both grain populations.



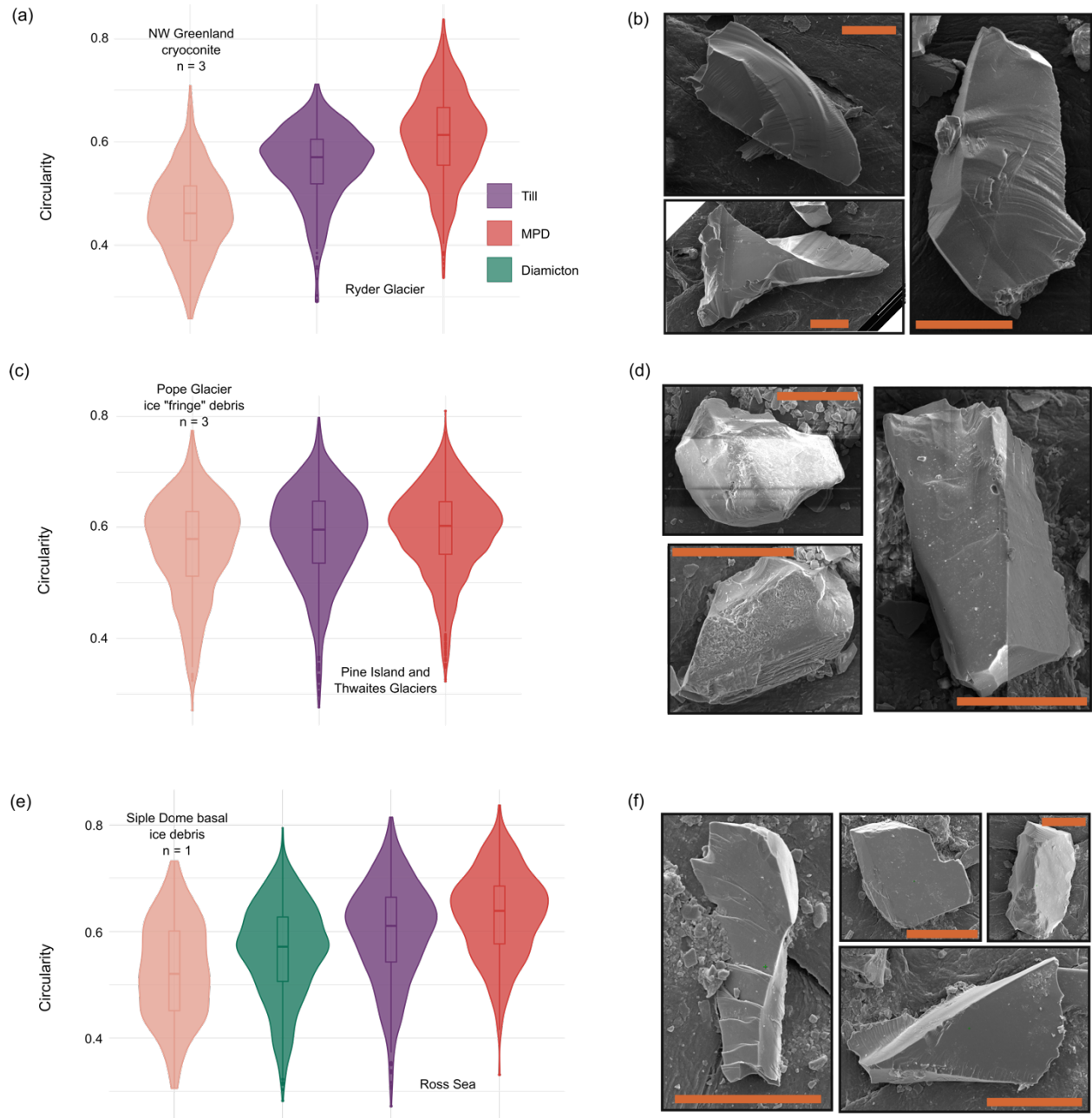


**Figure 3.7.** Visualization of grain shape evolution. (A), (C), and (E) show grain circularity for supraglacial or basal ice reference material in comparison to glacial-marine diamicton, till, and meltwater plume deposits from a neighboring glacial system. SEM images of (B) cryoconite, (D) basal fringe debris, and (F) basal ice debris show highly fractured and elongated grains that are less common following subglacial transport. Note that in (C) the middle violin includes samples from ice-proximal diamicton from offshore Pine Island and Thwaites glaciers, as well as subglacial till samples from Pine Island Glacier (Table 3.1). Scale bar in (B), (D), and (F) is 20 microns.

## Chapter 4: Isotopic signals of subglacial meltwater drainage into the Amundsen Sea Sector of West Antarctica

*Conducted with support from:* Lauren E. Miller, Jane K. Willenbring, Lisa C. Herbert, and Santiago Munevar Garcia. A manuscript in preparation for submission to *Geophysical Research Letters*.<sup>4</sup>

### 4.1 Introduction

Expulsion of fresh, subglacial meltwater into the ocean generates buoyancy-driven plumes that initiate at the grounding zone of marine-terminating glaciers (Hewitt, 2020). The migration and dynamics of those plumes have implications for submarine melting of floating ice shelves (Jenkins, 2011; Le Brocq et al., 2013; Alley et al., 2016; Wei et al., 2020), nutrient cycling (e.g., Hawkings et al., 2020; Herbert et al., 2020; Vick-Majors et al., 2020), ocean stratification and circulation (Begeman et al., 2018; Silvano et al., 2018; Hewitt, 2020 and references therein; Davis et al., 2023), and sediment transport offshore (Witus et al., 2014; Dowdeswell et al., 2015; Prothro et al., 2018; Lepp et al., 2022). Modern plumes emanating from the Greenland Ice Sheet and tidewater glaciers in Svalbard have been studied through remote sensing methods (e.g., Chu et al., 2009, 2012; Darlington, 2015; Dowdeswell et al., 2015), but such observations are limited in the Antarctic, where plume migration and transition to neutral buoyancy often occurs beneath floating ice. Marine sediment cores record evidence of meltwater discharge on longer timescales than observational data (e.g., Witus et al., 2014; O'Regan et al., 2021; Jennings et al., 2022; Lepp et al., 2022), but proxies that relate sedimentary deposits from meltwater plumes to plume properties are lacking.

Isotopic ratios of sediment porewaters from (de)glaciated environments are geochemical archives that can be used to study a wide array of processes, including biogeochemical cycling (e.g., Herbert et al., 2023), subglacial regelation and sediment entrainment (Iverson and Souchez, 1996), paleo-subglacial hydrology (Kuhn et al., 2017, Neuhaus et al., 2021), and changes in past ocean salinity (e.g., Adkins et al., 2002). Because glacial ice and thus subglacial meltwater have a distinctly different stable water isotope ratio ( $\delta^{18}\text{O}$  and  $\delta\text{D}$ ) than ambient ocean water (e.g., Hellmer et al., 1998; Meredith et al., 2018; Silvano et al., 2018; Biddle et al., 2019), sediment porewater may also record isotopic evidence of subglacial meltwater drainage into the ocean especially in ice-proximal regions, but this potential proxy has not previously been tested.

In this study, we present stable isotope ratios of interstitial waters from ten sediment cores collected at varying distances to the calving line of marine-terminating glaciers in the eastern Amundsen Sea, including Pine Island and Thwaites glaciers and the glaciers feeding the Dotson-Getz ice shelf system (Figure 4.1). Downcore porewater profiles are interpreted

---

<sup>4</sup> APL: conceptualization, formal analysis, investigation, methodology, project administration, resources, software, visualization, writing – original draft. LEM: conceptualization, funding acquisition, methodology, project administration, resources, supervision, writing – review & editing. JKW: formal analysis, investigation, resources, supervision, validation. LCH: formal analysis, methodology. SMG: investigation, resources, software.

alongside changes in sediment facies and oxygen isotope concentrations as predicted by an isotope diffusive model. Additionally, for a select group of cores, we present ratios of meteoric to lithogenic (stable) beryllium isotopes of sediments at the same core depth from which porewater samples were collected. Meteoric  $^{10}\text{Be}$  is produced atmospherically through spallation reactions and is deposited to the Earth's surface, including atop ice sheets and the open ocean, through precipitation or dust (Willenbring and von Blanckenburg, 2010). Subglacial drainage events therefore deliver above-background concentrations of meteoric  $^{10}\text{Be}$  into the ocean that adsorb to glaciomarine sediments. Normalizing meteoric  $^{10}\text{Be}$  to stable, terrestrial  $^9\text{Be}$  corrects for grain-size enrichments (e.g., Wittmann et al., 2012; Valletta et al., 2018), and this ratio has been measured in marine sediments from East Antarctica to identify periods of enhanced meltwater input into the ocean (Valletta et al., 2018; Behrens et al., 2022) and distinguish between glaciomarine depositional environments (e.g., sub-ice shelf or open marine; Yokoyama et al., 2016; White et al., 2019). These complementary data therefore not only provide an established proxy against which to interpret porewater profiles, but are also the first of their kind to be published from Amundsen Sea sediments and contribute to the growing terrestrial dataset of beryllium isotope measurements from the Antarctic.

## 4.2 Methodology

### 4.2.1 Porewater sampling and stable water isotope analysis

Sediment porewater samples were collected during three research cruises aboard the *RV/IB Nathaniel B. Palmer* in 2019, 2020, and 2022 using Rhizon filters that extract sediment porewater through a 0.15 micron-filter using a vacuum. Rhizons can sample porewater at high-resolution intervals (i.e., sub-cm vertical resolution; Seeberg-Elverfeldt et al., 2005; Herbert et al., 2023) from up to 50 m core depth while negligibly disturbing sediment stratigraphy (Dickens et al., 2007), an important advantage over the traditional squeeze method for porewater extraction. A comparison of porewater geochemistry collected using Rhizons and by squeezing found that, in general, both methods yield comparable results for oxygen isotopes (Miller et al., 2014). A minimum of two milliliters (mL) of porewater was allowed to collect in the syringe before turning the luer lock and disconnecting the syringe from the Rhizon (Figure 4.2). Porewater was sampled from kasten cores at a varied resolution based on core recovery and lithology. Some sites had multiple deployments, including multicores which often recover a well-preserved sediment-water interface and a rosette of Niskin bottles, both of which provided reference material (Table 4.1). Reference waters were either siphoned or dispensed (multicore and Niskin bottle, respectively) into rinsed vials, but were not filtered.

Samples were transferred from syringes into vials with no headspace, capped immediately, and wax sealed to prevent atmospheric exchange. Vials were stored at 4 °C and analyzed for oxygen and hydrogen isotope concentrations using a dual-inlet isotope ratio mass

spectrometer at the United States Geological Survey Reston Stable Isotope Lab in Reston, Virginia. Isotope ratios are reported using standard delta notation and are calculated by

$$\delta^{18}O = \left( \frac{\frac{^{18}O}{^{16}O} \text{ sample}}{\frac{^{18}O}{^{16}O} \text{ standard}} - 1 \right) * 1000 \text{ ‰} \quad \text{Eqn. 1}$$

$$\delta D = \left( \frac{\frac{^2H}{^1H} \text{ sample}}{\frac{^2H}{^1H} \text{ standard}} - 1 \right) * 1000 \text{ ‰} \quad \text{Eqn. 2}$$

where the standard is Vienna Standard Mean Ocean Water (VSMOW2). Two-sigma uncertainties are 0.2 per mille (‰) and 2 ‰ for  $\delta^{18}O$  and  $\delta D$ , respectively. We use these measurements to calculate deuterium excess, a metric which may vary in response to kinetic fractionation and can be indicative of different moisture origins (e.g., Masson-Delmotte et al., 2005). Deuterium excess ( $d$ ) is calculated according to Dansgaard (1964) using the equation

$$d = \delta D - 8 * \delta^{18}O \text{ ‰} \quad \text{Eqn. 3}$$

#### 4.2.2 Sediment porosity and isotopic diffusion modeling

Moisture content was collected on each core in 10-cm intervals, with increased measurements taken around lithological transitions or discrete event deposits. These data were first collected as percent mass lost between wet and 48-hour oven-dried bulk sediment, and were then converted to porosity following the methods outlined in Blake (2008) using a sediment density of  $2.7 \text{ g cm}^{-3}$  and a seawater density of  $1.024 \text{ g cm}^{-3}$ . Our 1-D vertical diffusion model solves the diffusion equation

$$\frac{\partial C}{\partial t} = D_{sed} \left( \frac{\partial^2 C}{\partial y^2} \right) \quad \text{Eqn. 4}$$

using the forward Euler method, where downcore changes in isotopic concentration are calculated every 0.5 cm according to the analytical solution

$$\frac{C - C_0}{C_s - C_0} = \text{erfc} \left( \frac{y}{2 * \sqrt{D_{sed} * t}} \right) \quad \text{Eqn. 5}$$

where  $C$  is the calculated concentration,  $C_s$  is isotopic concentration at the water-sediment interface,  $C_0$  is the concentration in the upcore interval,  $D_{sed}$  is the diffusion coefficient for the isotope in sediment,  $y$  is core depth, and  $t$  is total time (Turcotte and Schubert, 2014). The model is run for a total  $t$  of 10,000 years, which corresponds to the assumed maximum time of sediment

accumulation based on deglacial history and radiocarbon age constraints in core *NBP20-02* KC33 (cf. Chapter 2; Lepp et al., 2022). At the start of each run, we assumed porewater through the core was in isotopic equilibrium with the reference material (Table 4.1) and that the boundary layer at the sediment-water interface is small enough to not resist diffusion. For each sediment core, mean porosity was calculated by facies modified from prior studies (Table 4.2, Lepp et al., 2022; Clark et al., 2023). For cores published in this study, assigned facies were based off of shipboard lithologic descriptions and following the aforementioned references. Facies include laminated silty clay (Sl), bioturbated silty clay (Sb), laminated sandy silt (Ssl), massive diamicton (Dm) and stratified diamicton (Ds). Mean facies porosity was then used to calculate a facies-averaged value of  $D_{sed}$  using:

$$D_{sed} = D * \frac{\alpha}{\theta^2} \quad \text{Eqn. 6}$$

where  $D$  is the diffusion coefficient of the modeled isotope in water,  $\alpha$  is a constant describing the ratio between viscosity of the bulk solution to that of the interstitial solution (assumed here to be 1, after Li and Gregory, 1974; Neuhaus et al., 2021), and  $\theta$  is tortuosity. For a porous medium, tortuosity describes the ratio between the actual flow path length and the straight-line distance (Bear, 1988) and is calculated as

$$\theta = \alpha - \ln(\varphi^2) \quad \text{Eqn. 7}$$

where  $\varphi$  is sediment porosity (Boudreau, 1996). Between all ten cores, the diffusion coefficients used here ranged between  $2.213e^{-2}$  and  $2.508e^{-2} \text{ m}^2 \text{ y}^{-1}$  for glaciomarine sediments and between  $1.57e^{-2}$  and  $1.93e^{-2} \text{ m}^2 \text{ y}^{-1}$  for glacial diamicton (Table 4.2). The coefficients derived for diamicton facies are consistent with those used for isotopic modeling of  $\delta^{18}\text{O}$  through subglacial till recovered from Subglacial Lake Whillans (Neuhaus et al., 2021). Previous, analogous studies deemed advection to have a negligible effect on water isotope composition on similar timescales and at much greater sediment thicknesses than considered here (>40 m of glaciogenic clays and tills; Remenda et al., 1994). Additionally, shear strength measurements for cores are quite low (cf. Chapter 2, Lepp et al., 2022; Clark et al., 2023) indicating that, on the depth scale considered here, marine sediments from this region have experienced minimal sediment compaction that would encourage advection (e.g., Dickens et al., 2007); therefore, we consider diffusion only.

#### 4.2.3 Beryllium isotope leaching and analysis

Bulk sediment from discrete intervals from which porewater was extracted was oven-dried for 48 hours at 60 °C. We placed ~0.5 g into an acid-cleaned 15 mL centrifuge tube and prepared a number of chemical solutions to measure the native  $^9\text{Be}$  and to extract and purify the meteoric  $^{10}\text{Be}$ . To extract the amorphous oxide-bound beryllium, samples were leached in an ultrasonic bath at 50 °C for 24 hours via a 10 mL solution of 0.5 M HCl. An aliquot was extracted for later elemental analysis via inductively-coupled plasma mass spectrometry (ICP-

MS). To extract the crystalline oxide-bound beryllium, 10 mL of 1 M hydroxylamine hydrochloride solution was added to the centrifuge tubes with the sediment and placed into the ultrasonic bath at 70 °C for 4 hours with manual over-head shaking every 10 minutes. An aliquot was extracted, combined with the other aliquot for ICP-MS (adapted from Ebert et al. (2012)), and then diluted with 2% v/v nitric acid. Analysis was performed on an Agilent 8900 triple quadrupole ICP-MS attached to an Agilent SPS-4 autosampler at Stanford University, where the employed methods were developed and optimized for the best sensitivity for beryllium (Table A4.1). Instrumental blanks were run in parallel with samples and were below the detection limits for all analyzed elements.

Leachate solutions were spiked with ~200 mg <sup>9</sup>Be carrier and homogenized before 2 mL HF was added. This solution was dried down then dissolved in 2 additional mL of 50% HF acid and dried down completely. To remove Ca, Al, Mg, and other fluorides, 10 mL of ultrapure water was added to the residue and leached on a hot plate for 1 hour. The remaining liquid containing water-soluble Be was removed via pipette and purified following protocol from von Blanckenburg et al. (2004) that was adapted for meteoric beryllium. The solution was filtered through a series of columns containing either anion or cation resin conditioned with 6 M HCl and 0.4 M oxalic acid, respectively, that removes unwanted Fe and Al while Be is allowed to filter through. Lastly, hydroxides of Be were precipitated from the solution that had been eluted from the cation exchange column by adding ammonia drop-wise until pH ~9. During this step, any remaining K, Na, Ca, and Mg were left in solution. After precipitation, we separated the supernate and the sample precipitate by centrifuge and washed it with distilled water and reprecipitated it to remove any remaining Boron (an isobar of <sup>10</sup>Be). The Be(OH)<sub>2</sub> precipitate was then dried for 2 hours at 80 °C, then overnight at 200 °C and then oxidized by flame at >850 °C to form BeO. We then pressed the BeO and Niobium powder into cathodes for accelerated mass spectrometry analysis at the Center for Accelerator Mass Spectrometry at Lawrence Livermore National Lab (Table 4.3).

### 4.3 Results and discussion

Prior studies that leveraged stable water isotopes of sediment porewater found the most reliable isotopic signals to be preserved in clay-rich sediments due to low permeability that prevents porewater displacement through diffusive or advective flow (e.g., Remenda et al., 1994; Kumar et al., 2020). Sedimentological characterizations of cores from this region, including some of the same cores used in this study, indicate that meltwater plume deposits and diamicton matrices contain high proportions (~20-45 %) of clay-sized grains (Lepp et al., 2022; Clark et al., 2023). This context increases our confidence that the measured porewater signals are, in general, representative and have not been substantially altered post-deposition.

Regardless of the isotopic composition of the initial interval, diffusive processes alone are unable to explain the observed composition of sampled sediment porewater (Figure 4.3). While, in general, both the diffusive model and sampled porewater indicate a shift towards isotopically lighter porewater downcore, diffusion-based predictions of porewater chemistry are an order of magnitude lower than is observed in most sediment cores (Figure 4.3; Figure A4.1). Additionally, stable isotope signatures for reference materials vary by only ~0.6 ‰ across the entire study site; if diffusive processes were primarily governing downcore isotopic concentration in sediment porewaters, we would expect the observed porewater compositions to mirror one another closely. Instead, we see a range of 9.81 ‰ between measured isotopes from

all cores (max = 0.54 ‰, min = -9.27 ‰) which supports interpretation of porewater composition as a reflection of environmental conditions and water source. Miller et al. (2014) found that, compared to porewater extraction via whole-round squeezing,  $\delta^{18}\text{O}$  measured from Rhizon samples are on average 0.04 ‰ higher (i.e., more enriched) which they attribute to diffusive fractionation through the filter membrane. Again, these discrepancies are an order of magnitude lower than the observed variability we see and thus we discount such processes as having an important effect on our results or interpretations (Figure 4.3; Figure A4.1).

While variation in deuterium excess does not appear to be related to core location, we find that  $\delta^{18}\text{O}$  is significantly ( $p < 0.05$ ) more depleted at increasingly southern latitudes and eastern longitudes (Figure 4.4), though the correlation is weak ( $r^2 < 0.2$ ). This corresponds to an overall isotopically lighter porewater signal sampled from core locations that are closer to the ice margin, and lighter porewater in cores proximal to Thwaites and Pine Island glaciers than those from the Dotson-Getz region (Figure 4.1). Wei et al. (2020) posit that subglacial meltwater drainage enhances ocean-driven basal melt at the Getz Ice Shelf, but the locations of highest predicted subglacial outflow in their study are further west than the cores from which porewater was taken (KC06, KC22, and KC29). Persistent, and episodically high-magnitude, subglacial discharge from Thwaites and Pine Island glaciers is inferred from physical and geochemical properties of marine sediments collected offshore (e.g., Witus et al., 2014) which occur in laminated and bioturbated facies (S1 and S<sub>b</sub>, respectively, Lepp et al., 2022; Clark et al., 2023). However, mean porewater  $\delta^{18}\text{O}$  within these facies are between -0.49 ‰ and -0.85 ‰, which is inconsistent with a pure glacial source (cf. Masson-Delmotte et al., 2008) and is compositionally more similar to modified circumpolar deep water (mCDW) in the Amundsen Sea (0.05 ‰, Biddle et al., 2019). Buoyant plumes of subglacial meltwater and sediments can travel several to over tens of kilometers from the grounding line (e.g., Dowdeswell et al., 2015; Lepp et al., 2022; Gwyther et al., 2023), and the isotopic data from porewater suggest that, above these core sites, plumes were traveling at sufficiently shallow water depths to leave only a minor meltwater signal at the sediment-water interface.

Meteoric  $^{10}\text{Be}$  concentrations in all samples are on the order of  $10^7$  to  $10^9$  atoms  $\text{g}^{-1}$  (Table 4.3), which is consistent with Pliocene sediments from Wilkes Land (Valletta et al., 2018), glaciomarine sediments from Prydz Bay (White et al., 2019), and, interestingly, glaciolacustrine sediments from lakes Maruwan Oike and Skallen, East Antarctica (Spronson et al., 2021). Ratios of  $^{10}\text{Be}/^9\text{Be}$  within facies S1 and S<sub>b</sub> are elevated compared to other facies in all cores except for NBP19-02 KC15, which shows a fairly consistent beryllium isotopic signature and a discrete elevated ratio in facies S<sub>b</sub> at 181 cm core depth (Figure 4.3). We see that the elevated beryllium ratios, interpreted as marking periods of enhanced subglacial meltwater drainage, do not show a consistent pattern of aligning with isotopically-depleted porewater samples. It appears, therefore, that beryllium isotopes of meltwater plume deposits are more suitable for reconstructing meltwater processes and depositional settings than are stable water isotopes of porewater. Though, given the similarities to mCDW, the latter could be more appropriate for studying changes in bottom water chemistry and deep-water masses through time.

The widest range of observed  $\delta^{18}\text{O}$  in porewater, including the most depleted outliers, were sampled from massive diamicton (facies D<sub>m</sub>, Figure 4.5). In ice-proximal settings, massive or structureless diamicton is often interpreted as sediment deposition near the grounding zone through sediment gravity flows and/or basal ice meltout (e.g., Powell et al., 1996; Domack et al., 1999; Hillenbrand et al., 2005; Prothro et al., 2018; Smith et al., 2019; Lepp et al., 2022; Clark et

al., 2023). Sediment gravity flows leading to such deposits may be triggered by point-source meltwater release (i.e., where a subglacial channel intersects the grounding line) that, if the ice-margin position is stable, can produce meltwater fans over time (e.g., Dowdeswell et al., 2015; Simkins et al., 2017). The isotopic porewater signature indicates these waters are, at least in part, subglacial in origin, and their retention in facies Dm suggests these interstitial waters were preserved due to rapid sediment mobilization and deposition near the point of water drainage at the grounding zone. Concentrations of  $^{10}\text{Be}$  in this facies are lower by at least an order of magnitude compared to finer-grained sediment facies, which may indicate that the source of the freshwater (i.e., meltwater plume) evacuated fine-grained sediments with higher meteoric beryllium concentrations and remobilized grounding-zone sediments with lower  $^{10}\text{Be}/^9\text{Be}$  ratios (Figure 4.3). An alternate interpretation is that the Dm preserving relatively depleted porewaters are, in fact, “soft” subglacial till deposits, which are difficult to distinguish from ice-proximal diamicton due to similarities in shear strength and sedimentological characteristics (cf. Halberstadt et al., 2018). However, the measured  $\delta^{18}\text{O}$  are more enriched than has been estimated for meltwater drainage from Pine Island Glacier (-29 ‰, Hellmer et al., 1998), and deuterium excess within this facies is wide-ranging which likely reflects multiple water sources (Figure 4.5B). Therefore, we favor the interpretation that the freshest porewaters in Dm reflect mixing between subglacial discharge and ambient ocean water near the grounding line.

#### 4.4 Conclusions and future work

Isotope geochemistry of interstitial waters and sediments from the Amundsen Sea continental shelf record spatial and temporal variability in marine and glacial water sources and sedimentary processes. While stable water isotopes from meltwater plume deposits (facies S1 and S2) indicate sediments settled from a plume at a water depth that was sufficiently shallow so as to minimally influence bottom water, ratios of  $^{10}\text{Be}/^9\text{Be}$  are elevated in these sediments compared to those in diamicton facies (Dm and Ds), consistent with a subglacial source of meteoric beryllium to sediments (Figure 4.3). Grain size and sediment surface area may influence the concentration of meteoric beryllium (e.g., Wittmann et al., 2012), yet White et al. (2019) found no significant relationship between grain size and either  $^{10}\text{Be}/^9\text{Be}$  ratios or  $^{10}\text{Be}$  measurements in similar glaciomarine sediments from Prydz Bay, East Antarctica. Based on isotopic porewater and sediment chemistry, we suggest that the deposition of facies Dm was, at least in part, initiated by evacuation of meltwater at the grounding line and that interstitial waters, some of which are more isotopically depleted than Antarctic snowfall (Figure 4.5A; Masson-Delmotte et al., 2008), reflect mixing of subglacial and ambient ocean waters. These findings support the application of beryllium isotopes to determine sediment source and depositional setting (i.e., sub-ice shelf sediments or subglacial sediments mobilized within meltwater plumes), and identify clay-rich, ice-proximal diamictons formed through meltout or gravity flows at or near the grounding line as the most likely glaciogenic sediment to retain evidence of subglacial discharge in pore spaces (cf. Chapter 2, Lepp et al., 2022). Future work will integrate oceanographic measurements and stable water isotopes from cores collected beneath grounded ice to elucidate details of mixing (e.g., using a mixing model) during subglacial drainage needed to produce the depleted porewater isotopes observed in facies Dm. Additionally, we suggest that oxygen and hydrogen isotopes from porewater may help distinguish soft, deformable tills from grounding-line or ice-proximal diamicton. Porewater sampling in future polar coring expeditions should therefore target diamict recovered from ice-



proximal settings and landforms (e.g., grounding zone wedges, paleo-pinning points, meltwater fans) that are rich in clay.

**Table 4.1.** Geographic and bathymetric details for kasten cores (KC) used in this study. Multicore (MC), box core (BC) and CTD deployments with Niskin rosettes that collected bottom water samples, from which isotopes were used as reference, are denoted by an asterisk. IS = Ice Shelf. For more context on cores referenced in Lepp et al. (2022) cores, see Chapter 2 of this dissertation.

<b>Core ID</b>	<b>Latitude ° S</b>	<b>Longitude ° W</b>	<b>Water Depth <i>m</i></b>	<b>Bathymetric setting</b>	<b>Reference</b>
NBP19-02 KC04	74.94	106.87	469	Shallow basin on bathymetric high	Lepp et al., 2022
NBP19-02 KC15	74.87	106.33	545	Shallow basin west of Thwaites Eastern IS	Clark et al., 2023
NBP19-02 MC16*	74.87	106.33	549	Same site as NBP19-02 KC15	This study
NBP19-02 KC23	75.07	104.22	677	Thwaites Eastern IS corner	Lepp et al., 2022
NBP19-02 CTD76*	75.07	104.22	668	Same site as NBP19-02 KC23	This study
NBP20-02 KC20	74.97	100.60	686	Pine Island IS; lineated seafloor	This study
NBP20-02 KC26	75.02	100.75	805	Central Pine Island IS margin	This study
NBP20-02 BC27*	74.97	99.24	806	Same site as KC26	This study
NBP20-02 KC33	74.63	106.17	397	Bathymetric high, Thwaites Eastern IS	Lepp et al., 2022
NBP20-02 CTD27*	73.01	99.39	235	Same site as NBP120-02 KC33	This study
NBP22-02 KC06	74.09	112.26	930	Dotson IS East	This study
NBP22-02 KC15	73.97	113.85	683	Martin Peninsula	This study
NBP22-02 MC16*	73.97	113.85	699	Same site as NBP22-02 KC15	This study
NBP22-02 KC22	73.87	118.73	701	Getz B - West	This study
NBP22-02 KC29	74.12	115.19	808	Getz A	This study
NBP22-02 MC30*	74.12	115.19	807	Same site as NBP22-02 KC29	This study

**Table 4.2.** Range of diffusion coefficients for each sediment facies used in the porewater diffusion model. Mean porosity shows the average and standard error of mean porosity values for a given facies for all 10 sediment cores that sampled that facies. Note that only one core sampled stratified diamicton (NBP19-02 KC04) so this mean is reported with standard deviation.

<b>Facies</b>	<b>Mean Porosity</b>	<b>Diffusivity</b> <i>m<sup>2</sup> yr<sup>-1</sup></i>
Laminated silty clay - Sl	0.659 ± 0.020	2.508 ± 0.084 e <sup>-2</sup>
Bioturbated silty clay - Sb	0.635 ± 0.058	2.428 ± 0.212 e <sup>-2</sup>
Laminated sandy silt - Ssl	0.576 ± 0.046	2.213 ± 0.164 e <sup>-2</sup>
Massive diamicton - Dm	0.380 ± 0.031	1.565 ± 0.087 e <sup>-2</sup>
Stratified diamicton - Ds	0.498 ± 0.049	1.930 ± 0.002 e <sup>-2</sup>

SCILab Sample name	Sample name	Sample mass g	Native <sup>9</sup> Be μg	Mass of <sup>9</sup> Be Added* μg	Corr. for Background 10Be/ <sup>9</sup> Be	Corr. For Background 10Be/ <sup>9</sup> Be unc.	Native <sup>9</sup> Be atoms/g	<sup>9</sup> Be atoms unc.	[10Be]-bk	[10Be] unc	10Be/ <sup>9</sup> Be
23Ant1	NBP1902 KC04 20-22 cm	0.34498	0.00	0.20889	1.1547E-12	1.5272E-14	1.9479E+16	2.0387E+14	4.6721E+10	6.1792E+08	2.39856E-06
23Ant2	NBP1902 KC04 40-42 cm	0.35360	0.00	0.20510	3.1226E-13	5.7983E-15	1.4200E+16	2.8139E+14	1.2102E+10	2.2473E+08	8.52249E-07
23Ant3	NBP1902 KC04 80-82 cm	0.36316	0.00	0.20043	2.8077E-13	4.5070E-15	1.2279E+16	3.3679E+14	1.0354E+10	1.6621E+08	8.43224E-07
23Ant4	NBP1902 KC04 120-122 cm	0.33406	187.18	0.20902	1.8006E-13	3.3473E-15	1.2508E+16	2.0387E+14	7.5282E+09	1.3995E+08	6.01882E-07
23Ant5	NBP1902 KC04 200-202 cm	0.35289	227.03	0.20618	2.9532E-13	4.7299E-15	1.5170E+16	2.8139E+14	1.1529E+10	1.8465E+08	7.59995E-07
23Ant6	NBP1902 KC15 0-2 cm	0.35916	200.65	0.20360	7.1819E-13	1.1577E-14	1.3408E+16	3.3679E+14	2.7204E+10	4.3853E+08	2.02898E-06
23Ant7	NBP1902 KC15 90-92 cm	0.39534	351.46	0.20171	1.4371E-12	1.5810E-14	2.3485E+16	1.6467E+14	4.8996E+10	5.3902E+08	2.08626E-06
23Ant8	NBP1902 KC15 180-182 cm	0.33967	305.82	0.20872	2.5933E-12	2.3682E-14	2.0435E+16	1.9973E+14	1.0648E+11	9.7238E+08	5.21064E-06
23Ant9	NBP1902 KC15 290-292 cm	0.35465	354.77	0.20530	1.4573E-12	1.4577E-14	2.3706E+16	3.9339E+14	5.6370E+10	5.6383E+08	2.37787E-06
23Ant10	NBP1902 KC23 0-2 cm	0.41206	510.54	0.20308	1.8035E-14	1.8035E-14	3.4115E+16	1.2666E+14	6.4848E+10	5.931E+08	1.90088E-06
23Ant11	NBP1902 KC23 10-12 cm	0.39032	164.98	0.20130	2.2944E-13	4.7906E-15	1.1024E+16	4.2426E+14	7.9063E+09	1.6508E+08	7.17197E-07
23Ant12	NBP1902 KC23 180-182 cm	0.40973	302.38	0.20720	1.4997E-13	2.4068E-15	2.0205E+16	3.4588E+14	5.0674E+09	8.1323E+07	2.50794E-07
23Ant13	NBP2002 KC26 10-12 cm	0.38297	190.47	0.20606	1.3257E-12	1.4979E-14	1.2727E+16	2.6273E+14	4.7664E+10	5.3853E+08	3.74509E-06
23Ant14	NBP2002 KC26 30-32 cm	0.35671	114.15	0.20985	1.1682E-13	2.2626E-15	7.6275E+15	3.4403E+14	4.5916E+09	8.8934E+07	6.01979E-07
23Ant15	NBP2002 KC26 90-92 cm	0.34897	140.40	0.20451	1.5711E-13	2.5527E-15	9.3818E+15	2.6894E+14	6.1519E+09	9.9956E+07	6.55723E-07
23Ant16	NBP2202 KC06 5-6 cm	0.35810	245.30	0.20652	2.3287E-11	1.1055E-13	1.6391E+16	2.2174E+14	8.9739E+11	4.2600E+09	5.47487E-05
23Ant17	NBP2202 KC06 20-21 cm	0.39406	302.77	0.20022	3.2111E-12	6.2523E-14	2.0231E+16	3.1334E+14	1.0902E+11	2.1227E+09	5.38861E-06
23Ant18	NBP2202 KC06 80-81 cm	0.37560	376.35	0.20495	1.6180E-12	2.9251E-14	2.5148E+16	2.2253E+14	5.8996E+10	1.0665E+09	2.34595E-06
23Ant19	NBP2202 KC06 99-100 cm	0.35314	343.61	0.20145	2.2711E-12	2.5588E-14	2.2960E+16	2.0136E+14	8.6571E+10	9.7534E+08	3.7705E-06
23Ant20	NBP2202 KC06 119-120 cm	0.35108	319.71	0.20448	1.7810E-12	2.8194E-14	2.1363E+16	2.9793E+14	6.9313E+10	1.0973E+09	3.24448E-06
BLNK23-04	--	--	n.d.	0.20610	5.2289E-15	3.2490E-16	n.d.	n.d.	--	--	--
BLNK23-05	--	--	n.d.	0.20941	9.3873E-15	4.9647E-16	n.d.	n.d.	--	--	--

**Table 4.3.** Meteoric <sup>10</sup>Be and native <sup>9</sup>Be beryllium concentrations in Amundsen Sea sediment samples. Refer to Table 4.1 for sample coordinates and water depths. Unc. = uncertainty.

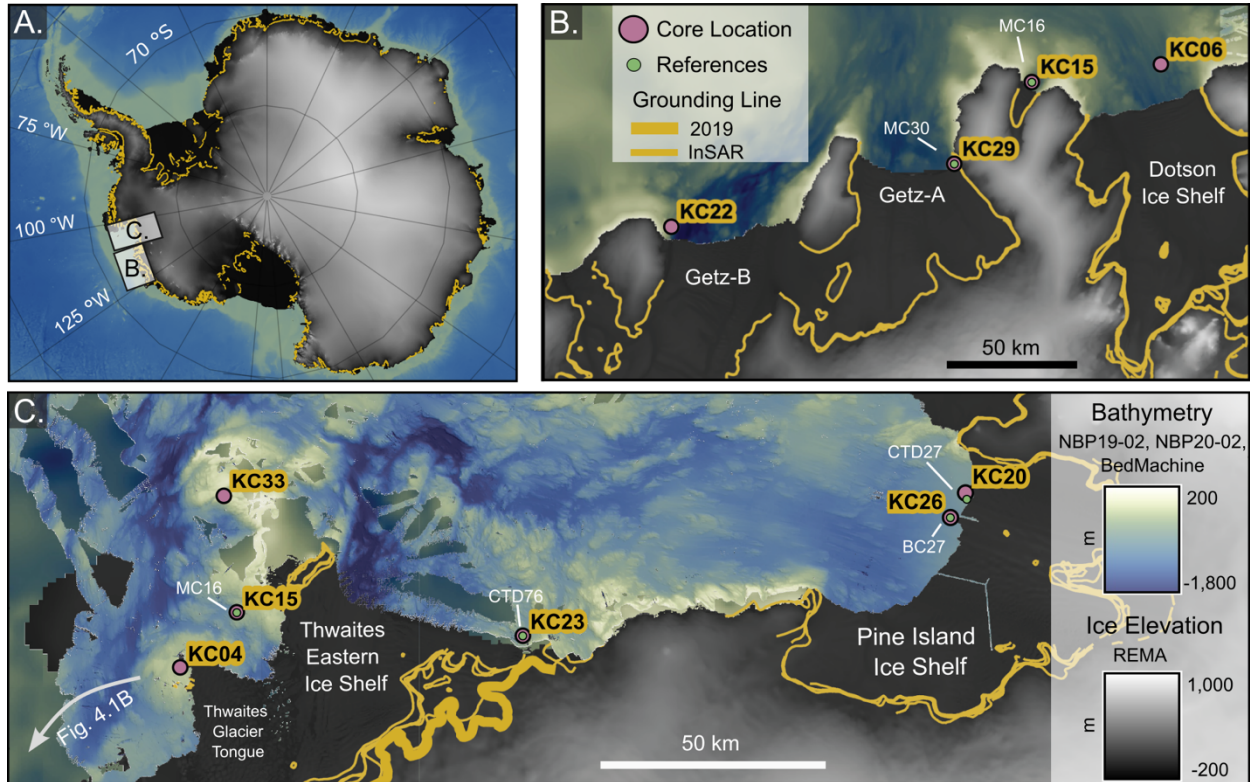


**Figure 4.1.** Location of sediment cores from the Amundsen Sea sector of West Antarctica (A) for which porewater diffusion profiles are examined. (B) Sediment cores collected from ice-marginal locations offshore the Dotson and Getz ice shelves. (C) Sediment cores from inner Pine Island Bay offshore of the Pine Island and Thwaites ice shelves. Small green circles denote locations where reference waters used in isotopic diffusion models were collected (Table 4.1). Grounding line data are from Milillo et al. (2019) and Rignot et al. (2011). BedMachine bathymetry is from Morlighem et al. (2020) and ice surface elevation is from the Reference Elevation Model of Antarctica (REMA; Howat et al., 2019).

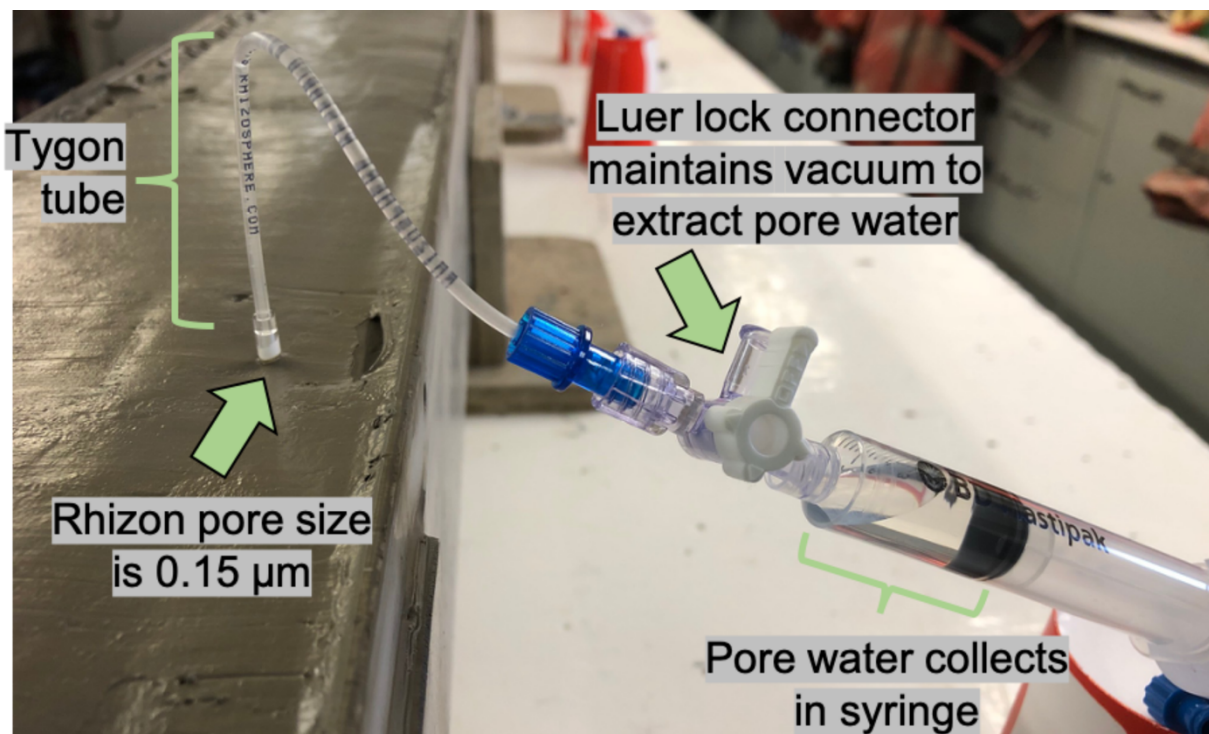


**Figure 4.2.** Sampling image of sediment porewater extraction using a Rhizon filter. A minimum of 2 mL of water was collected from each interval for stable water isotope analysis.

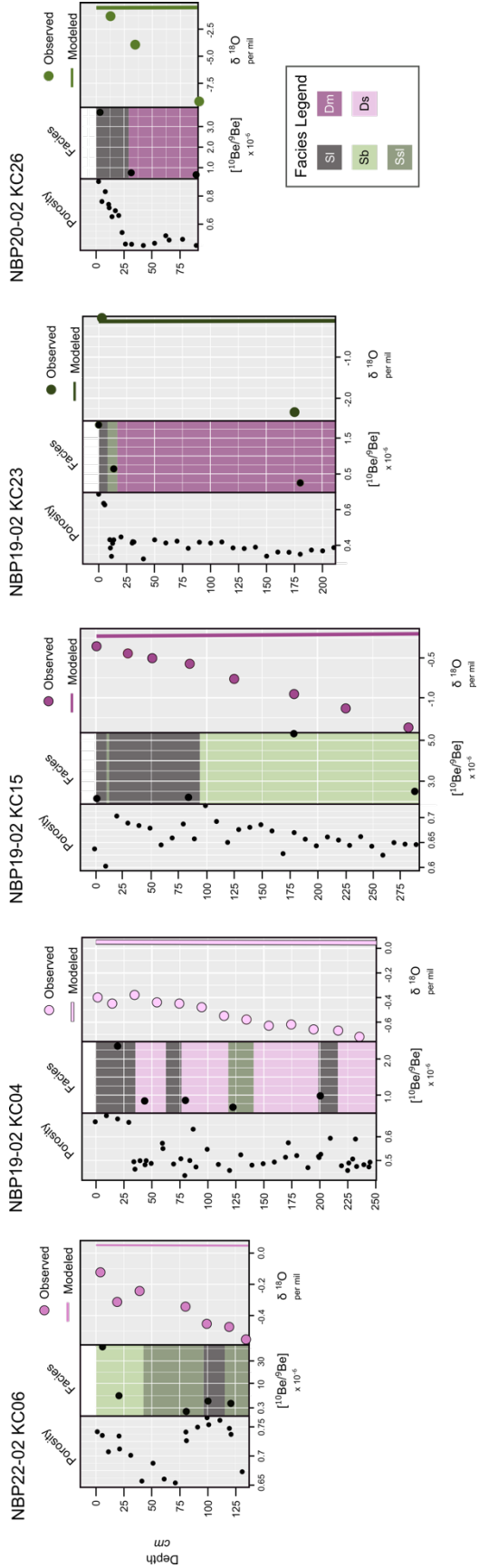


**Figure 4.3.** Downcore porosity, facies assignments,  $^{10}\text{Be}/^9\text{Be}$  ratios, and both modeled (solid line) and measured (circle) concentrations of  $\delta^{18}\text{O}$  (‰) for select sediment cores. Plots are arranged from western (left) to eastern (right) core sites Sl: laminated silty clay; Sb: bioturbated silty clay; Ssl: laminated sandy silts; Dm: massive diamicton; Ds: stratified diamicton.

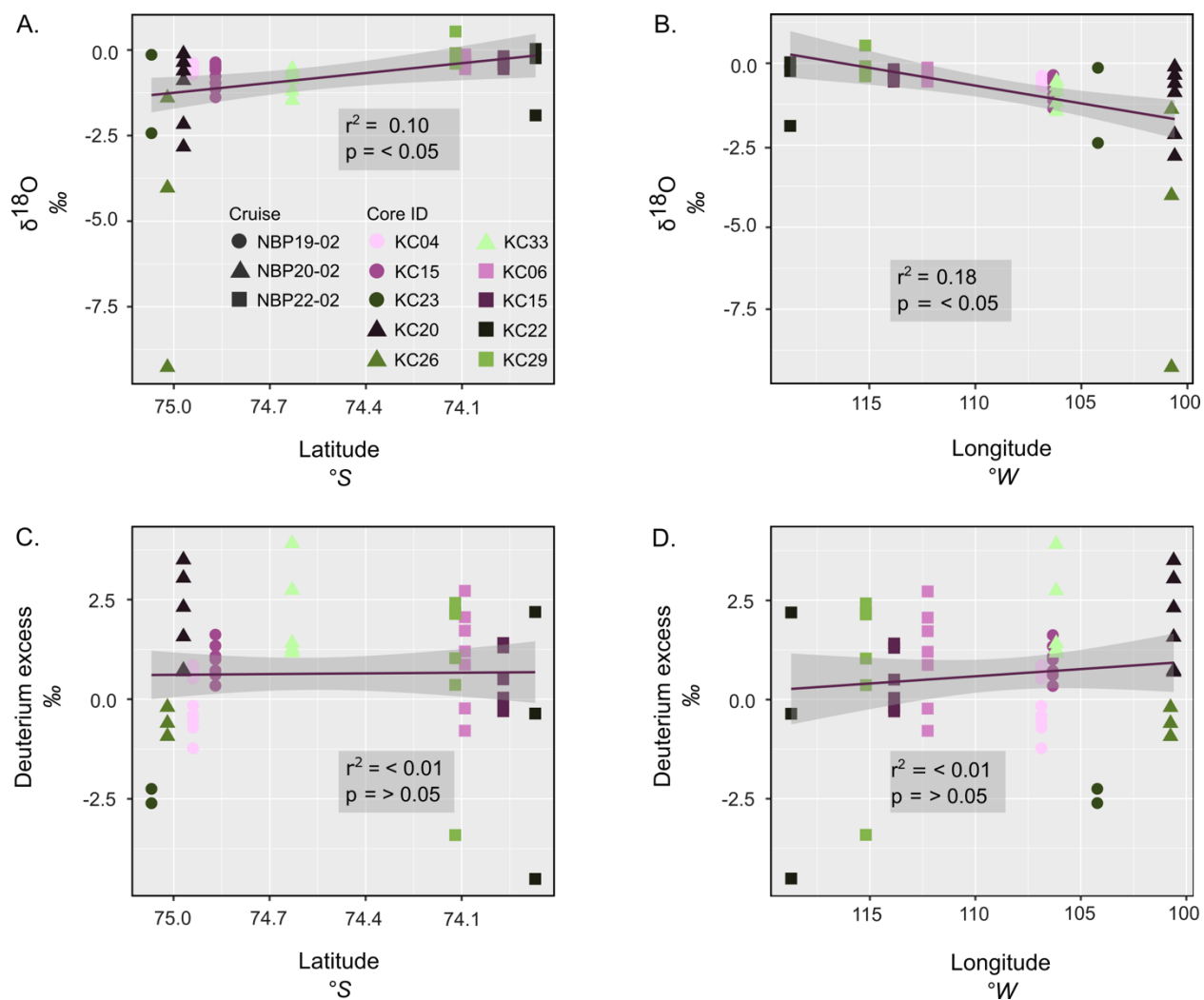


**Figure 4.4.** Spatial distribution of oxygen isotope ratio (A-B) and deuterium excess (C-D). Purple lines indicate linear regressions between each pair of variables with standard error bounds shaded in gray, and the coefficient of determination and  $p$  values for each pair are shown in the dark gray boxes. Cruise and core symbology is provided in (A).



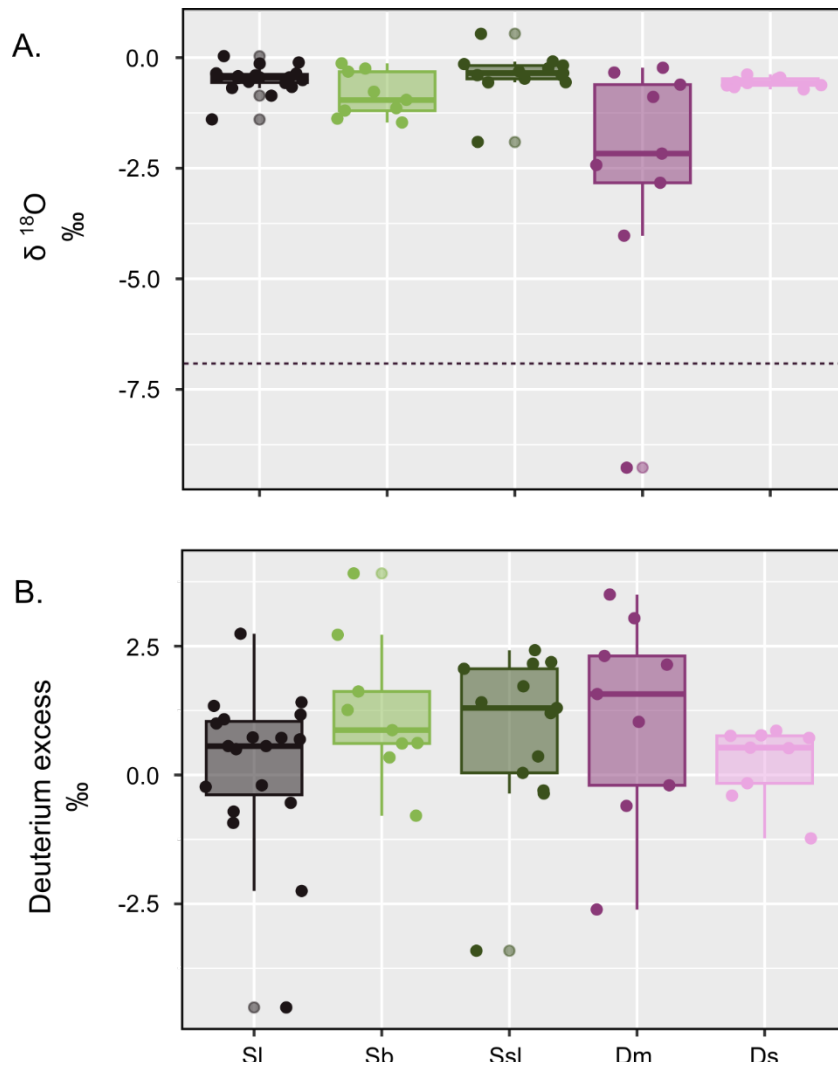


**Figure 4.5.** Box and whisker plots showing the range for all measured (A)  $\delta^{18}\text{O}$  and (B) deuterium excess colored by facies. Dashed line represents the most enriched end-member for Antarctic snow from a database with isotopic measurements from over 1,100 locations (Masson-Delmotte et al., 2008). Sl: laminated silty clay; Sb: bioturbated silty clay; Ssl: laminated sandy silts; Dm: massive diamicton; Ds: stratified diamicton.

## Chapter 5: Concluding Remarks

### *5.1 Dissertation summary*

This dissertation presents novel findings from marine sediment archives that advance site-specific and process-based understanding of subglacial hydrology, sediment transport, and ice-marginal response to subglacial meltwater discharge through time and space. Our ability to connect details of subglacial plumbing systems to the sedimentary signatures they leave behind is necessary for a holistic understanding of glacial systems and the controls on their stability. Collectively, the studies comprising this dissertation expand the toolkit with which glaciomarine sediment records can be assessed and linked to subglacial hydrologic processes.

In Chapter 2, sedimentological and geochemical measurements indicate that the vulnerable Thwaites Glacier has a spatially variable subglacial plumbing network upstream, and that this plumbing network has been a persistent delivery system of sediment into the eastern Amundsen Sea throughout the Holocene. The geographic distribution and stratigraphic character of meltwater plume deposits is consistent with predicted locations and relative, estimated fluxes of channelized drainage to the grounding line (Le Brocq et al., 2013; Hager et al., 2022). Furthermore, recent observations from the contemporary grounding zone of eastern Thwaites Glacier record a low-magnitude, pulsed outflow of meltwater into the ice-shelf cavity from a subglacial source (Davis et al., 2023); such a “leaky faucet” drainage style is recorded by meltwater endmember cores offshore eastern Thwaites, indicating that the observation from Davis et al. (2023) is likely representative of long-lived, steady-state conditions of subglacial hydrology that do not appear to be connected with Holocene ice-shelf disintegration. Conversely, drainage emerging beneath the Thwaites Glacier Tongue to the west is found to have been active prior to and following unpinning of the ice tongue from a bathymetric high between 2011 and 2019. Furthermore, stratigraphic analysis suggests the relative magnitude of drainage events has increased in recent centuries compared to the past several millennia (Figures 2.6A, 2.8C). Combined with the presence of deep bathymetric troughs that actively route warm circumpolar deep water to the grounding zone, the sedimentary evidence presented in Chapter 2 strongly suggest that subglacial discharge has, and likely will continue to, enhanced localized melting of the grounding line and ice shelf base of Thwaites Glacier and must be accounted for in models considering ice-ocean feedback.

The ubiquitous grain-size distribution of meltwater plume deposits sampled offshore of several Antarctic and Greenland glaciers suggests widespread subglacial sedimentary and/or hydrological processes, and Chapter 3 provides the first inter-system comparison with the aim of elucidating those processes. Grain shape and microtexture (considered together as grain micromorphology) are examined for their proven abilities to record details of sediment transport and grain-size production in myriad depositional environments (e.g., Oakey et al., 2005; Campaña et al., 2016; Crompton et al., 2019; van Hateren et al., 2020). Three-quarters of the nearly ten-thousand grains imaged for quantitative grain-shape analysis fall within one-quarter of possible grain shapes, providing support for efficient, widespread subglacial sediment transport at catchment scales (Figure 3.5). In the first microtexture analysis conducted on silt-sized quartz grains, both meltwater plume deposits and tills are found to exhibit mechanical textures indicative of glacial abrasion and sustained stress in comparable amounts, confirming that the grain-size production of the ubiquitous meltwater silt is a glacial, rather than a hydrological process. Alteration in grain shape between subglacial tills and meltwater plume deposits is the

most significant in glacial systems for which supraglacial melt is an important contribution to the subglacial hydrological budget, and for which high-magnitude drainage events are inferred from other marine geologic records. Chapter 3 establishes new linkages between grain-scale characteristics of sediments deposited by subglacial meltwater and past subglacial hydrological organization and conditions (Lepp et al., *preprint*). More broadly, these findings indicate that grain shape could be a useful metric with which to assess whether surface melting contributed substantially to the subglacial hydrological budget of Antarctic glaciers during past warm periods (e.g., Anderson et al., 2011; Passchier et al., 2011; Bart and DeSantis, 2012). Additionally, a micromorphological approach can support the quantification of differential impacts of shearing and stress on grain micromorphology in experimental settings (e.g., Hansen and Zoet, 2022; Zoet et al., 2023), which is useful in estimating subglacial sediment production and fluxes.

Sediment porewater geochemistry in marine and glaciomarine sediments can retain ionic and isotopic evidence for sedimentary processes and climatic conditions of the past (Remenda et al., 1994; Adkins et al., 2002; Kuhn et al., 2017; Kumar et al., 2020; Neuhaus et al., 2021; Herbert et al., 2023). Using a suite of ten glaciomarine sediment cores from the eastern Amundsen Sea sector of West Antarctica, we consider whether stable oxygen and hydrogen isotopes of interstitial waters are an appropriate proxy to study subglacial meltwater drainage events since the LGM. Porewaters sampled from laminated and bioturbated silty clay, sedimentary facies reflective of suspension settling from subglacial meltwater plumes, are inconsistent with a fresh, glacial source, but elevated ratios of  $^{10}\text{Be}/^{9}\text{Be}$  in these sediments compared to ice-proximal diamicton facies (Dm and Ds) are consistent with a subglacial source of meteoric beryllium to sediments (Figure 4.3). Conversely, the most isotopically-depleted porewaters are sampled from massive diamicton, implying that rapid sedimentation in grounding-line proximal sites can retain interstitial water with a composition of mixed marine and subglacial endmembers. These isotopic ratios are valuable data to inform mixing models needed to constrain likely fluxes of freshwater, and sediment, into ice-shelf cavities and beyond. This work assesses the suitability of different isotope proxies based on sediment properties and depositional environments, and suggests that stable water isotopes in porewater may be useful in separating ice-proximal diamicton from subglacial till, which is a longstanding challenge in glaciomarine sedimentology (cf. Halberstadt et al., 2018; Prothro et al., 2018).

The works within this dissertation have implications for the interactions between subglacial drainage and melting within ice-shelf cavities, subglacial sediment transport processes, and realistic models of modern and paleo-subglacial hydrological organization and activity. Methods and findings presented here are relevant to a range of disciplines including paleoclimatology, contemporary glacial hydrology, glacial (marine) geology, and polar oceanography.

## 5.2 *Suggestions for future research directions*

Subglacial hydrology impacts ice sheet mass balance through modulating rates of ice discharge into the ocean, impacting stability of ice margins and floating ice shelves, and can have far-reaching impacts as buoyant meltwater plumes transport freshwater and nutrients into the ocean. We lack a comprehensive understanding of this vital component of glaciology, in particular its evolution on timescales exceeding satellite observations. It remains unclear how subglacial hydrology may (continue to) affect contemporary marine-terminating glaciers in a warming world, and the framework within which we consider subglacial hydrology beneath the

Antarctic Ice Sheet will need to shift dramatically should surface melting become a widespread and significant contributor to the subglacial hydrological budget. Research that elucidates glacial sensitivity and response to subglacial discharge over centuries to millennia is therefore necessary to provide critical context for ongoing changes of marine-terminating glaciers.

While many settings on the Antarctic continental shelf remain under-surveyed and higher spatial resolution of sediment core sampling would be valuable, this dissertation demonstrates the utility of underused, emerging, and nondestructive methods that can be applied to gain new insights from legacy cores. For example, computed tomography (CT) scanning is increasingly used for sedimentary applications and supported by institutional partnerships between medical and earth science departments. In addition to the work presented in Chapter 2 (Lepp et al., 2022), CT imagery has contributed to reconstructing post-LGM meltwater drainage activity for glaciers in northern Greenland (Reilly et al., 2019; O'Regan et al., 2021; Davies et al., 2022; Jennings et al., 2022) and within the modern Mercer Subglacial Lake of Antarctica (Siegfried et al., 2023). Automated approaches for traditional sedimentological analyses, like counting of varves, laminae, and ice-rafted debris, are emerging using CT imagery (e.g., McDonald et al., 2022). Thus, stratigraphic details of glaciomarine sediments as revealed through CT or other density-based imaging techniques have the potential to support, or challenge, existing interpretations of depositional environments and processes, including those related to subglacial meltwater discharge.

The geometry and migration of plumes has important implications for the impacts of subglacial discharge on regional oceanographic circulation (i.e., within fjords, embayments, etc.) and sediment distribution. Recent modeling studies show great promise in reconstructing and projecting realistic plume trajectories that incorporate observed oceanographic, glaciologic, and atmospheric conditions (Gwyther et al., 2023), but very few have integrated the temporal perspective preserved by marine sediments (e.g., Dowdeswell et al., 2015). In Antarctica, a notable challenge of plume modeling remains the obscuration of plume initiation and dispersal by floating ice shelves and ice canopies. Interdisciplinary studies that integrate bathymetric and sedimentologic details of subglacial discharge with geochronology as available into existing modeling frameworks for plume migration (Mugford and Dowdeswell, 2011) can help reduce knowledge gaps and should be of a high scientific priority. Similarly, high-resolution observations of plume initiation and development, while limited, suggest that true plume dynamics are more complex than implied by buoyant plume theory (Jenkins, 2011; Jackson et al., 2017). Research focusing on data-model integration for subglacial water drainage and convective heat transfer within ice-shelf cavities will be incredibly valuable for predictive models of marine-terminating glaciers in the Antarctic where warm CDW is shown to reach grounding zones. Results from Chapter 4 demonstrate that stable water isotopes in clay-rich, ice-proximal sediments can be appropriate tools to untangle details of paleo-drainage events using the sediment record. If coupled with numerical models, these data can inform estimates of subglacial discharge and refine quantified freshwater inputs to polar marine environments (e.g., Adusumilli et al., 2020).

The stratigraphic sequence of subglacial till overlain by meltwater plume deposits and capped with biogenic-rich open marine sediments is described in sediment cores collected offshore several glacial systems in the Antarctic. The implication is that intensive subglacial drainage is a precursor to significant grounding-zone retreat events and, in contemporary systems, may be a 'canary in the coal mine' for impending glacial instability (e.g., Witus et al., 2014). However, our findings from Chapter 2 present a more complex story, whereby the

Thwaites Eastern Ice Shelf and grounding zone migrated landward relatively gradually without ice-shelf collapse or major changes to the volume of subglacial drainage. While this gradual retreat may have been connected with rerouting of subglacial drainage pathways, marine sediments record a different story for the Thwaites Glacier Tongue and the grounding line of western Thwaites, demonstrating that multiple styles and magnitudes of subglacial drainage can co-exist within a single glacial catchment and, importantly, may be associated with distinct behaviors of ice flow. These new sedimentary archives provide context to existing evidence for varied and simultaneous styles of paleo-subglacial drainage that are preserved in the landform and bathymetric records (meltwater corridors, e.g., Simkins et al., 2021). Overall, these results imply we should exercise caution when widely prescribing subglacial conditions, including organization of subglacial plumbing and bed conditions, in glaciohydraulic models, but also strongly suggest the role of subglacial discharge be incorporated into models predicting grounding line and ice shelf behavior.

## Appendix A2.

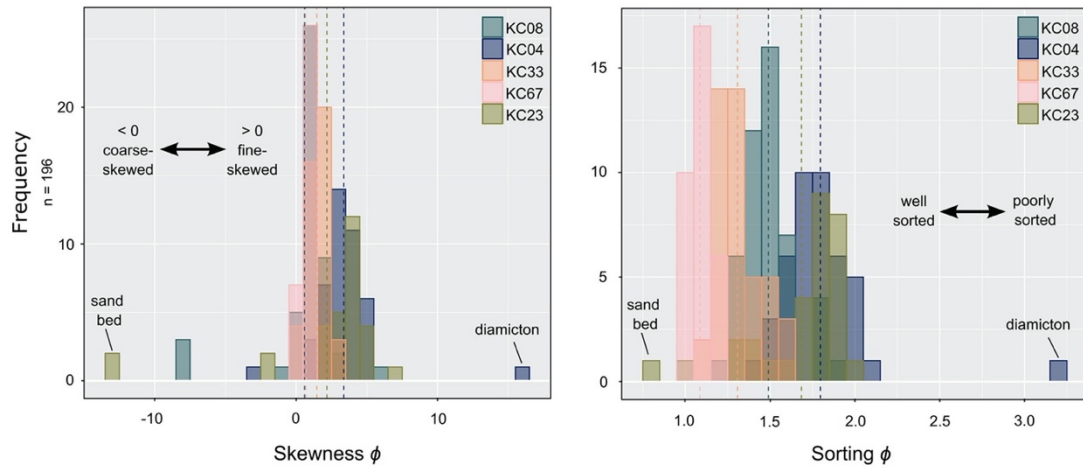


**Figure A2.1.** Histograms showing skewness and sorting (i.e., standard deviation) statistics for all grain size samples (n=196). Note range of axes differ between plots. The majority of samples are fine-skewed, while KC33 and KC67 distributions are closest to symmetrical (skewness=0). Cores KC33 and KC67 are the most well-sorted, with KC67 showing little variation in sorting downcore. Ice-shelf proximal cores KC04 and KC23 show the poorest sorting, consistent with diamicton and glacially-influenced deposits.

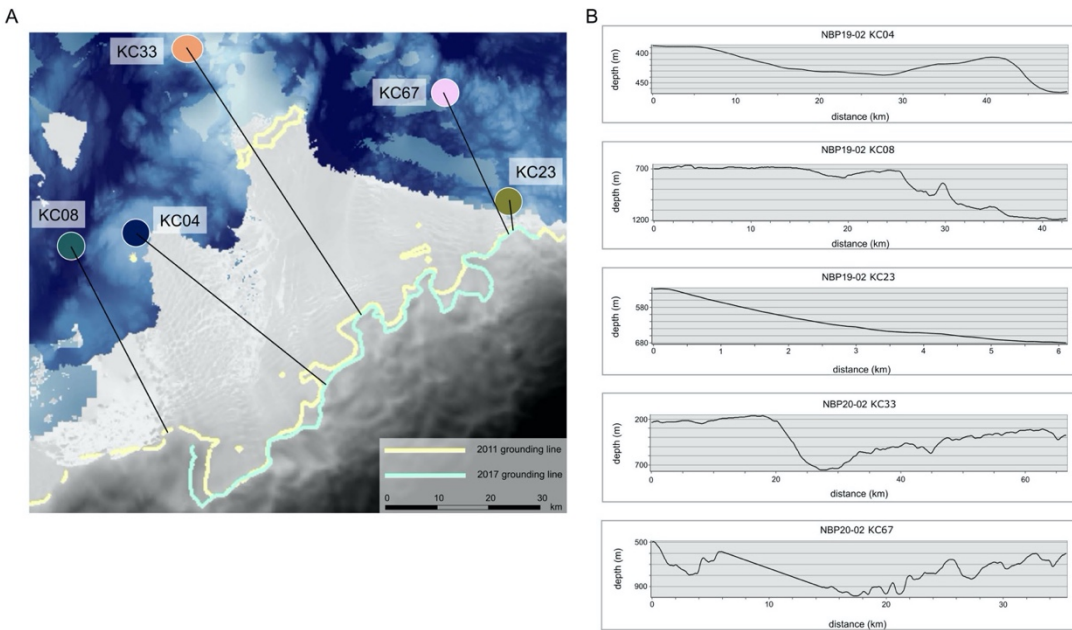
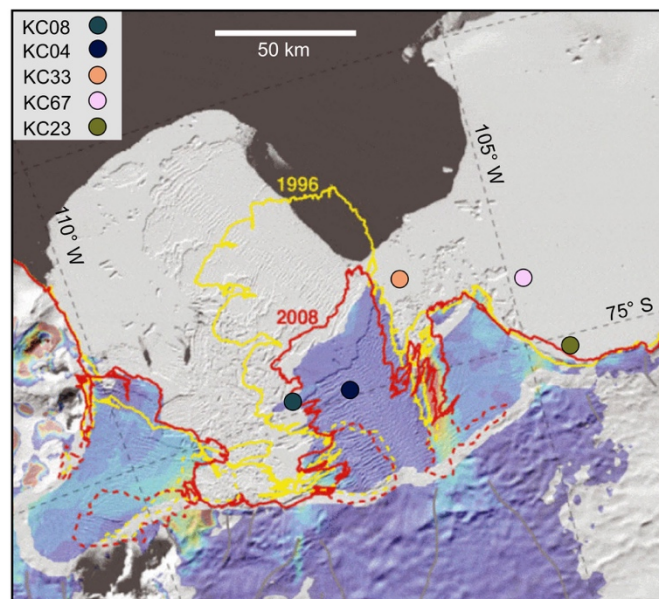


**Figure A2.2.** Distance of contemporary plume migration estimated by (A) drawing transects from most proximal, and most recent (as is available), grounding line position to each core site. (B) Projections of horizontal bathymetric profiles of transects. Grounding line position is on the left and core location on the right. Transects were mapped using the 3D Analyst toolbox in ArcGIS. Note the difference in axis values between transects. Grounding line data are from Rignot et al. (2011) and Milillo et al. (2019). Floating ice is from the Reference Elevation Map of Antarctica (REMA; Howat et al., 2019).

**Figure A2.3.** Location of core sites georeferenced onto a map of Thwaites Glacier ice-shelf and ice-tongue extents in 1996 (yellow) and 2008 (red). Adapted from MacGregor et al. (2012).



## Appendix A4.

**Table A4.1.** Instrumental operating parameters for inductively-coupled plasma mass spectrometry conducted at Stanford University. The instrument was operated in single quad mode with He as a reaction gas.

<b>He gas mode</b>		
<b>Acquisition Parameters</b>	Scan Mode	Single quad
	Integration time per mass (s)	0.15
<b>Plasma</b>	RF power (W)	1550
	Sampling depth (mm)	7.0
	Nebulizer gas (L/min)	0.70
<b>Cell</b>	He gas flow rates (mL/min)	1.6
	KED (V)	3.0



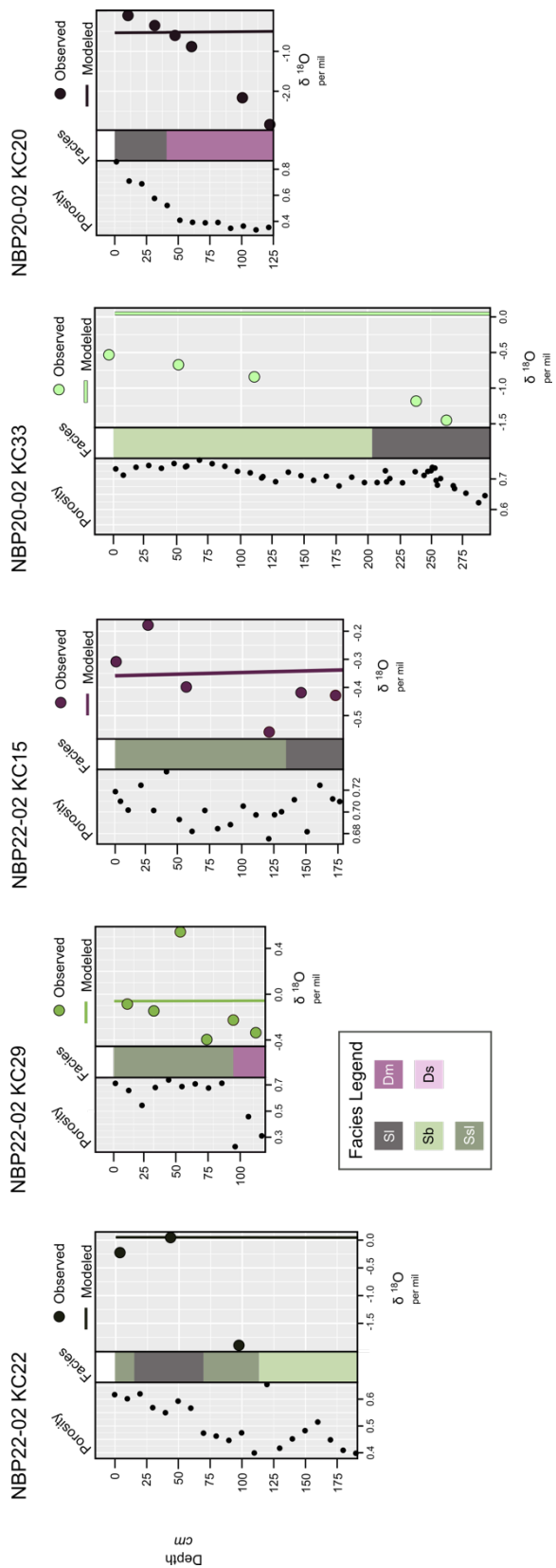
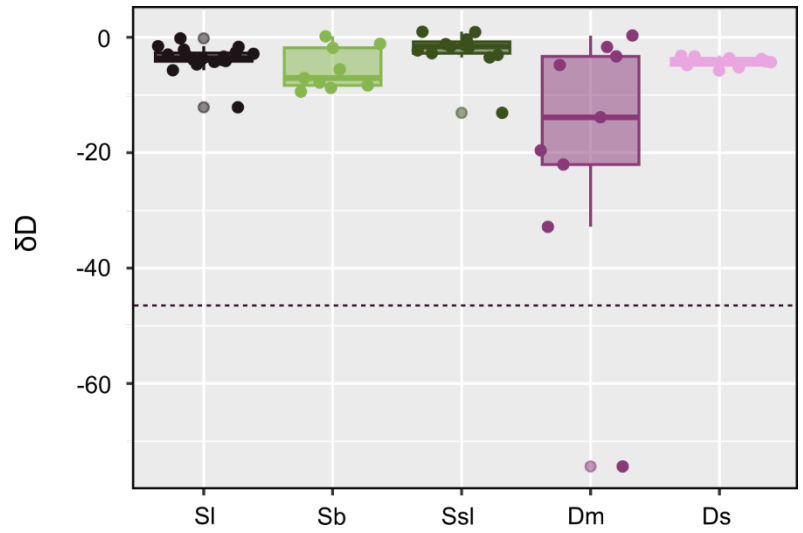


**Figure A4.1.** Downcore porosity, facies assignments, and modeled (solid line) and measured (circle)  $\delta^{18}\text{O}$  concentrations for sediment cores without beryllium measurements. Plots are arranged from western (left) to eastern (right) core sites. Sl: laminated silty clay; Sb: bioturbated silty clay; Ssl: laminated sandy silts; Dm: massive diamicton; Ds: stratified diamicton.

**Figure A4.2.** Box and whisker plots showing the range of  $\delta D$  for porewater samples colored by facies. Dashed line represents the most enriched end-member for Antarctic snow from a database with isotopic measurements from over 1,100 locations (Masson-Delmotte et al., 2008). Sl: laminated silty clay; Sb: bioturbated silty clay; Ssl: laminated sandy silts; Dm: massive diamicton; Ds: stratified diamicton.



## References

- Adkins, J.F., McIntyre, K., and Schrag, D.P.: The salinity, temperature, and  $\delta^{18}\text{O}$  of the glacial deep ocean, *Science*, 298, 1769-1773, doi: 10.1126/science.1076252, 2002.
- Adusumilli, S., Fricker, H.A., Medley, B., Padman, L., and Siegfried, M.R.: Interannual variations in meltwater input to the Southern Ocean from Antarctic ice shelves, *Nat. Geosci.*, 13, 616-620, doi: 10.1038/s41561-020-0616-z, 2020.
- Alley, K.E., Scambos, T.A., Siegfried, M.R., and Fricker, H.A.: Impacts of warm water on Antarctic ice shelf stability through basal channel formation, *Nat. Geosci.*, 9, 290-294, doi: 10.1038/ngeo2675, 2016.
- Alley, K.E., Wild, C.T., Luckman, A., Scambos, T.A., Truffer, M., Pettit, E.C., Muto, A., Wallin, B., Klinger, M., Sutterley, T., Child, S.R., Hulen, C., Lenaerts, J.T.M., Maclennan, M., Keenan, E., and Dunmire, D.: Two decades of dynamic change and progressive destabilization on the Thwaites Eastern Ice Shelf, *Cryosphere*, 15, 5187-5203. doi: 10.5194/tc-15-5187-2021, 2021.
- Alley, R.B., Blankenship, D.D., Bentley, C.R., and Rooney, S.T.: Deformation of till beneath ice stream B, West Antarctica, *Nature*, 322, 57–59, doi: 10.1038/322057a0, 1986.
- Alley, R.B., Cuffey, K.M., Evenson, E.B., Strasser, J.C., Lawson, D.E., and Larson, G.J.: How glaciers entrain and transport basal sediments: physical constraints, *Quaternary Sci. Rev.*, 16, 1017-1038, doi: 10.1016/S0277-3791(97)00034-6, 1997.
- Alley, R.B., Cuffey, K.M., and Zoet, L.K.: Glacial erosion: status and outlook, *Ann. Glaciol.*, 60, 1-13, doi: 10.1017/aog.2019.38, 2019.
- Alley, R.B., Holschuh, N., MacAyeal, D.R., Parizek, B.R., Zoet, L., Riverman, K., Muto, A., Christianson, K., Clyne, E., Anandakrishnan, S., Stevens, N. and the GHOST Collaboration: Bedforms of Thwaites Glacier, West Antarctica: Character and Origin, *J. Geophys. Res.-Earth*, 126:12, doi:10.1029/2021JF006339, 2021.
- Anderson, J.B.: *Antarctic Marine Geology*. New York: Cambridge University Press, Cambridge, 1999.
- Anderson, J.B. and Fretwell, L.O.: Geomorphology of the onset area of a paleo-ice stream, Marguerite Bay, Antarctic Peninsula, *Earth Surf. Proc. Land.*, 33, 503-512, doi: 10.1002/esp.1662, 2008.
- Anderson, J.B., Warny, S., Askin, R.A., Wellner, J.S., Bohaty, S.M., Kirshner, A.E., Livsey, D.N., Simms, A.R., Smith, T.R., Ehrmann, W., Lawver, L.A., Barbeau, D., Wise, S.W., Kulhanek, D.K., Weaver, F.M., and Majewski, W.: Progressive Cenozoic cooling and the demise of Antarctica's last refugium, *P. Natl. Acad. Sci. USA*, 108, 11356-11360, doi: 10.1073/pnas.10104885108, 2011.
- Andreassen, K. and Winsborrow, M.: Signature of ice streaming in Bjørnøyrenna, Polar North Atlantic, through the Pleistocene and implications for ice-stream dynamics, *Ann. Glaciol.*, 50, 17-26, doi: 10.3189/172756409789624238, 2009.
- Bart, P.J. and DeSantis, L.: Glacial intensification during the Neogene: A review of seismic stratigraphic evidence from the Ross Sea, Antarctica, *Continental Shelf, Oceanography*, 25, 166-183, <https://www.jstor.org/stable/24861411>, 2012.

- Bart, P.J., Krogmeier, B.J., Bart, M.P., and Tulaczyk, S.: The paradox of a long grounding during West Antarctic Ice Sheet retreat in Ross Sea, *Sci. Rep.*, 7, 1262, doi: 10.1038/s41598-017-01329-8, 2017.
- Bear, J.: *Dynamics of fluids in porous media*, Dover, New York, 1988.
- Begeman, C.B., Tulaczyk, S.M., Marsh, O.J., Mikucki, J.A., Stanton, T.P., Hodson, T.O., Siegfried, M.R., Powell, R.D., Christianson, K., and King, M.A.: Ocean stratification and low melt rates at the Ross Ice Shelf grounding zone, *J. Geophys. Res.*, 123, 7438-7452, doi: 10.1029/2019JC013987, 2018.
- Behrens, B.C., Yokoyama, Y., Miyairi, Y., Sproson, A.D., Yamane, M., Jimenez-Espejo, F.J., McKay, R.M., Johnson, K.M., Escutia, C., and Dunbar, R.B.: Beryllium isotope variations recorded in the Adlie Basin, East Antarctica reflect Holocene changes in ice dynamics, productivity, and scavenging efficiency, *Quaternary Sci. Adv.*, 7, 100054, doi: 10.1016/j.qsa.2022.100054, 2022.
- Bell, R.E., Studinger, M., Shuman, C.A., Fahnestock, M.A., and Joughin, I.: Large subglacial lakes in East Antarctica at the onset of fast-flowing ice streams, *Nature*, 445, 904-907, doi: 10.1038/nature05554, 2007.
- Bell, R.E., Banwell, A.F., Trusel, L.D., and Kingslake, J.: Antarctic surface hydrology and impacts on ice-sheet mass balance, *Nat. Clim. Change*, 8, 1044-1052, doi: 10.1038/s41558-018-0326-3, 2018.
- Bentley, M.J., Johnson, J.S., Hodgson, D.A., Dunai, T., Freeman, S.P.H.T., and Ó Cofaigh, C.: Rapid deglaciation of Marguerite Bay, western Antarctic Peninsula in the Early Holocene, *Quaternary Sci. Rev.*, 30, 3338-3349, doi: 10.1016/j.quascirev.2011.09.002, 2011.
- Biddle, L. C., Loose, B., and Heywood, K.J.: Upper ocean distribution of glacial meltwater in the Amundsen Sea, Antarctica. *J. Geophys. Res-Oceans*, 124, 6854-6870, doi: 10.1029/2019JC015133, 2019.
- Blackman, D.K., Von Herzen, R.P., and Lawver, L.A.: Heat flow and tectonics in the Western Ross Sea, Antarctica, Vol. 5B9, 179-189, Earth Science Series, Circum-Pacific Council for Energy and Mineral Resources, 1987.
- Blake, G.R.: Particle density. In: Chesworth, W. (eds) *Encyclopedia of Soil Science*, *Encyclopedia of Earth Sciences Series*, Springer, Dordrecht, doi: 10.1007/978-1-4020-3995-9\_406, 2008.
- Borstad, C., Khazendar, A., Larour, E., Morlighem, M., Rignot, E., Schodlok, M.P., and Seroussi, H.: A damage mechanics assessment of the Larsen B ice shelf prior to collapse: Toward a physically-based calving law, *Geophys. Res. Lett.*, 39, L18502, doi: 10.1029/2012GL053317, 2012.
- Borstad, C., McGrath, D., and Pope, A.: Fracture propagation and stability of ice shelves governed by ice shelf heterogeneity, *Geophys. Res. Lett.*, 44, 4186-4194, doi: 10.1002/2017GL072648, 2017.
- Boudreau, B.P.: The diffusive tortuosity of fine-grained unlithified sediments, *Geochim. Cosmochim. Ac.*, 60, 3139-3142, doi: 10.1016/0016-7037(96)00158-5-, 1996.
- Boulton, G.S., Dobbie, K.E., and Zatsepin, S.: Sediment deformation beneath glaciers and its coupling to the subglacial hydraulic system, *Quatern. Int.*, 86, 3-28, doi: 10.1016/S1040-6182(01)00048-9, 2001.

- Bowling, J.S., Livingstone, S.J., Sole, A.J., and Chu, W.: Distribution and dynamics of Greenland subglacial lakes, *Nat. Commun.*, 10, 2810, doi: 10.1038/s41467-019-10821-w, 2019.
- Bjarnadóttir, L.R., Winsborrow, M.C.M., and Andreassen, K.: Deglaciation of the central Barents Sea, *Quaternary Sci. Rev.*, 92, 208-226, doi: 10.1016/j.quascirev.2013.09.012, 2014.
- Campaña, I., Benito-Calvo, A., Pérez-González, Bermúdez de Castro, J.M., and Carbonell, E.: Assessing automated image analysis of sand grain shape to identify sedimentary facies, Gran Dolina archaeological site (Burgos, Spain), *Sed. Geol.*, 346, 72-83, doi: 10.1016/j.sedgeo.2016.09.010, 2016.
- Carter, S.P., Fricker, H.A., Blankenship, D.D., Johnson, J.V., Lipscomb, W.H., Price, S.F., and Young, D.A.: Modeling 5 years of subglacial lake activity in the MacAyeal Ice Stream (Antarctica) catchment through assimilation of ICESat laser altimetry, *Ann. Glaciol.*, 57, 1098-1112, doi: 10.3189/002214311798843421, 2011.
- Carter, S.P., and Fricker, H.A.: The supply of subglacial meltwater to the grounding line of the Siple Coast, West Antarctica, *Ann. Glaciol.*, 53, 267-280, doi: 10.3189/2012AoG60A119, 2012.
- Carter, S. P., Fricker, H.A., and Siegfried, M.R.: Evidence of rapid subglacial water piracy under Whillans Ice Stream, West Antarctica, *J. Glaciol.*, 59, 1147-1162, doi: 10.3189/2013JoG13J085, 2013.
- Cederstrøm, J.M., van der Bilt, W.G.M., Støren, E.W.N., and Rutledal, S.: Semi-automatic ice-rafted debris quantification with computed tomography, *Paleoceanography and Paleoclimatology*, 36, e2021PA004293, doi: 10.1029/2021PA004293, 2021.
- Chandler, D.M., Wadham, J.L., Nienow, P.W., Doyle, S.H., Tedstone, A.J., Telling, J., Hawkings, J., Alcock, J.D., Linhoff, B., and Hubbard, A.: Rapid development and persistence of efficient subglacial drainage under 900 m-thick ice in Greenland, *Earth Plan. Sci. Lett.*, 566, 116982, doi: 10.1016/j.epsl.2021.116982, 2021.
- Charpentier, I., Staszyc, A.B., Wellner, J.S., and Alejandro, V.: Quantifying grain shape with MorpheoLV: a case study using Holocene glacial marine sediments, *EPJ Web of Conferences*. Vol. 140. EDP Sciences, doi:10.1051/epjconf/201714014003, 2017.
- Christoffersen, P., Tulaczyk, S., and Behar, A.: Basal ice sequences in Antarctic ice stream: exposure of past hydrologic conditions and a principal mode of sediment transfer, *J. Geophys. Res.-Earth*, 115(F3), doi: 10.1029/2009JF001430, 2010.
- Christoffersen, P., Bougamont, M., Carter, S.P., Fricker, H.A., and Tulaczyk, S.: Significant groundwater contribution to Antarctic ice streams hydrologic budget, *Geophys. Res. Lett.*, 41, 2003-2010, doi: 10.1002/2014GL059250, 2014.
- Chu, V.W., Smith, L.C., Rennermalm, A.K., Forster, R.R., Box, J.E., and Reeh, N.: Sediment plume response to surface melting and supraglacial lake drainages on the Greenland ice sheet, *J. Glaciol.*, 55, 1072-1082, doi: 10.3189/002214309790794904, 2009.
- Chu, V.W., Smith, L.C., Rennermalm, A.K., Forster, R.R., and Box, J.E.: Hydrologic controls on coastal suspended sediment plumes around the Greenland ice sheet, *Cryosphere*, 6, 1-19, doi: 10.5194/tc-6-1-2012, 2012.
- Chu, V.W.: Greenland ice sheet hydrology: A review, *Prog. Phys. Geog.-Earth Env.*, 38, 19-54, doi: 10.1177/0309133313507075, 2014.
- Clark, R.W., Wellner, J.S., Hillenbrand, C.-D., Totten, R.L., Smith, J.A., Simkins, L.M., Larter, R.D., Hogan, K.A., Graha, A.G.C., Nitsche, F.O., Lehrmann, A.A., Lepp, A.P., Kirkham,

- J.D., Fitzgerald, V.T., Garcia-Barrera, G., Ehrmann, W., and Wacker, L.: Synchronous retreat of Thwaites and Pine Island glaciers in response to external forcings in the pre-satellite era, *P. Natl. Acad. Sci. USA* (in press), 2023.
- Clyne, E. R., Anandakrishnan, S., Muto, A., Alley, R.B., and Voigt, D.E.: Interpretation of topography and bed properties beneath Thwaites Glacier, West Antarctica using seismic reflection methods, *Earth Planet. Sc. Lett.*, 550, 116543, doi: 10.1016/j.epsl.2020.116543, 2020.
- Cooper, A.K., Davey, F.J., and Behrendt, J.C.: The Antarctic Continental Margin: Geology and Geophysics of the Western Ross Sea, Vol. 5B9, 27-65, Earth Science Series, Circum-Pacific Council for Energy and Mineral Resources, 1987.
- Cowan, E.A., Hillenbrand, C.-D., Hassler, L.E., and Ake, M.T.: Coarse-grained terrigenous sediment deposition on continental rise drifts: a record of Plio-Pleistocene glaciation on the Antarctic Peninsula, *Palaeogeogr. Palaeoclimatol.*, 265, 275-291, doi: 10.1016/j.palaeo.2008.03.010, 2008.
- Cowan, E.A., Christoffersen, P., and Powell, R.D.: Sedimentological signature of a deformable bed preserved beneath an ice stream in a late Pleistocene glacial sequence, Ross Sea, Antarctica, *J. Sediment. Res.*, 82, 270-282, doi: 10.2110/jsr.2012.25, 2012.
- Cowton, T., Nienow, P., Sole, A., Wadham, J., Lis, G., Bartholomew, I., Mair, D., and Chandler, D.: Evolution of drainage system morphology at a land-terminating Greenlandic outlet glacier, *J. Geophys. Res.-Earth*, 118, 29-41, doi: 10.1029/2012JF002540, 2013.
- Creys, T.T. and Clarke, G.K.C.: Hydraulics of subglacial supercooling: theory and simulations for clear water flows, *J. Geophys. Res.-Earth*, 115, F03021, doi: 10.1029/2009JF001417, 2010.
- Crompton, J.W., Flowers, G.E., and Dyck, B.: Characterization of glacial silt and clay using automated mineralogy, *Ann. Glaciol.*, 60, 49-65, doi: 10.1017/aog.2019.45, 2019.
- Croudace, I.W. and Rothwell, R.G.: *Micro-XRF studies of sediment cores*. Springer Netherlands, ISBN: 9789401798495, 9401798494, 2015.
- Cuffey, K.M., and Paterson, W.S.B.: *The Physics of Glaciers: Fourth Edition*, Academic Press, Burlington, Massachusetts, ISBN: 9780123694614, 2010.
- Damiani, T.M., Jordan, T.A., Ferraccioli, F., Young, D.A., and Blankenship, D.D.: Variable crustal thickness beneath Thwaites Glacier revealed from airborne gravimetry, possible implications for geothermal heat flux in West Antarctica, *Earth Planet. Sc. Lett.*, 407, 109-122, doi: 10.1016/j.epsl.2014.09.023, 2014.
- Dansgaard, W.: Stable isotopes in precipitation, *Tellus*, 16, 436-468, doi: 10.3402/tellusa.v16i4.8993, 1964.
- Darlington, E.F.: Meltwater delivery from the tidewater glacier Kronebreen to Kongsfjorden, Svalbard: Insights from in-situ and remote-sensing analyses of sediment plumes (PhD thesis), Loughborough University, 2015.
- Davarpanah Jazi, S. and Wells, M.G.: Dynamics of settling-driven convection beneath a sediment-laden buoyant overflow: Implications for the length-scale of deposition in lakes and the coastal ocean, *Sedimentology*, 67, 699-720. doi: 10.1111/sed.12660, 2020.
- Davies, J., Mathiasen, A.M., Kristiansen, K., Hansen, K.E., Wacker, L., Alstrup, A.K.O., Munk, O.L., Pearce, C., and Seidenkrantz, M-S.: Linkages between ocean circulation and the Northeast Greenland Ice Stream in the Early Holocene, *Quaternary Sci. Rev.*, 286, 107530, doi: 10.1016/j.quascirev.2022.107530, 2022.

- Davis, P.E.D., Nicholls, K.W., Holland, D.M., Schmidt, B.E., Washam, P., Riverman, K.L., Arthern, R.J., Vaňková, I., Eayrs, C., Smith, J.A., Anker, P.G.D., Mullen, A.D., Dichek, D., Lawrence, J.D., Meister, M.M., Clyne, E., Basinski-Ferris, A., Rignot, E., Queste, B.Y., Boehme, L., Heywood, K.J., Anandakrishnan, S., and Makinson, K.: Suppressed basal melting in the eastern Thwaites Glacier grounding zone, *Nature*, 614, 479-485, doi: 10.1038/s41586-022-05586-0, 2023.
- DeConto, R.M., Pollard, D., Alley, R.B., Velicogna, I., Gasson, E., Gomez, N., Sadai, S., Condrón, A., Gilford, D.M., Ashe, E.L., Kopp, R.E., Li, D., and Dutton, A.: The Paris Climate Agreement and future sea-level rise from Antarctica, *Nature*, 593, 83-89, doi: 10.1038/s41586-021-03427-0, 2021.
- Dickens, G.R., Koelling, M., Smith, D.C., Schnieders, L., and the IODP Expedition 302 Scientists: Rhizon sampling of pore waters on scientific drilling expeditions: an example from the IODP Expedition 302, Arctic Coring Expedition (ACEX), *Scientific Drilling*, 4, 22-25, doi: 10.2204/iodp.sd.4.08.2007, 2007.
- Domack, E. W. and Harris, P. T.: A new depositional model for ice shelves, based upon sediment cores from the Ross Sea and the Mac. Robertson shelf, Antarctica, *Ann. Glaciol.*, 27, 281–284, doi: 10.3189/1998AoS27-1-281-284, 1998.
- Domack, E.W., Jacobson, E.K., Shipp, S., and Anderson, J.B.: Late Pleistocene-Holocene retreat of the west Antarctic ice sheet system in the Ross Sea: Part 2 – sedimentologic and stratigraphic signature, *Geol. Soc. Am. Bull.*, 111, 1517-1536, 1999.
- Dow, C.F., Lee, W.S., Greenbaum, J.S., Greene, C.A., Blankenship, D.D., Poinar, K., Forrest, A.L., Young, D.A., and Zappa, C.J.: Basal channels drive active surface hydrology and transverse ice shelf fracture, *Sci. Adv.*, 4, eaao7212, doi: 10.1126/sciadv.aao7212, 2018.
- Dow, C.F., Ross, N., Jeofry, H., Siu, K., and Siegert, M.J.: Antarctic basal environment shaped by high-pressure flow through a subglacial river system, *Nat. Geosci.*, 15, 892-898, doi: 10.1038/s41561-022-01059-1, 2022.
- Dowdeswell, J.A., Hogan, K.A., Arnold, N.S., Mugford, R.I., Wells, M., Hirst, J.P.P., and Decalf, C.: Sediment-rich meltwater plumes and ice-proximal fans at the margins of modern and ancient tidewater glaciers: Observations and modelling, *Sedimentology*, 62, 1665-1692, doi: 10.1111/sed.12198, 2015.
- Dreimanis, A., and Vagners, U.J: Bimodal distribution of rock and mineral fragments in basal tills, *Glacial Till: An Interdisciplinary Study*, edited by: Legget, R.F., Royal Society of Canada, Special Publication, 12, 237-250, 1971.
- Dreimanis, A., and Vagners, U.J.: The effect of lithology upon texture of till, *Research methods in Pleistocene geomorphology*, 66-82, 1972.
- Dunnington, D.W., Spooner, I.S., Mallory, M.L., White, C.E., and Gagnon, G.A.: Evaluating the utility of elemental measurements obtained from factory-calibrated field-portable X-Ray fluorescence units for aquatic sediments, *Environ. Pollut.*, 249, 45-53, doi: 10.1016/j.envpol.2019.03.001, 2019.
- Dziadek, R., Ferraccioli, F., and Gohl, K.: High geothermal heat flow beneath Thwaites Glacier in West Antarctica inferred from aeromagnetic data, *Nat. Commun. Earth Environ.*, 162, doi: 10.1038/s43247-012-00242-3, 2021.
- Ebert, K., Willenbring, J., Norton, K.P., Hall, A., and Hättestrand, C.: Meteoric <sup>10</sup>Be concentrations from saprolite and till in northern Sweden: Implications for glacial erosion and age, *Quaternary Geochron.*, 12, 11-22, doi: 10.1016/j.quageo.2012.05.005, 2012.

- Ehrmann, W., Hillenbrand, C.-D., Smith, J.A., Graham, A.G.C., Kuhn, G., and Larter, R.D.: Provenance changes between recent and glacial-time sediments in the Amundsen Sea embayment, West Antarctica: clay mineral assemblage evidence, *Antarct. Sci.*, 23, 471-486, doi: 10.1017/S0954102011000320, 2011.
- Esteves, M., Bjarnadóttir, L.R., Winsborrow, M.C.M., Shackleton, C.S., and Andreassen, K.: Retreat patterns and dynamics of the Sentralbankrenna glacial system, central Barents Sea, *Quaternary Sci. Rev.*, 169, 131-147, doi: 10.1016/j.quascirev.2017.06.004, 2017.
- Esteves, M., Rütther, D., Winsborrow, M. C. M., Livingstone, S. J., Shackleton, C. S., and Andreassen, K.: An interconnected palaeo-subglacial lake system in the central Barents Sea, *EarthArxiv [ArXiv pre-print]*, doi:10.31223/X58934, 2022.
- Evans, D., Phillips, E., Hiemstra, J., and Auton, C.: Subglacial till: Formation, sedimentary characteristics and classification, *Earth Sci. Rev.*, 78, 115–176, doi: 10.1016/j.earscirev.2006.04.001, 2006.
- Evans, J., Pudsey, C.J., Ó Cofaigh, C., Morris, P., and Domack, E.: Late Quaternary glacial history, flow dynamics, and sedimentation along the eastern margin of the Antarctic Peninsula Ice Sheet, *Quaternary Sci. Rev.*, 24, 741-774, doi: 10.1016/j.quascirev.2004.10.007, 2005.
- Flowers, G. E.: Modelling water flow under glaciers and ice sheets, *P. R. Soc. A*, 471, 20140907, doi:10.1098/rspa.2014.0907, 2015.
- Flowers, G.E.: Hydrology and the future of the Greenland Ice Sheet, *Nat. Commun.*, 9, 2729, doi: 10.1038/s41467-018-05002-0, 2018.
- Folk, R.L. and Ward, W.C.: Brazos River bar [Texas]; a study in the significance of grain size parameters. *J. Sediment Res*, 27, 3-26, 1957.
- Fricker, H.A., Scambos, T., Bindschadler, R., and Padman, L.: An active subglacial water system in West Antarctica mapped from space, *Science*, 315, 1544-1548, doi: 10.1126/science.1136897, 2007.
- Fürst, J. J., Durand, G., Gillet-Chaulet, F., Tavad, L., Rankl, M., Braun, M., and Gagliardini, O.: The safety band of Antarctic ice shelves, *Nature Clim. Change*, 6, 479-482, doi: 10.1038/nclimate2912, 2016.
- Gerringa, L.J.A., Alderkamp, A-C, Laan, P., Thuróczy, C-E., De Baar, H.J.W., Mills, M.M., van Dijken, G.L., van Haren, H., and Arrigo, K.R.: Iron from melting glaciers fuels the phytoplankton blooms in Amundsen Sea (Southern Ocean): Iron biogeochemistry, *Deep Sea Research Part II: Topical Studies in Oceanography*, 71-76, 16-13, doi: 10.1016/j.dsr2.2012.03.007, 2012.
- Gilbert, E., and Kittel, C.: Surface melt and runoff on Antarctic ice shelves at 1.5 °C, 2 °C, and 4 °C of future warming, *Geophys. Res. Lett.*, 48, e2020GL091733, doi: 10.1029/2020GL091733, 2021.
- Gimbert, F., Tsai, V.C., Amundson, J.M., Bartholomaeus, T.C., and Walter, J.I.: Subseasonal changes observed in subglacial channel pressure, size, and sediment transport, *Geophys. Res. Lett.*, 43, 3786-3794, doi: 10.1002/2016GL068337, 2016.
- Golledge, N.R., Kowalewski, D.E., Naish, T.R., Levy, R.H., Fogwill, C.J., and Gasson, E.G.W.: The multi-millennial Antarctic commitment to future sea-level rise, *Nature*, 526, 421-425, doi: 10.1038/nature15706, 2015.
- Gourmelen, N., Goldberg, D., Snow, K., Henley, S., Bingham, R., Kimura, S., Hogg, A.E., Shepherd, A., Mouginos, J., Lenaerts, J.T.M., Ligtenberg, S.R.M., and van de Berg, W.J.:



- Channelized melting drives thinning under a rapidly melting Antarctic ice shelf, *Geophys. Res. Lett.*, 44, 9796–9804, doi: 10.1002/2017GL074929, 2017.
- Graham, A.G.C., Larter, R.D., Gohl, K., Dowdeswell, J.A., Hillenbrand, C.-D., Smith, J.A., Evans, J., Kuhn, G., and Deen, T.: Flow and retreat of the Late Quaternary Pine Island-Thwaites palaeo-ice stream, West Antarctica, *J. Geophys. Res.-Earth*, 115, F03025, doi: 10.1029/2009JF001482, 2010.
- Graham, A.G.C., Jakobsson, M., Nitsche, F.O., Larter, R.D., Anderson, J.B., Hillenbrand, C.-D., Gohl, K., Klages, J.P., Smith, J.A., and Jenkins, A.: Submarine glacial-landform distribution across the West Antarctic margin, from grounding line to slope: the Pine Island-Thwaites ice-stream system, *Geo. Soc. Mem.*, 46, 493-500, doi: 10.1144/M46.173, 2016.
- Greco, N., and Jaeger, J.M.: Modeling Mud: Floccs as Global Meltwater Indicators in Ice-Proximal Glacimarine Sediments, *AGU Fall Meeting Abstracts*, 2020, EP001-0014, 2020.
- Greenwood, S. L., Gyllencreutz, R., Jakobsson, M., and Anderson, J. B.: Ice-flow switching and East/West Antarctic Ice Sheet roles in glaciation of the western Ross Sea, *Geol. Soc. Am. Bull.*, 124, 1736–1749, doi:10.1130/B30643.1, 2012.
- Greenwood, S.L., Clason, C.C., Helanow, C., and Margold, M.: Theoretical, contemporary observational and palaeo-perspectives on ice sheet hydrology: Processes and products, *Earth Sci. Rev.*, 15, 1-27, doi:10.1016/j.earscirev.2016.01.010, 2016.
- Greenwood, S.L., Simkins, L.M., Halberstadt, A.R.W., Prothro, L.O., and Anderson, J.B.: Holocene reconfiguration and readvance of the East Antarctic Ice Sheet, *Nat. Commun.*, 9, 3176, doi: 10.1038/s41467-018-05625-3, 2018.
- Greenwood, S. L., Simkins, L. M., Winsborrow, M. C. and Bjarnadóttir, L. R. Exceptions to bed-controlled ice sheet flow and retreat from glaciated continental margins worldwide. *Sci. Adv.* 7, doi:10.1126/sciadv.abb6291, 2021.
- Gustafson, C.D., Key, K., Siegfried, M.R., Winberry, J.P., Fricker, H.A., Venturelli, R.A., and Michaud, A.B.: A dynamic saline groundwater system mapped beneath an Antarctic ice stream, *Science*, 376, 640-644, doi: 10.1126/science.abm3301, 2022.
- Gwyther, D.E., Dow, C.F., Jendersie, S., Gourmelen, N., and Galton-Fenzi, B.K.: Subglacial freshwater drainage increases simulated basal melt of the Totten Ice Shelf, *Geophys. Res. Lett.*, 50, e2023GL103765, doi: 10.1029/2023GL103765, 2023.
- Hager, A.O., Hoffman, M.J., Price, S.F., and Schroeder, D.M.: Persistent, extensive channelized drainage modeled beneath Thwaites Glacier, West Antarctica, *Cryosphere*, 16, 3575-3599, doi: 10.5194/tc-2021-338, 2022.
- Hahn, A., Bowen, M.G., Clift, P.D., Kilhanek, D.K., and Lyle, M.W.: Testing the analytical performance of handheld XRF using marine sediments of IODP Expedition 355, *Geol. Mag.*, 157, 956-960, doi:10.1017/S0016756819000189, 2019.
- Halberstadt, A.R.W, Simkins, L., Greenwood, S., and Anderson, J., Past ice-sheet behaviour: Retreat scenarios and changing controls in the Ross Sea, Antarctica, *Cryosphere*, 10, 1003-1020, doi: 10.5194/tc-10-1003-2016, 2016.
- Halberstadt, A.R.W., Simkins, L.M., Anderson, J.B., Prothro, L.O., and Bart, P.J.: Characteristics of the deforming bed: till properties on the deglaciated Antarctic continental shelf. *J. Glaciol.*, 64, 1014-1027, doi: 10.1017/jog.2018.92, 2018.
- Haldorsen, S.: Grain-size distribution of subglacial till and its relation to glacial crushing and abrasion, *Boreas*, 10, 91-105, doi: 10.1111/j.1502-3885.1981.tb00472.x, 1981.

- Hansen, D.D. and Zoet, L.K.: Characterizing sediment flux of deforming glacier beds, *J. Geophys. Res.-Earth*, 127, e2021JF006544, doi: 10.1029/2021JF006544, 2022.
- Hart, J.K.: Athabasca Glacier, Canada – a field example of subglacial ice and till erosion? *Earth Surf. Proc. Land.*, 31, 65-80, doi: 10.1002/esp.1233, 2006.
- Hawkesworth, C.J., Turner, S.P., McDermott, F., Peate, D.W., and van Calsteren, P.: U-Th isotopes in arc magmas: implications for element transfer from the subducted crust *Science*, 276, 551-555, doi: 10.1126/science.276.5312.551, 1997.
- Hawkings, J.R., Skidmore, M.L., Wadham, J.L., Priscu, J.C., Morton, P.L., Hatton, J.E., Gardner, C.B., Kohler, T.J., Stibal, M., Bagshaw, E.A., Steigmeyer, A., Barker, J., Dore, J.E., Lyons, W.B., Tranter, M., Spencer, R.G.M., and the SALSA Science Team: Enhanced trace element mobilization by Earth's ice sheets, *P. Natl. Acad. Sci. USA*, 117, 31648-31659, doi: 10.1073/pnas.2014378117, 2020.
- Heaton, T.J., Köhler, P., Buztin, M., Bard, E., Reimer, R.W., Austin, W.E.N., Ramsey, C.B., Grootes, P.M., Hughen, K.A., and Kromer, B.: Marine20 – the Marine Radiocarbon age calibration curve (0-55,000 cal BP), *Radiocarbon*, 62, 779-820, doi: 10.1017/RDC.2020.68, 2020.
- Hellmer, H.H., Jacobs, S.S., and Jenkins, A.: Oceanic erosion of a floating Antarctic glacier in the Amundsen Sea, *Antarctic Res. Ser.*, 75, 83-99, 1998.
- Henriksen, N., Higgins, A., Kalsbeck, F., and Pulvertaft, T.C.R.: Greenland from Archaen to Quaternary. Descriptive text to the 1995 Geological map of Greenland, 1:2,500,000. 2<sup>nd</sup> edition, *GEUS Bulletin*, 18, 1-126, doi: 10.31494/geusb.v18.4993, 2009.
- Herbert, L.C., Riedinger, N., Michaud, A.B., Laufer, K., Røy, H., Jørgensen, B.B., Heilbrun, C., Aller, R.C., Cochran, J.K., Wehrmann, L.M.: Glacial controls on redox-sensitive trace element cycling in Arctic fjord sediments (Spitsbergen, Svalbard), *Geochim. Cosmochim. Ac.*, 271, 33-60, doi: 10.1016/j.gca.2019.12.005, 2020.
- Herbert, L.C., Lepp, A.P., Munevar Garcia, S., Browning, A., Miller, L.E., Wellner, J., Severmann, S., Hillenbrand, C.-D., Johnson, J.S., and Sherrell, R.M.: Volcanogenic fluxes of iron from the seafloor in the Amundsen Sea, West Antarctica, *Mar. Chem.*, 104250, doi: 10.1016/j.marchem.2023.104250, 2023.
- Hillenbrand, C.-D., Grobe, H., Diekmann, B., Kuhn, G., and Fütterer, D.K.: Distribution of clay minerals and proxies for productivity in surface sediments of the Bellingshausen and Amundsen seas (West Antarctica) – relation to modern environmental conditions, *Mar. Geol.*, 193, 253-271, doi: 10.1016/S0025-3227(02)00659-X, 2003.
- Hillenbrand, C.-D., Baesler, A., and Grobe, H.: The sedimentary record of the last glaciation in the western Bellingshausen Sea (West Antarctica): Implications for the interpretation of diamictons in a polar-marine setting, *Mar. Geol.*, 216, 191-204, doi: 10.1016/j.margeo.2005.01.007, 2005.
- Hillenbrand, C.-D., Kuhn, G., Smith, J.A., Gohl, K., Graham, A.G.C., Larter, R.D., Klages, J.P., Downey, R., Moreton, S.G., Forwick, M., and Vaughan, D.G.: Grounding-line retreat of the West Antarctic Ice Sheet from inner Pine Island Bay, *Geology*, 41, 35-38, doi: 10.1130/G33469.1, 2013.
- Hillenbrand, C.-D., Smith, J.A., Hodell, D.A., Greaves, M., Poole, C.M., Kender, S., Williams, N., Anderson, T.J., Jernas, P.E., Elderfield, H., Klages, J.P., Roberts, S.J., Gohl, K., Larter, R.D., and Kuhn, G.: West Antarctic Ice Sheet retreat driven by Holocene warm water incursions, *Nature*, 547, 43-48, doi: 10.1038/nature22995, 2017.

- Hodson, T.O., Powell, R.D., Brachfeld, S.A., Tulaczyk, S., Scherer, R.P., and the WISSARD Science Team: Physical processes in Subglacial Lake Whillans, West Antarctica: Inferences from sediment cores, *Earth Planet. Sc. Lett.*, 444, 56-63, doi: 10.1016/j.epsl.2016.03.036, 2016.
- Hoffman, M.J., Asay-Davis, X., Price, S.F., Fyke J., and Perego, M.: Effect of subshelf melt variability on sea level rise contribution from Thwaites Glacier, Antarctica, *J. Geophys. Res.-Earth*, 124, 2798-2822, doi: 10.1029/2019JF005155, 2019.
- Hoffman, A.O., Christianson, K., Shapero, D., Smith, B.E., and Joughin, I.: Brief Communication: Heterogenous thinning and subglacial lake activity on Thwaites Glacier, West Antarctica, *Cryosphere*, 14, 4603-4609, doi: 10.5194/tc-14-4603-2020, 2020.
- Hogan, K.A., Larter, R.D., Graham, A.G.C., Arthern, R., Kirkham, J.D., Minzoni, R.T., Jordan, T.A., Clark, R., Fitzgerald, V., Wåhlin, A. K., Anderson, J.B., Hillenbrand, C.-D., Nitsche, F.O., Simkins, L., Smith, J.A., Gohl, K., Arndt, J.A., Hong, J., and Wellner, J.: Revealing the former bed of Thwaites Glacier using sea-floor bathymetry: implications for warm-water routing and bed controls on ice flow and buttressing, *Cryosphere*, 14, 2883–2908, doi: 10.5194/tc-14-2883-2020, 2020a.
- Hogan, K.A., Jakobsson, M., Mayer, L., Reilly, B.T., Jennings, A.E., Stoner, J.S., Nielsen, T., Andresen, K.J., Nørmark, E., Heirman, K.A., Kamla, E., Jerram, K., Stranne, C., and Mix, A.: Glacial sedimentation, fluxes, and erosion rates associated with ice retreat in Petermann Fjord and Nares Strait, north-west Greenland, *Cryosphere*, 14, 261-286, doi: 10.5194/tc-14-261-2020, 2020b.
- Hogan, K.A., Arnold, N.S., Larter, R.D., Kirkham, J.D., Noormets, R., Ó Cofaigh, C., Golledge, N.R., and Dowdeswell, J.A.: Subglacial water flow over an Antarctic palaeo-ice stream bed, *J. Geophys. Res.-Earth*, 127, e2021JF006442, doi: 10.1029/2021JF006442, 2022.
- Holland, D.M., Nicholls, K.W., and Basinski, A.: The Southern Ocean and its interaction with the Antarctic Ice Sheet, *Science*, 367, 1326-1330, doi: 10.1126/science.aaz5491, 2020.
- Holt, J.W., Blankenship, D.D., Morse, D.L., Young, D.A., Peters, M.E., Kempf, S.D., Richter, T.G., Vaughan, D.G., and Corr, H.F.J.: New boundary conditions for the West Antarctic Ice Sheet: Subglacial topography of the Thwaites and Smith glacier catchments, *Geophys. Res. Lett.*, 33, L09502, doi: 10.1029/2005GL025588, 2006.
- Houbin, A.J.P., Bijl, P.J., Sluijs, A., Schouten, S., and Brinkhuis, H: Late Eocene Southern Ocean Cooling and Invigoration of Circulation Preconditioned Antarctica for Full-Scale Glaciation, *Geochem., Geophys., Geosys.*, 20, 2214-2234, doi: 10.1029/2019GC008182, 2019.
- Immonen, N.: Surface microtextures of ice-rafted quartz grains revealing glacial ice in the Cenozoic Arctic, *Palaeogeogr. Palaeoclimatol.*, 374, 293-302, doi: 10.1016/j.palaeo.2013.02.003, 2013.
- Iverson, N.R. and Souchez, R.: Isotopic signature of debris-rich ice formed by regelation into a subglacial sediment bed. *Geophys. Res. Lett.*, 23, 1151-1154, doi: 10.1029/96GL01073, 1996.
- Iverson, N.R., Hooyer, T.S., and Hooke, R.L.: A laboratory study of sediment deformation: stress heterogeneity and grain-size evolution, *Ann. Glaciol.*, 22, 167-175, doi: 10.3189/1996AoS22-1-167-175, 1996.
- Iverson, N.R.: Shear resistance and continuity of subglacial till: hydrology rules, *J. Glaciol.*, 56, 1104-1114, doi: 10.3189/002214311796406220, 2010.

- Iverson, N.R., McCracken, R.G., Zoet, L.K., Benediktsson, Í. Ö., Schomacker, A., Johnson, M.D., and Woodard, J.: A theoretical model of drumlin formation based on observations at Múlajökull, Iceland, *J. Geophys. Res.-Earth*, 122, 2302-2323, doi: 10.1002/2017JF004354, 2017.
- Jackson, R.H., Shroyer, E.L., Nash, J.D., Sutherland, D.A., Carroll, D., Fried, M.J., Catania, G.A., Bartholomew, T.C., and Stearns, L.A.: Near-glacier surveying of a subglacial discharge plume: Implications for plume parameterizations, *Geophys. Res. Lett.*, 44, 6886-6894, doi: 10.1002/2017GL073602, 2017.
- Jakobsson, M., Hogan, K.A., Mayer, L.A., Mix, A., Jennings, A., Stoner, J., Eriksson, B., Jerram, K., Mohammad, R., Pearce, C., Reilly, B., and Stranne, C.: The Holocene retreat dynamics and stability of Petermann Glacier in northwest Greenland, *Nat. Commun.*, 9, 2104, doi: 10.1038/s41467-018-04573-2, 2018.
- Jenkins, A., Dutrieux, P., Jacobs, S.S., McPhail, S.D., Perrett, J.R., Webb, A.T., and White, D.: Observations beneath Pine Island Glacier in West Antarctica and implications for its retreat, *Nature Geosci.*, 3, 468-472, doi: 10.1038/ngeo890, 2010.
- Jenkins, A.: Convection-driven melting near the grounding lines of ice shelves and tidewater glaciers. *J. Phys. Oceanogr.*, 41, 2279-2294, doi: 10.1175/JPO-D-11-03.1, 2011.
- Jennings, A., Reilly, B., Andrews, J., Hogan, K., Walczak, M., Jakobsson, M., Stoner, J., Mix, A., Nicholls, K.W., O'Regan, M., Prins, M.A., and Troelstra, S.R.: Modern and early Holocene ice shelf sediment facies from Petermann Fjord and northern Nares Strait, northwest Greenland, *Quaternary Sci. Rev.*, 283, 107460, doi: 10.1016/j.quascirev.2022.107460, 2022.
- Jordan, T.A., Porter, D., Tinto, K., Millan, R., Muto, A., Hogan, K., Larter, R.D., Graham, A.G.C., and Paden, J.D.: New gravity-derived bathymetry for the Thwaites, Crosson, and Dotson ice shelves revealing two ice shelf populations, *Cryosphere*, 14, 2869-2882, doi: 10.5194/tc-14-2869-2020.
- Jordan, T.A., Thompson, S., Kulesa, B., and Ferraccioli, F.: Geological sketch map and implications for ice flow of Thwaites Glacier, West Antarctica, from integrated aerogeophysical observations, *Sci. Adv.*, 9, eadf2639, doi: 10.1126/sciadv.adf2639, 2023.
- Joughin, I., Tulaczyk, S., Bamber, J.L., Blankenship, D., Holt, J.W., Scambos, T., and Vaughan, D.G.: Basal conditions for Pine Island and Thwaites glaciers, West Antarctica, determined using satellite and airborne data, *J. Glaciol.*, 55, 245-257, doi: 10.3189/002214309788608705, 2009.
- Joughin, I., Smith, B.E., and Medley, B.: Marine ice sheet collapse potentially under way for the Thwaites Glacier Basin, West Antarctica, *Science*, 344, 735-738, doi: 10.1126/science.1249055, 2014.
- Jung, J., Yoo, K.-C., Rosenheim, B.E., Conway, T.M., Lee, J.I., Yoon, H.I., Hwang, C.Y., Yang, K., Subt, C., and Kim, J.: Microbial Fe(III) reduction as a potential iron source from Holocene sediments beneath Larsen Ice Shelf, *Nat. Commun.*, 10, 5786, doi: 10.1038/s41467-019-13741-x, 2019.
- Kennedy, D.S. and Anderson, J.B.: Glacial-marine sedimentation and Quaternary glacial history of Marguerite Bay, Antarctic Peninsula, *Quaternary Res.*, 31, 255-276, doi: 10.1016/0033-5894(89)90008-2, 1989.
- Khazendar, A., Rignot, E., Schroeder, D.M., Seroussi, H., Schodlok, M.P., Scheuchl, B., Mougintot, J., Sutterley, T.C., and Velicogna, I.: Rapid submarine ice melting in the

- grounding zones of ice shelves in West Antarctica, *Nat. Commun.*, 7, 13243, doi: 10.1038/ncomms13243, 2016.
- Kilfeather, A.A., Ó Cofaigh, C., Lloyd, J.M., Dowdeswell, J.A., Xu, S., and Moreton, S.G.: Ice-stream retreat and ice-shelf history in Marguerite Trough, Antarctic Peninsula: Sedimentological and foraminiferal signatures, *Geol. Soc. Am. Bull.*, 123, 997-1015, doi: 10.1130/B30282.1, 2011.
- King, M.V., Gales, J.A., Laberg, J.S., McKay, R.M., De Santis, L., Kulhanek, D.K., Hosegood, P.J., Morris, A., and IODP Expedition 374 Scientists: Pleistocene depositional environments and links to cryosphere-ocean interactions on the eastern Ross Sea continental slope, Antarctica (IODP Hole U1525A), *Mar. Geol.*, 443, 106674, doi:10.1016/j.margeo.2021.106674, 2022.
- Kirkham, J.D., Hogan, K.A., Larter, R.D., Arnold, N.S., Nitsche, F.O., Golledge, N.R., and Dowdeswell, J.A.: Past water flow beneath Pine Island and Thwaites glaciers, West Antarctica, *Cryosphere*, 13, 1959-1981, doi: 10.5194/tc-13-1959-2019, 2019.
- Kirkham, J.D., Hogan, K.A., Larter, R.D., Arnold, N.S., Nitsche, F.O., Kuhn, G., Gohl, K., Anderson, J.B., and Dowdeswell, J.A.: Morphometry of bedrock meltwater channels on Antarctic inner continental shelves: Implications for channel development and subglacial hydrology, *Geomorphology*, 370, 107369, doi: 10.1016/j.geomorph.2020.107369, 2020.
- Kirshner, A.E., Anderson, J.B., Jakobsson, M., O'Regan, M., Majewski, W., and Nitsche, F.O.: Post-LGM deglaciation in Pine Island Bay, West Antarctica, *Quaternary Sci. Rev.*, 38, 11-26, doi: 10.1016/j.quascirev.2012.01.017, 2012.
- Knight, P.G., Waller, R.I., Patterson, C.J., Jones, A.P., and Robinson, Z.P.: Discharge of debris from ice at the margin of the Greenland ice sheet, *J. Glaciol.*, 48, 192-198, doi: 10.3189/172756502781831359, 2002.
- Krabbendam, M.: Sliding of temperate basal ice on a rough, hard bed: creep mechanisms, pressure melting, and implications for ice streaming, *Cryosphere*, 10, 1915-1932, doi: 10.5194/tc-10-1915-2016, 2016.
- Křížek, M., Krbcová, K., Mida, P., and Hanáček, M.: Micromorphological changes as an indicator of the transition from glacial to glaciofluvial quartz grains: Evidence from Svalbard, *Sediment. Geol.*, 358, 35-43, doi:10.1016/j.sedgeo.2017.06.010, 2017.
- Kuhn, G., Hillenbrand, C.-D., Kasten, S., Smith, J.A., Nitsche, F.O., Frederichs, T., Wiers, S., Ehrmann, W., Klages, J.P., and Mogollon, J.M.: Evidence for a palaeo-subglacial lake on the Antarctic continental shelf, *Nat. Commun.*, 8, 15591, doi: 10.1038/ncomms15591, 2017.
- Kumar, O., Ramanathan, A.L., Bakke, J., Kotlia, B.S., and Shrivastava, J.P.: Disentangling source of moisture driving glacier dynamics and identification of 8.2 ka event: evidence from pore water isotopes, Western Himalaya, *Sci. Rep.*, 10, 15324, doi: 10.1038/s41598-020-71686-4, 2020.
- Lamping, N., Müller, J., Esper, O., Hillenbrand, C.-D., Smith, J.A., and Kuhn, G.: Highly branched isoprenoids reveal onset of deglaciation followed by dynamic sea-ice conditions in the western Amundsen Sea, Antarctica, *Quaternary Sci. Rev.*, 228, 106103, doi: 10.1016/j.quascirev.2019.106103, 2020.
- Larter, R.D., Anderson, J.B., Graham, A.G.C., Gohl, K., Hillenbrand, C.-D., Jakobsson, M., Johnson, J.S., Kuhn, G., Nitsche, F.O., Smith, J.A., Witus, A.E., Bentley, M.J., Dowdeswell, J.A., Ehrmann, W., Klages, J.P., Lindow, J., Ó Cofaigh, C., and Spiegel, C.: Reconstruction of changes in the Amundsen Sea and Bellingshausen Sea sector of the

- West Antarctic Ice Sheet since the Last Glacial Maximum, *Quaternary Sci. Rev.*, 100, 55-86, doi: 10.1016/j.quascirev.2013.10.016, 2014.
- Le Brocq, A.M., Ross, N., Griggs, J.A., Bingham, R.G., Corr, H.F., Ferraccioli, F., Jenkins, A., Jordan, T.A., Payne, A.J., Rippin, D.M., and Siegert, M.J.: Evidence from ice shelves for channelized meltwater flow beneath the Antarctic Ice Sheet, *Nat. Geosci.*, 6, 945–948, doi: 10.1038/ngeo1977, 2013.
- Lecavalier, B.S., Fisher, D.A., Milne, G.A., Vinther, B.M., Tarasov, L., Huybrechts, P., Lacelle, D., Main, B., Zheng, J., Bourgeois, J., and Dyke, A.S.: High Arctic Holocene temperature record from the Agassiz ice cap and Greenland ice sheet evolution, *P. Natl. Acad. Sci. USA*, 114, 5952-5957, doi: 10.1073/pnas.1616287114, 2017.
- Lenaerts, J.T.M., Vizcaino, M., Fyke, J., van Kampenhout, L., and van den Broeke, M.R.: Present-day and future Antarctic ice sheet climate and surface mass balance in the Community Earth System Model, *Clim. Dynam.*, 47, 1367-1381, doi: 10.1007/s00382-015-2907-4, 2016.
- Lepp, A.P., Simkins, L.M., Anderson, J.B., Clark, R.W., Wellner, J.S., Hillenbrand, C.-D., Smith, J.A., Lehrmann, A.A., Totten, R., Larter, R.D., Hogan, K.A., Nitsche, F.O., Graham, A.G.C., and Wacker, L.: Sedimentary signatures of persistent subglacial meltwater drainage from Thwaites Glacier, Antarctica, *Front. Earth Sci.*, 10:863200, doi: 10.3389/feart.2022.863200, 2022.
- Lepp, A.P., Miller, L.E., Anderson, J.B., O'Regan, M., Winsborrow, M.C.M., Smith, J.A., Hillenbrand, C.-D., Wellner, J.S., Prothro, L.O., and Podolskiy, E.A.: Insights into glacial processes from micromorphology of silt-sized sediment, *Cryosphere Discuss.* [preprint], doi: 10.5194/tc-2023-70, in review, 2023.
- Lešić, N.-M., Streuff, K.T., Bohrmann, G., and Kuhn, G.: Glacimarine sediments from outer Drygalski Trough, sub-Antarctic South Georgia – evidence for extensive glaciation during the Last Glacial Maximum, *Quaternary Sci. Rev.*, 292, 107657, doi: 10.1016/j.quascirev.2022.107657, 2022.
- Li, Y.-H. and Gregory, S.: Diffusion of ions in sea water and in deep-sea sediments. *Geochim. Cosmochim. Ac.*, 38, 703-714, doi: 10.1016/0016-7037(74)90145-8, 1974.
- Licht, K.J., Lederer, J.R., and Swope, R.J.: Provenance of LGM glacial till (sand fraction) across the Ross embayment, Antarctica, *Quaternary Sci. Rev.*, 24, 1499-1520, doi: 10.1016/j.quascirev.2004.10.017, 2005.
- Livingstone, S.J., Ó Cofaigh, C., Stokes, C.R., Hillenbrand, C.-D., Vieli, A., and Jamieson, S.S.R.: Glacial geomorphology of Marguerite Bay Palaeo-Ice stream, western Antarctic Peninsula, *J. Maps*, 9, 558-572, doi: 10.1080/17445647.2013.829411, 2013.
- Livingstone, S.J., Stokes, C.R., Cofaigh, C.Ó., Hillenbrand, C.-D., Vieli, A., Jamieson, S.S.R., Spagnolo, M., and Dowdeswell, J.A.: Subglacial processes on an Antarctic ice stream bed. 1: Sediment transport and bedform genesis inferred from marine geophysical data. *J. Glaciol.*, 62, 270–284, doi: 10.1017/jog.2016.18, 2016.
- Livingstone, S.J., Li, Y., Rutishauser, A., Sanderson, R.J., Winter, K., Mikucki, J.A., Björnsson, H., Bowling, J.S., Chu, W., Dow, C.F., Fricker, H.A., McMillan, M., Ng, F.S.L., Ross, N., Sieger, M.J., Siegfried, M., and Sole, A.J.: Subglacial lakes and their changing role in a warming climate, *Nat. Rev. Earth Environ.*, 3, 106-124, doi: 10.1038/s43017-021-00246-9, 2022.
- Livsey, D.N., Simms, A.R., Clary, W.G., Wellner, J.S., Anderson, J.B., and Chandler, J.P.: Fourier grain-shape analysis of Antarctic marine core: the relative influence of

- provenance and glacial activity on grain shape, *J. Sediment. Res.*, 83, 80-90, doi: 10.2110/jsr.2013.5, 2013.
- Lowe, A. L. and Anderson, J. B.: Evidence for abundant subglacial meltwater beneath the paleo-ice sheet in Pine Island Bay, Antarctica, *J. Glaciol.*, 49, 125–138, doi: 10.3189/172756503781830971, 2003.
- MacGregor, J.A., Catania, G.A., Markowski, M.S., and Andrews, A.G.: Widespread rifting and retreat of ice-shelf margins in the eastern Amundsen Sea Embayment between 1972 and 2011, *J. Glaciol.*, 58, 458-466, doi: 10.3189/2012JoG11J262, 2012.
- Mahaney, W.C.: Atlas of sand grain surface textures and applications, Oxford University Press, USA, 2002.
- Majewski, W.: Benthic foraminifera from Pine Island and Ferrero bays, Amundsen Sea, *Pol. Polar Res.*, 34, 169-200, doi: 10.2478/popore-2013-0012, 2013.
- Majewski, W., Prothro, L. O., Simkins, L. M., Demianiuk, E. J., and Anderson, J. B.: Foraminiferal patterns in deglacial sediment in the Western Ross Sea, Antarctica: Life near grounding lines. *Paleoceanography and Paleoclimatology*, 35, e2019PA003716, doi: 10.1029/2019PA003716, 2020.
- Malczyk, G., Gourmelen, N., Goldberg, D., Wuite, J., and Nagler, T.: Repeat subglacial lake drainage and filling beneath Thwaites Glacier, *Geophys. Res. Lett.*, 47, e2020GL089658, doi: 10.1029/2020GL089658, 2020.
- Mankoff, K. D., Jacobs, S. S., Tulaczyk, S. M., and Stammerjohn, S. E.: The role of Pine Island Glacier Ice Shelf basal channels in deep-water upwelling, polynyas and ocean circulation in Pine Island Bay, Antarctica, *Ann. Glaciol.*, 53, 123–128, doi: 10.1038/ngeo2675, 2012.
- Manning, A.J., Spearman, J.R., Whitehouse, R.J.S., Pidduck, E.L., Baugh, J.V., and Spencer, K.L.: Flocculation Dynamics of Mud: San Mixed Suspensions, in: *Sediment transport processes and their modelling applications*, edited by: Manning, A.J., InTech, Rijeka, Croatia, 119-125, doi:10.5772/55233, 2013.
- Marsaglia, K., Milliken, K., and Doran, L.: IODP digital reference for smear slide analysis of marine mud. Part 1: Methodology and atlas of siliciclastic and volcanogenic components, IODP Technical Note 1, doi: 10.2204/iodp.tn.1.2013, 2013.
- Marsh, O. J., Fricker, H.A., Siegfried, M.R., Christianson, K., Nicholls, K.W., Corr, H.F.J., and Catania, G.: High basal melting forming a channel at the grounding line of Ross Ice Shelf, Antarctica, *Geophys. Res. Lett.*, 43, 250-255, doi: 10.1002/2015GL066612, 2016.
- Masson-Delmotte, V., Jouzel, J., Landais, A., Stievenard, M., Johnsen, S.J., White, J.W.C., Werner, M., Sveinbjornsdottir, A., and Fuhrer, K.: GRIP Deuterium Excess reveals rapid and orbital-scale changes in Greenland moisture origin, *Science*, 309, 118-121, doi: 10.1126/science.1108575, 2005.
- Masson-Delmotte, V., Hou, S., Ekaykin, A., Jouzel, J., Aristarain, A., Bernardo, R.T., Bromwich, D., Cattani, O., Delmotte, M., Falourd, S., Frezzotti, M., Gallée, H., Genoni, L., Isaksson, E., Landais, A., Helsen, M.M., Hoffmann, G., Lopez, J., Morgan, V., Motoyama, H., Noone, D., Oerter, H., Petit, J.R., Royer, A., Uemura, R., Schmidt, G.A., Schlosser, E., Simões, J.C., Steig, E.J., Stenni, B., Stievenard, M., van den Broeke, M.R., van de Wal, R.S.W., van de Berg, W.J., Vimeux, F., and White, J.W.C.: A review of Antarctic surface snow isotopic composition: observations, atmospheric circulation, and isotopic modeling, *J. Climate*, 21, 3359-3387, doi: 10.1175/2007JCLI2139.1, 2008.

- McDonald, N., Bradwell, T., Callard, S.L., Toney, J.L., Shreeve, B., and Shreeve, J.: Automated characterization of glaciomarine sediments using X-ray computed laminography, *Quaternary Sci. Adv.*, 5, 100046, doi: 10.1016/j.qsa.2021.100046, 2022.
- McFarlin, J.M., Axford, Y., Osburn M.R., Kelly, M.A., Osterberg, E.C., and Farnsworth, L.B.: Pronounced summer warming in northwest Greenland during the Holocene and Last Interglacial, *P. Natl. Acad. Sci. USA*, 201720420, doi: 10.1073/pnas.1720420115, 2018.
- Menzies, J.: Strain pathways, till internal architecture and microstructures-perspectives on a general kinematic model – a ‘blueprint’ for till development, *Quaternary Sci. Rev.*, 50, 105-124, doi: 10.1016/j.quascirev.2012.07.012, 2012.
- Meredith, M.P., Falk, U., Bers, A.V., Mackensen, A., Schloss, I.R., Barlett, E.R., Jerosch, K., Busso, A.S., and Abele, D.: Anatomy of a glacial meltwater discharge event in an Antarctic cove, *Philos. T. R. Soc. A.*, 376, 20170163, doi: 10.1098/rsta.2017.0163, 2018.
- Meyer, C.R., Robel, A.A., and Rempel, A.W.: Frozen fringe explains sediment freeze-on during Heinrich events, *Earth Plan. Sci. Lett.*, 524, 115725, doi: 10.1016/j.eosl.2019/115725, 2019.
- Miles, B., Stokes, C., Jenkins, A., Jordan, J., Jamieson, S., and Gudmundsson, G.: Intermittent structural weakening and acceleration of the Thwaites Glacier Tongue between 2000 and 2018, *J. Glaciol.*, 66, 485-495. Doi: 10.1017/jog.2020.20, 2020.
- Milillo, P., Rignot, E., Rizzoli, P., Scheuchl, B., Mouginot, J., Bueso-Bello, J., and Iraola-Prats, P.: Heterogeneous retreat and ice melt of Thwaites Glacier, West Antarctica. *Science Adv.*, 5, eaau3433, doi: 10.1126/sciadv.aau3433, 2019.
- Millan, R., Rignot, E., Bernier, V., Morlighem, M., and Dutrieux, P.: Bathymetry of the Amundsen Sea Embayment sector of West Antarctica from Operation IceBridge gravity and other data, *Geophys. Res. Lett.*, 44, 1360-1368 doi: 10.1002/2016GL072071, 2017.
- Miller, M.D., Adkins, J.F., and Hodell, D.A.: Rhizon sampler alteration of deep ocean sediment interstitial water samples, as indicated by chloride concentration and oxygen and hydrogen isotopes, *Geochem. Geophys. Geosy.*, 15, 2401-2413, doi: 10.1002/2014GC005308, 2014.
- Milliken, K.T., Anderson, J.B., Wellner, J.S., Bohaty, S.M., and Manley, P.L.: High-resolution Holocene climate record from Maxwell Bay, South Shetland Islands, Antarctica, *GSA Bulletin*, 121, 1711-1725, doi: 10.1130/B26478.1, 2009.
- Minzoni, R.T., Anderson, J.B., Fernandez, R., and Wellner, J.S.: Marine record of Holocene climate, ocean, and cryosphere interactions: Herbert Sound, James Ross Island, Antarctica, *Quaternary Sci. Rev.*, 129, 239-259, doi: 10.1016/j.quascirev.2015.09.009, 2015.
- Morlighem, M., Rignot, E., Binder, T., Blankenship, D., Drews, R., Eagles, G., et al.: Deep glacial troughs and stabilizing ridges unveiled beneath the margins of the Antarctic ice sheet, *Nat. Geosci.*, 13, 132– 137, doi:10.1038/s41561-019-0510-8, 2020.
- Mugford, R.I., and Dowdeswell, J.A.: Modeling glacial meltwater plume dynamics and sedimentation in high-latitude fjords, *J. Geophys. Res.-Earth*, 116, F01023, doi: 10.1029/2010JF001735, 2011.
- Munoz, Y.P. and Wellner, J.S.: Seafloor geomorphology of western Antarctic Peninsula bays: a signature of ice flow behavior, *Cryosphere*, 12, 205-225, doi: 10.5194/tc-12-205-2018, 2018.
- Muto, A., Peters, L.E., Gohl, K., Sasgen, I., Alley, R.B., Anandakrishnan, S., and Riverman, K.L.: Subglacial bathymetry and sediment distribution beneath Pine Island Glacier ice



- shelf modeled using aerogravity and in situ geophysical data: new results, *Earth Planet. Sc. Lett.*, 443, 63-75, doi: 10.1016/j.epsl.2015.10.037, 2016.
- Nakayama, Y., Cai, C., and Seroussi, H.: Impact of subglacial freshwater discharge on Pine Island Ice Shelf, *Geophys. Res. Lett.*, 48, e2021GL093923, doi: 10.1029/2021GL093923, 2021.
- Nanni, U., Gimbert, F., Vincent, C., Gräff, D., Walter, F., Piard, L., and Moreau, L.: Quantification of seasonal and diurnal dynamics of subglacial channels using seismic observations on an Alpine glacier, *Cryosphere*, 14, 1475-1496, doi: 10.5194/tc-14-1475-2020, 2020.
- Neuhaus, S.U., Tulaczyk, S.M., Stansell, N.D., Coenen, J.J., Scherer, R.P., Mikucki, J.A., and Powell, R.D.: Did Holocene climate changes drive West Antarctic grounding line retreat and advance? *Cryosphere*, 15, 4655-4673, doi: 10.5194/tc-15-4655-2021, 2021.
- Nitsche, F.O., Gohl, K., Larter, R.D., Hillenbrand, C.D., Kuhn, G., Smith, J.A., Jacobs, S., Anderson, J.B., and Jakobsson, M.: Paleo ice flow and subglacial meltwater dynamics in Pine Island Bay, West Antarctica, *Cryosphere*, 7, 249–262, doi:10.5194/tc-7-249-2013, 2013.
- Noormets, R., Dowdeswell, J.A., Larter, R.D., Ó Cofaigh, C., and Evans, J.: Morphology of the upper continental slope in the Bellingshausen and Amundsen Seas - Implications for sedimentary processes at the shelf edge of West Antarctica, *Mar. Geol.*, 258, 100-114, doi: 10.1016/j.margeo.2008.11.011, 2009.
- Ó Cofaigh, C. and Dowdeswell, J.A.: Laminated sediments in glacial marine environments: diagnostic criteria for their interpretation, *Quaternary Sci. Rev.*, 20, 1411-1436, doi: 10.1016/S0277-3791(00)00177-3, 2001.
- Ó Cofaigh, C., Dowdeswell, J.A., Allen, C.S., Hiemstra, J.F., Pudsey, C.J., Evans, J., and Evans, D.J.A.: Flow dynamics and till genesis associated with a marine-based Antarctic palaeo-ice stream, *Quaternary Sci. Rev.*, 24, 709-740, doi: 10.1016/j.quascirev.2004.10.006, 2005.
- Ó Cofaigh, C., Davies, B.J., Livingstone, S.J., Smith, J.A., Johnson, J.S., Hocking, E.P., Hodgson, D.A., Anderson, J.B., Bentley, M.J., Canals, M., Domack, E., Dowdeswell, J.A., Evans, J., Glasser, N.F., Hillenbrand, C.-D., Larter, R.D., Roberts, S.J., and Simms, A.R.: Reconstruction of ice-sheet changes in the Antarctic Peninsula since the Last Glacial Maximum, *Quaternary Sci. Rev.*, 100, 87-100, doi: 10.1016/j.quascirev.2014.06.023, 2014.
- Oakey, R.J., Green, M., Carling, P.A., Lee, M.W.E., Sear, D.A., and Warburton, J.: Grain-shape analysis – a new method for determining representative particle shapes for populations of natural grains, *J. Sediment. Res.*, 75, 1065-1073, doi: 10.2110/jsr.2005.079, 2005.
- O'Regan, M., Cronin, T.M., Reilly, B., Alstrup, A.K.O., Gemery, L., Golub, A., Mayer, L.A., Morlighem, M., Moros, M., Munk, O.L., Nilsson, J., Pearce, C., Detlef, H., Stranne, C., Vermassen, F., West, G., and Jakobsson, M.: The Holocene dynamics of Ryder Glacier and ice tongue in north Greenland, *Cryosphere*, 15, 4073–4097, doi:10.5194/tc-15-4073-2021, 2021.
- Passchier, S., Browne, G., Field, B., Fielding, C.R., Krissek, L.A., Panter, K., Pekar, S.F., and ANDRILL-SMS Science Team: Early and middle Miocene Antarctic glacial history from the sedimentary facies distribution in the AND-2A drill hole, Ross Sea, Antarctica, *GSA Bulletin*, 123, 2352-2365, doi: 10.1130/B30334.1, 2011.

- Passchier, S., Hansen, M.A., and Rosenberg, J.: Quartz grain microtextures illuminate Pliocene periglacial sand fluxes on the Antarctic continental margin, *the Depositional Record*, 7, 564-581, doi: 10.1002/dep2.157, 2021.
- Pelle, T., Morlighem, M., and Bondzio, J.H.: Brief communication: PICOP, a new ocean melt parameterization under ice shelves combining PICO and a plume model, *Cryosphere*, 14, 1043-1049, doi: 10.5194/tc-13-1043-2019, 2019.
- Poinar, K., Joughin, I., Lilien, D., Brucker, L., Kehrl, L., and Nowicki, S.: Drainage of southeast Greenland firn aquifer water through crevasses to bed, *Front. Earth Sci.*, 5, 5, doi: 10.3389/feart.2017.00005, 2017.
- Powell, R.D., Dawber, M., McInnes, J.N., and Pyne, A.R.: Observations at the grounding-line area at a floating glacier terminus, *Ann. Glaciol.*, 22, 217-223, doi: 10.3189/1996AoG22-1-217-223, 1996.
- Prothro, L.O., Simkins, L.M., Majewski, W., and Anderson, J.B.: Glacial retreat patterns and processes determined from integrated sedimentology and geomorphology records. *Mar. Geol.*, 395, 104-119, doi:10.1016/j.margeo.2017.09.012, 2018.
- Prothro, L.O., Majewski, W., Yokoyama, Y., Simkins, L.M., Anderson, J.B., Yamane, M., Miyairi, Y., and Ohkouchi, N.: Timing and pathways of East Antarctic Ice Sheet retreat, *Quaternary Sci. Rev.*, 230, 106166, doi: 10.1016/j.quascirev.2020.106166, 2020.
- Quartini, E., Blankenship, D.D., and Young, D.A.: Active subglacial volcanism in West Antarctica, *Geo. Soc. Mem.*, 55, 785-803, doi: 10.1144/M55-2019-3, 2021.
- Reading, A.M., Stål, T., Halpin, J.A., Lösing, M., Ebbing, J., Shen, W., McCormack, F.S., Siddoway, C.S., and Hasterok, D.: Antarctic geothermal heat flow and its implications for tectonics and ice sheets, *Nat. Rev. Earth Environ.*, 3, 814-831, doi: 10.1038/s43017-022-00348-y, 2022.
- Reilly, B. T., Stoner, J. S., and Wiest, J.: SedCT: MATLAB™ tools for standardized and quantitative processing of sediment core computed tomography (CT) data collected using a medical CT scanner, *Geochem. Geophys. Geosy.*, 18, 3231–3240, doi: 10.1002/2017GC006884, 2017.
- Reilly, B.T., Stoner, J.S., Mix, A.C., Walczak, M.H., Jennings, A., Jakobsson, M., Dyke, L., Glueder, A., Nicholls, K., Hogan, K.A., Mayer, L.A., Hatfield, R.G., Albert, S., Marcott, S., Fallon, S., and Cheseby, M.: Holocene break-up and reestablishment of the Petermann Ice Tongue, Northwest Greenland. *Quaternary Sci. Rev.*, 218, 322-342, doi: 10.1016/j.quascirev.2019/06/023, 2019.
- Reinardy, B.T.I., Hiemstra, J.F., Murray, T., Hillenbrand, C.-D., and Larter, R.D.: Till genesis at the bed of an Antarctic Peninsula palaeo-ice stream as indicated by micromorphological analysis, *Boreas*, 40, 498-517, doi: 10.1111/j.1502-3885.2010.00199.x, 2011.
- Remenda, V.H., Cherry, J.A., and Edwards, T.W.D.: Isotopic composition of old ground water from Lake Agassiz: Implications for late Pleistocene climate, *Science*, 266, 1975-1978, doi: 10.1126/science.266.5193.1975, 1994.
- Rempel, A.W.: A theory for ice-till interactions and sediment entrainment beneath glaciers, *J. Geophys. Res.-Earth*, 113, F01013, doi: 10.1029/2007/JF000870, 2008.
- Rignot, E., Mouginot, J., and Scheuchl, B.: Antarctic grounding line mapping from differential satellite radar interferometry, *Geophys. Res. Lett.*, 38, L10504, doi: 10.1029/2011GL047109, 2011.
- Rignot, E., Jacobs, S., Mouginot, J., and Scheuchl, B.: Ice-shelf melting around Antarctica, *Science*, 341, 266-270, doi: 10.1126/science.1235798, 2013.

- Rignot, E., Mouginot, J., Scheuchl, B., van den Broeke, M., van Wessem, M. J., and Morlighem, M.: Four decades of Antarctic Ice Sheet mass balance from 1979–2017, *P. Natl. Acad. Sci. USA*, 116, 1095. doi: 10.1073/pnas.1812883116, 2019.
- Rilling, S., Mukasa, S., Wilson, T., Lawver, L., and Hall, C.: New determinations of  $^{40}\text{Ar}/^{39}\text{Ar}$  isotopic ages and flow volumes for Cenozoic volcanism in the Terror Rift, Ross Sea, Antarctica, *J. Geophys. Res.* 114, B12207, doi:10.1029/2009JB006303, 2009.
- Robel, A.A., Seroussi, H., and Roe, G.H.: Marine ice sheet instability amplifies and skews uncertainty in projections of future sea-level rise, *P. Natl. Acad. Sci. USA*, 116, 14887-14892, doi: 10.1073/pnas.1904822116, 2019.
- Robinson, D.E., Menzies, J., Wellner, J.S., and Clark, R.W.: Subglacial sediment deformation in the Ross Sea, Antarctica, *Quaternary Sci. Adv.*, 4, 100029, doi:10.1016/j.qsa.2021.100029, 2021.
- Rose, K.C., and Hart, J.K.: Subglacial comminution in the deforming bed: inferences from SEM analysis, *Sediment. Geol.*, 203, 87-97, doi: 10.1016/j.sedgeo.2007.11.003, 2008.
- Rothwell, R. G. and Croudace, I. W. Twenty years of XRF core scanning marine sediments: What do geochemical proxies tell us? *Micro-XRF studies of sediment cores: Applications of a non-destructive tool for the environmental sciences*, 25-102, 2015.
- Roseby, Z.A., Smith, J.A., Hillenbrand, C.-D., Cartigny, M.J.B., Rosenheim, B.E., Hogan, K.A., Allen, C.S., Leventer, A., Kuhn, G., Ehrmann, W., and Larter, R.D.: History of Anvers-Hugo Trough, western Antarctic Peninsula shelf, since the Last Glacial Maximum. Part I: Deglacial history based on new sedimentological and chronological data, *Quaternary Sci. Rev.*, 291, 107590, doi: 10.1016/j.quascirev.2022.107590, 2022.
- Rüther, D.C., Bjarnadóttir, L.R., Junttila, J., Husum, K., Rasmussen, T.L., Lucchi, R.G., and Andreassen, K.: Pattern and timing of the northwestern Barents Sea Ice Sheet deglaciation and indications of episodic Holocene deposition, *Boreas*, 41, 494-512, doi: 10.1111/j.1502-3885.2011.00244.x, 2012.
- Scambos, T.A., Bohlander, J.A., Shuman, C.A., and Skvarca, P.: Glacier acceleration and thinning after ice shelf collapse in the Larsen B embayment, Antarctica, *Geophys. Res. Lett.*, 31, L18402, doi: 10.1029/2004GL020670, 2004.
- Scambos, T.A., Bell, R.E., Alley, R.B., Anandakrishnan, S., Bromwich, D.H., Brunt, K., Christianson, K., Creyts, T., Das, S.B., DeConto, R., Dutrieux, P., Fricker, H.A., Holland, D., MacGregor, J., Medley, B., Nicolas, J.P., Pollard, D., Siegfried, M.R., Smith, A.M., Steig, E.J., Trusel, L.D., Vaughan, D.G., and Yager, P.I.: How much, how fast?: A science review and outlook for research on the instability of Antarctica's Thwaites Glacier in the 21st century, *Global Planet. Change*, 153, 16-34, doi: 10.1016/j.gloplacha.2017.04.008, 2017.
- Schoof, C.: Ice sheet grounding line dynamics: steady states, stability, and hysteresis, *J. Geophys. Res.*, 112, F03S28, doi: 10.1029/2006JF000664, 2007.
- Schroeder, D.M., Blankenship, D.D., and Young, D.A.: Evidence for a water system transition beneath Thwaites Glacier, West Antarctica, *P. Natl. Acad. Sci. USA*, 110, 12225-12228, doi:10.1073/pnas.1302828110, 2013.
- Schroeder, D.M., Blankenship, D.D., Young, D.A., Witus, A.E., and Anderson, J.B.: Airborne radar sounding evidence for deformable sediments and outcropping bedrock beneath Thwaites Glacier, West Antarctica, *Geophys. Res. Lett.*, 41, 7200, 7208, doi: 10.1002/2014GL061645, 2014.

- Schroeder, D.M., Grima, C., and Blankenship, D.D.: Evidence for variable grounding-zone and shear-margin basal conditions across Thwaites Glacier, West Antarctica. *Geophysics*, 81, 1JF-3JF, doi: 10.1190/geo2015-0122.1, 2016.
- Schroeder, D.M., MacKie, E.J., Creyts, T.T., and Anderson, J.B.: A subglacial hydrologic drainage hypothesis for silt sorting and deposition during retreat in Pine Island Bay, *Ann. Glaciol.*, 60, 14–20, doi:10.1017/aog.2019.44, 2019.
- Seeberg-Elverfeldt, J., Schlüter, M., Feseker, T., and Kölling, M.: Rhizon sampling of porewaters near the sediment-water interface of aquatic systems, *Limnol. Oceanogr.: Meth.*, 3, 361-371, doi: 10.4319/lom.2005.3.361, 2005.
- Seroussi, H., Nakayama, Y., Larour, E., Menemenlis, D., Morlighem, M., Rignot, E., and Khazendar, A.: Continued retreat of Thwaites Glacier, West Antarctica, controlled by bed topography and ocean circulation, *Geophys. Res. Lett.*, 44, 6191-6199, doi: 10.1002/2017GL072910, 2017.
- Shackleton, C., Patton, H., Winsborrow, M., Esteves, M., Bjarnadóttir, L., and Andreassen, K.: Distinct modes of meltwater drainage and landform development beneath the last Barents Sea ice sheet, *Front. Earth Sci.*, 11, 1111396, doi: 10.3389/feart.2023.1111396, 2023.
- Shreve, R.L.: Movement of water in glaciers, *J. Glaciol.*, 11, 205-214, doi: 10.3189/S0022143000002219X, 1972.
- Siegfried, M.R., Fricker, H.A., Carter, S.P., and Tulaczyk, S.: Episodic ice velocity fluctuations triggered by a subglacial flood in West Antarctica, *Geophys. Res. Lett.*, 43, 2640-2648, doi: 10.1002/2016GL067758, 2016.
- Siegfried, M.R., Venturelli, R.A., Patterson, M.O., Arnuk, W., Campbell, T.D., Gustafson, C.D., Michaud, A.B., Galton-Fenzi, B.K., Hausner, M.B., Holzschuh, S.N., Huber, B., Manoff, K.D., Schroeder, D.M., Summers, P.T., Tyler, S., Carter, S.P., Fricker, H.A., Harwood, D.M., Leventer, A., Rosenheim, B.E., Skidmore, M.L., Priscu, J.C., and the SALSA Science Team: The life and death of a subglacial lake in West Antarctica, *Geology*, 51, 434-438, doi: 10.1130/G50995.1, 2023.
- Silvano, A., Rintoul, S.R., Pena-Molino, R., Hobbs, W.R., van Wijk, E., Aoki, S., Tamura, T., and Williams, G.D.: Freshening by glacial meltwater enhances melting of ice shelves and reduces formation of Antarctic Bottom Water, *Sci. Advances*, 4, eaap9467, doi: 10.1126/sciadv.aap9467, 2018.
- Simkins, L.M., Anderson, J.B., Prothro, L.O., Halberstadt, A.R.W., Stearns, L.A., Pollard, D., and DeConto, R.M.: Anatomy of a meltwater drainage system beneath the ancestral East Antarctic ice sheet, *Nat. Geosci.*, 10, 691-697, doi:10.1038/ngeo3012, 2017.
- Simkins, L.M., Greenwood, S.L., and Anderson, J.B.: Diagnosing ice sheet grounding line stability from landform morphology, *Cryosphere*, 12, 2707-2726, doi:10.5194/tc-12-2707-2018, 2018.
- Simkins, L.M., Greenwood, S.L., Munevar Garcia, S., Eareckson, E.A., Anderson, J.B., and Prothro, L.O.: Topographic controls on channelized meltwater in the subglacial environment. *Geophys. Res. Lett.*, 48, 1-11, doi: 10.1029/2021GL094678, 2021.
- Simkins, L.M., Greenwood, S.L., Winsborrow, M.C.M., Bjarnadóttir, L.R., and Lepp, A.P.: Advances in understanding subglacial meltwater drainage from past ice sheets, *Ann. Glaciol.*, 1-5, doi: 10.1017/aog.2023.16, 2023.
- Simões Pereira, P., van de Fliedert, T., Hemming, S.R., Hammond, S.J., Kuhn, G., Brachfeld, S., Doherty, C., and Hillenbrand, C.-D.: Geochemical fingerprints of glacially eroded

- bedrock from West Antarctica: Detrital thermochronology, radiogenic isotope systematics and trace element geochemistry in Late Holocene glacial-marine sediments, *Earth-Sci. Rev.*, 182, 204-232, doi: 10.1016/j.earscirev.2018.04.011, 2018.
- Simões Pereira, P., van de Flierdt, T., Hemming, S.R., Frederichs, T., Hammond, S.J., Brachfeld, S., Doherty, C., Kuhn, G., Smith, J.A., Klages, J.P., and Hillenbrand, C.-D.: The geochemical and mineralogical fingerprint of West Antarctica's weak underbelly: Pine Island and Thwaites glaciers, *Chem. Geol.*, 550, 119649, doi: 10.1016/j.chemgeo.2020.119649, 2020.
- Smith, A.M., Jordan, T.A., Ferraccioli, F., and Bingham, R.G.: Influence of subglacial conditions on ice stream dynamics: seismic and potential field data from Pine Island Glacier, West Antarctica, *J. Geophys. Res.-Earth*, 118, 1471-1482, doi: 10.1029/2012JB009582, 2013.
- Smith, B.E., Gourmelen, N., Huth, A., Joughin, I.: Connected subglacial lake drainage beneath Thwaites Glacier, West Antarctica, *Cryosphere*, 11, 451-467. doi: 10.5194/tc-11-451-2017, 2017.
- Smith, J. A., Hillenbrand, C.-D., Larter, R. D., Graham, A. G. C., and Kuhn, G.: The sediment infill of subglacial meltwater channels on the West Antarctic continental shelf, *Quaternary Res.*, 71, 190–200. doi: 10.1016/j.yqres.2008.11.005, 2009.
- Smith, J.A., Hillenbrand, C.-D., Kuhn, G., Klages, J.P., Graham, A.G.C., Larter, R.D., Ehrmann, W., Moreton, S.G., Wiers, S., and Frederichs, T.: New constraints on the timing of West Antarctic Ice Sheet retreat in the eastern Amundsen Sea since the Last Glacial Maximum, *Global Planet. Change*, 122, 224-237, doi: 10.1016/j.gloplacha.2014.07.015, 2014.
- Smith, J.A., Anderson, T.J., Shortt, M., Gaffney, A.M., Truffer, M., Stanton, T.P., Bindshadler, R., Dutrieux, P., Jenkins, A., Hillenbrand, C.-D., Ehrmann, W., Corr, H.F.J., Farley, N., Crowhurst, S., and Vaughan, D.G.: Sub-ice-shelf sediments record history of twentieth-century retreat of Pine Island Glacier, *Nature*, 541, 77-80, doi: 10.1038/nature20136, 2017.
- Smith, J.A., Graham, A.G.C., Post, A.L., Hillenbrand, C.-D., Bart, P.J., and Powell, R.D.: The marine geological imprint of Antarctic ice shelves, *Nat. Commun.*, 10, 1-16, doi: 10.1038/s41467-019-13496-5, 2019.
- Smith, L.C., Chu, V.W., Yang, K., Gleason, C.J., Pitcher, L.H., Rennermalm, A.K., Legleiter, C.J., Behar, A.E., Overstreet, B.T., Moustafa, S.E., Tedesco, M., Forster, R.R., LeWinter, A.L., Finnegan, D.C. Sheng, Y., and Balog, J.: Efficient meltwater drainage through supraglacial streams and rivers on the southwest Greenland ice sheet, *P. Natl. Acad. Sci. USA*, 112, 1001-1006, doi: 10.1073/pnas.1413024112, 2015.
- St. John, K., Passchier, S., Tantillo, B., Darby, D., and Kearns, L.: Microtextures of modern sea-ice-rafted sediment and implications for paleo-sea-ice reconstructions, *Ann. Glaciol.*, 56, 83-93, doi: 10.3189/2015AoG69A586, 2015.
- Stearns, L. A., Smith, B. E., and Hamilton, G. S.: Increased flow speed on a large East Antarctic outlet glacier caused by subglacial floods, *Nat. Geosci. Letters*, 1, 827-831, doi:10.1038/ngeo356, 2008.
- Steig, E.J., Ding, Q., Battisti, D.S., and Jenkins, A.: Tropical forcing of Circumpolar Deep Water inflow and outlet glacier thinning in the Amundsen Sea Embayment, West Antarctica, *Ann. Glaciol.*, 53, 19-28, doi: 10.3189/2012AoG60A110, 2012.
- Streuff, K., Ó Cofaigh, C., Hogan, K., Jennings, A., Lloyd, J.M., Noormets, R., Nielsen, T., Juijpers, A., Dowdeswell, J.A., and Weinrebe, W.: Seafloor geomorphology and glacial-marine sedimentation associated with fast-flowing ice sheet outlet glaciers in Disko

- Bay, West Greenland, *Quaternary Sci. Rev.*, 169, 206-230 doi: 10.1016/j.quascirev.2017.05.021, 2017.
- Subt, C., Yoon, H.I., Yoo, K.C., Lee, J.I., Leventer, A., Domack, E.W., and Rosenheim, B.E.: Sub-ice shelf sediment geochronology utilizing novel radiocarbon methodology for highly detrital sediments, *Geochem., Geophys., Geosy.*, 18, 1404-1418, doi: 10.1002/2016GC006578, 2017.
- Sutherland, B.R., Rosevear, M.G., and Cenedese, C.: Laboratory experiments modeling the transport and deposition of sediments by glacial plumes rising under an ice shelf, *Phys. Rev. Fluids*, 5, 013802, doi: 10.1103/PhysRevFluids.5.013802, 2020.
- Sweet, D.E., and Brannan, D.K.: Proportion of glacially to fluvially induced quartz grain microtextures along the Chitina River, SE Alaska, U.S.A., *J. Sediment. Res.*, 86, 749-761, doi: 10.2110/jsr.2016.49, 2016.
- Swift, D.A., Nienow, P.W., and Hoey, T.B.: Basal sediment evacuation by subglacial meltwater: suspended sediment transport from Haut Glacier d'Arolla, Switzerland, *Earth Surf. Proc. Land.*, 30, 867-883, doi: 10.1002/esp.1197, 2005.
- Trusel, L.D., Frey, K.E., Das, S.B., Karnauskas, K.B., Munneke, P.K., van Meijgaard, E., and van den Broeke, M.R.: Divergent trajectories of Antarctic surface melt under two twenty-first-century climate scenarios, *Nat. Geosci.*, 8, 927-932, doi: 10.1038/ngeo2563, 2015.
- Turcotte, D., and Schubert, G.: *Geodynamics*, 3<sup>rd</sup> Edn., Cambridge University Press, Cambridge, 2014.
- Valletta, R.D., Willenbring, J.K., Passchier, S., and Elmi, C.: 10Be/9Be ratios reflect Antarctic Ice Sheet freshwater discharge during Pliocene warming, *Paleoceanography and Paleoclimatology*, 33, 934-944, doi: 10.1029/2017PA003283, 2018.
- van Hateren, J.A., van Buuren, U., Arens, S.M., van Balen, R.T., and Prins, M.A.: Identifying sediment transport mechanisms from grain size-shape distributions, applied to aeolian sediments, *Earth Surf. Dynam.*, 8, 527-553, doi:10.5194/esurf-8-527-2020, 2020.
- Vaughan, D.G., Corr, H.F.J., Bindshadler, R.A., Dutrieux, P., Gudmundsson, G.H., Jenkins, A., Newman, T., Vornberger, P., and Wingham, D.J.: Subglacial melt channels and fracture in the floating part of Pine Island Glacier, Antarctica. *J. Geophys. Res-Earth*, 117, F03012, doi: 10.1029/2012JF002360, 2012.
- Vick-Majors, T.J., Michaud, A. B., Skidmore, M. L., Turetta, C., Barbante, C., Christner, B. C., Dore, J.E., Christianson, K., Mitchell, A.C., Achberger, A.M., Mikucki, J.A., and Priscu, J.C.: Biogeochemical connectivity between freshwater ecosystems beneath the West Antarctic ice sheet and the sub-ice marine environment. *Global Biogeochemical Cycles*, 34, e2019GB006446. doi: 10.1029/2019GB006446, 2020.
- von Blanckenburg, F., Hewawasam, T., and Kubik, P.W.: Cosmogenic nuclide evidence for low weathering and denudation in the wet, tropical highlands of Sri Lanka, *J. Geophys. Res.-Earth*, 109, F03008, doi: 10.1029/2003FJ000049, 2004.
- Vos, K., Vandenbergh, N., and Elsen, J.: Surface textural analysis of quartz grains by scanning electron microscopy (SEM): From sample preparation to environmental interpretation, *Earth-Sci. Rev.*, 128, 193-104, doi:10.1016/j.earscirev.2013.10.013, 2014.
- Wacker, L., Bonani, G., Friedrich, M., Hajdas, I., Kromer, B., Němec, M., Ruff, M., Suter, M., Synal, H.-A., and Vockenhuber, C.: MICADAS: Routine and high-precision radiocarbon dating, *Radiocarbon*, 52, 252-262, doi: 10.1017/S0033822200045288, 2010.
- Wählin, A., Graham, A.G.C., Hogan, K., Queste, B.Y., Boehme, L., Larter, R.D., Pettit, E.C., Wellner, J., and Heywood, K.J.: Pathways and modification of warm water flowing

- beneath Thwaites Ice Shelf, West Antarctica. *Science Advances*, 7, doi: 10.1126/sciadv.abd7254, 2021.
- Weertman, J.: Stability of the Junction of an Ice Sheet and an Ice Shelf, *J. Glaciol.*, 13, 3-11, doi: 10.3189/S0022143000023327, 1974.
- Wei, W., Blankenship, D.D., Greenbaum, J.S., Gourmelen, N., Dow, C.F., Richter, Greene, C.A., Young, D.A., Lee, S., Kim, T-W., Lee, W.S., and Assmann, K.M.: Getz Ice Shelf melt enhanced by freshwater discharge from beneath the West Antarctic Ice Sheet. *The Cryosphere*, 14, 1399–1408, doi: 10.5194/tc-14-1399-2020, 2020.
- Wellner, J.S., Heroy, D.C., Anderson, J.B.: The death mask of the Antarctic Ice Sheet: Comparison of glacial geomorphic features across the continental shelf, *Geomorphology*, 75, 157-171. doi: 10.1016/j.geomorph.2005.05.015, 2006.
- Wellner, J.S., Anderson, J.B., Ehrmann, W., Weaver, F.M., Kirshner, A., Livsey, D., and Simms, A.R.: History of an Evolving Ice Sheet as Recorded in SHALDRIL Cores From the Northwestern Weddell Sea, Antarctica, in: *Tectonic, Climatic, and Cryospheric Evolution of the Antarctic Peninsula*, American Geophysical Union, Washington, DC, USA, 131-151, doi: 10.1029/2010SP001047, 2011.
- White, D.A., Fink, D., Post, A.L., Simon, K., Galton-Fenzi, B., Foster, S., Fujioka, T., Jeromson, M.R., Blaxell, M., and Yokoyama, Y.: Beryllium isotope signatures of ice shelves and sub-ice shelf circulation, *Earth Plan. Sci. Lett.*, 505, 86-95, doi: 10.1016/j.epsl.2018.10.004, 2019.
- Willis, M.J., Herried, B.G., Bevis, M.G., and Bell, R.E.: Recharge of a subglacial lake by surface meltwater in northeast Greenland, *Nature*, 518, 223-227, doi: 10.1038/nature14116, 2015.
- Wingham, D.J., Siegert, M.J., Shepherd, A., and Muir, A.S.: Rapid discharge connects Antarctic subglacial lakes, *Nature*, 440, 1033-1036, doi: 10.1038/nature04660, 2006.
- Winsborrow, M.C.M., Andreassen, K., Corner, G.D., and Laberg, J.S.: Deglaciation of a marine-based ice sheet: Late Weichselian palaeo-ice dynamics and retreat in the southern Barents Sea reconstructed from onshore and offshore glacial geomorphology, *Quaternary Sci. Rev.*, 29, 424-442, doi: 10.1016/j.quascirev.2009.10.001, 2010.
- Wittmann, H., Blanckenburg, F., Bouchez, J., Dannhaus, N., Naumann, R., Christl, M., and Gaillardet, J.: The dependence of meteoric  $^{10}\text{Be}$  concentrations on particle size in Amazon River bed sediment and the extraction of reactive  $^{10}\text{Be}/^{9}\text{Be}$  ratios, *Chem. Geol.* 318, 126–138, doi: 10.1016/j.chemgeo.2012.04.031, 2012.
- Witus, A.E., Braneky, C.M., Anderson, J.B., Szczucinski, W., Schroeder, D.M., Blankenship, D.D., and Jakobsson, M.: Meltwater intensive retreat in polar environments and investigation of associated sediments: example from Pine Island Bay, West Antarctica, *Quaternary Sci. Rev.*, 85, 99–118, doi:10.1016/j.quascirev.2013.11.021, 2014.
- Yawar, Z. and Schieber, J.: On the origin of silt laminae in laminated shales, *Sediment. Geol.*, 360, 22-34, doi:10.1016/j.sedgeo.2017.09.001, 2017.
- Yokoyama, Y., Anderson, J.B., Yamane, M., Simkins, L.M., Miyairi, Y., Yamazaki, T., Koizumi, M., Suga, H., Kusahara, K., Prothro, L., Hasumi, H., Southon, J.R., and Ohkouchi, N.: Widespread collapse of the Ross Ice Shelf during the late Holocene, *P. Natl. Acad. Sci. USA*, 113, 2354-2359, doi: 10.1073/pnas.1516908113, 2016.
- Young, D.A., Schroeder, D.M., Blankenship, D.D., Kempf, S.D., and Quartini, E.: The distribution of basal water between Antarctic subglacial lakes from radar sounding, *Phil. Trans. R.Soc. A*, 374, 20140297, doi: 10.1098/rsta.2014.0297, 2016.

- Yu, H., Rignot, E., Seroussi, H., Morlighem, M.: Retreat of Thwaites Glacier, West Antarctica, over the next 100 years using various ice flow models, ice shelf melt scenarios and basal friction laws, *Cryosphere*, 12, 3861-3876. doi: 10.5194/tc-12-3861-2018, 2018.
- Zoet, L.K., Hansen, D.D., Morgan-Witts, N., Menzies, J., Sobol, P., and Lord, N.: An experimental baseline for ice-till strain indicators, *Can. J. Earth Sci.*, 60, 537-549, doi: 10.1139/cjes-2022-0074, 2023.